


A CRC Press FREEBOOK

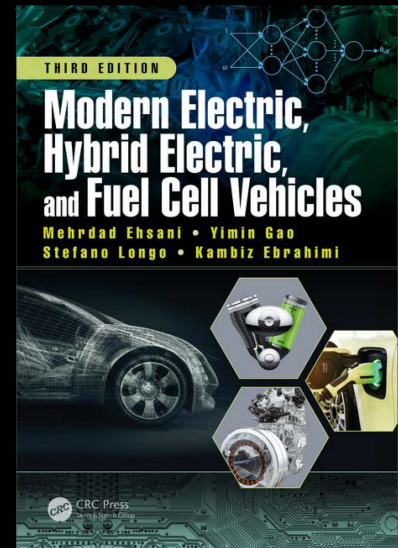
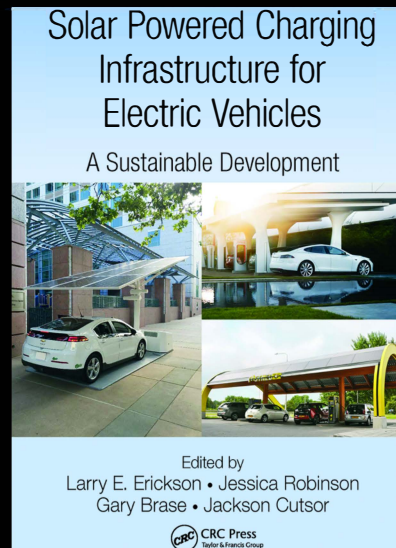
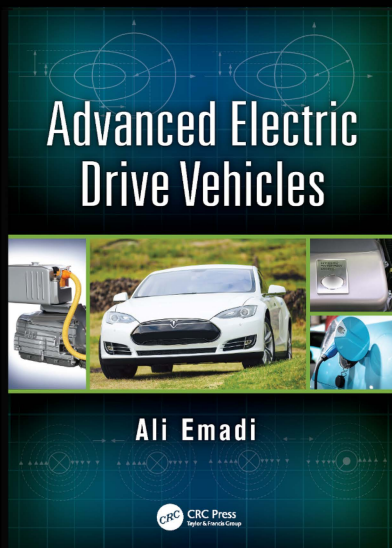
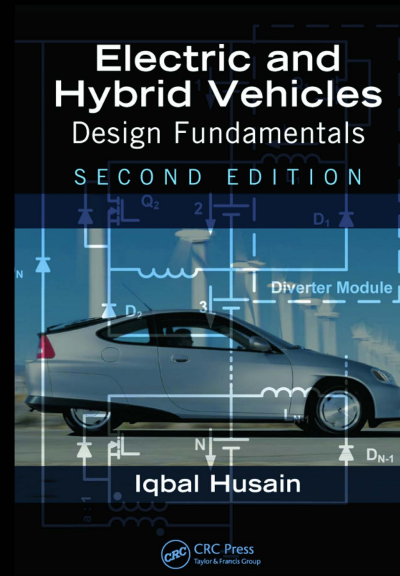
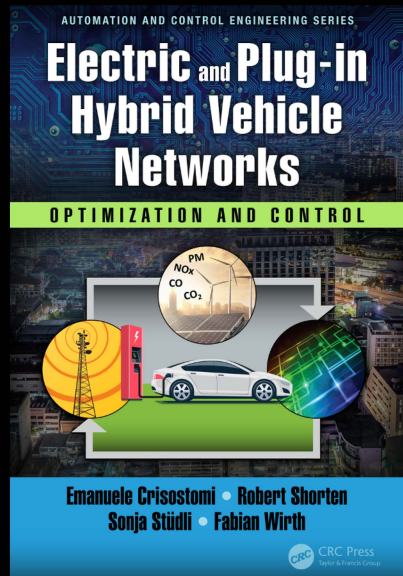
Hybrid & Electric Vehicles



TABLE OF CONTENTS

-  Introduction
-  1 • Introduction to Electric Vehicles *from Electric and Plug-in Hybrid Vehicle Networks: Optimization and Control*
-  2 • Electric Machines *from Electric and Hybrid Vehicles: Design Fundamentals, Second Edition*
-  3 • Fundamentals of Conventional Vehicles and Powertrains *from Advanced Electric Drive Vehicles*
-  4 • Hybrid Energy Storage Systems *from Advanced Electric Drive Vehicles*
-  5 • Solar Powered Charging Stations *from Solar Powered Charging Infrastructure for Electric Vehicles: A Sustainable Development*
-  6. Internal Combustion Engines *from Modern Electric, Hybrid Electric, and Fuel Cell Vehicles, Third Edition*

READ THE LATEST ON ELECTRICAL ENGINEERING WITH THESE KEY TITLES



VISIT WWW.CRCPRESS.COM
TO BROWSE FULL RANGE OF ELECTRICAL ENGINEERING TITLES



Introduction

In response to increasing demand for low-carbon technologies, we educate in hybrid and fully electric vehicle development from CRC Press.

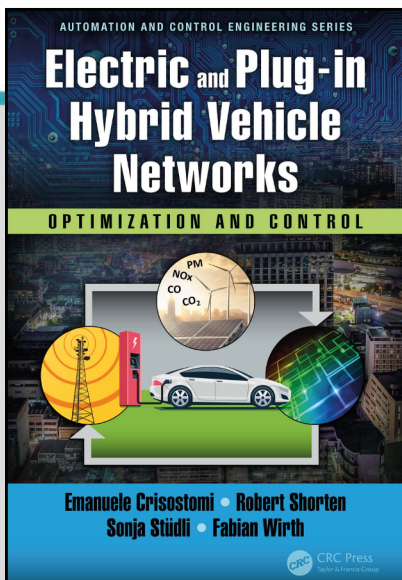
These books show students and professionals alike how electrical and mechanical engineers must work together to complete an alternative vehicle system. It empowers them to carry on state-of-the-art research and development in automotive engineering in order to meet today's needs of clean, efficient, and sustainable vehicles!



CHAPTER

1

INTRODUCTION TO ELECTRIC VEHICLES



This chapter is excerpted from

*Electrical and Plug-in Hybrid Vehicle Networks:
Optimization and Control*

by Emanuele Crisostomi, Robert Shorten, Sonja Stüdli
& Fabian Wirth

© 2018 Taylor & Francis Group. All rights reserved.



[Learn more](#)

1

Introduction to Electric Vehicles

1.1 Introduction

Growing concerns over the limited supply of fossil-based fuels are motivating intense activity in the search for alternative road transportation propulsion systems. In addition, regulatory pressures to reduce urban pollution, CO_2 emissions and city noise have made plug-in electric vehicles [23, 166] a very attractive choice as the alternative to the internal combustion engine [140]. However, despite the enormous benefits of such vehicles, their adoption and uptake has, to this point, been disappointing. In this chapter we shall outline some of the impediments to electric vehicles, and discuss some of the solutions to these problems that will be addressed in this book, as well as other opportunities that arise when using this new form of mobility.

1.2 Benefits and Challenges

Basically, an Electric Vehicle (EV) is a vehicle that no longer relies solely on an Internal Combustion Engine (ICE) as the only propulsion mechanism, but rather uses an electric drive system as a replacement, or to enhance, the ICE. Roughly speaking, three types of electrically propelled vehicles can be distinguished.

- A Hybrid Electric Vehicle (HEV) combines an ICE and an electric motor within the drive train. Mostly, the electric motor supports the ICE for fuel economy and/or performance. The vehicle is then either propelled by the combustion engine or the electric drive.
- A Plug-in Hybrid Electric Vehicle (Plug-in Hybrid Electric Vehicle (PHEV)) is a vehicle equipped, in general, with a larger battery compared to HEVs, that allows recharging of the battery via home outlets or at charging stations. While in most cases both the electric drive and the ICE are able to propel the vehicle, some vehicles use solely the electric drive. In this latter case the ICE can be used to recharge the battery or directly

produce electricity for the electric drive. Also, in most cases PHEVs can be used in a full electric mode if there is enough energy stored in the battery. This allows one to select when and where to release pollutants. This functionality shall be used in some applications discussed in the book.

- A Full Electric Vehicle (FEV) runs solely on an electric drive system. As with PHEVs their batteries are large and can be recharged in charging stations or at home. Since there are no pollutants released while driving, these vehicles are often marketed as zero-emission vehicles. Naturally, this is not exactly a correct terminology, since the recharging of the batteries will cause emissions depending on the actual emissions of the power generation in the country. Due to the fact that many power plants are located in less populated areas, the use of FEVs still has beneficial effects on emissions in population centers. Such vehicles may be considered *as filters for turning dirty into clean energy*.

Of these three types, we shall distinguish PHEVs and FEVs from HEVs, and we shall denote the former as plug-in EVs, to emphasize that they continuously have to recharge their batteries. In Figure 1.1 a graphical overview over the various EV types is given.

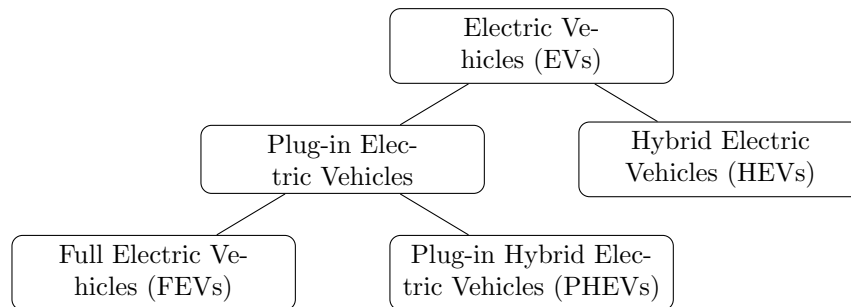


FIGURE 1.1

Classification of some different EV types

While the deployment of plug-in EVs can give rise to various environmental and health improvements, their adoption to date has been disappointing. According to initial reports [6], even in Europe, where the green agenda was well received, fewer than 12 000 EVs were sold in the first half of 2012 (of which only 1000 of these were sold in the UK). This number represented less than 0.15% of total new car sales in that year. These figures were in spite of the fact that many European governments had offered incentives for the purchase of EVs in the form of subsidies and had also invested in enabling infrastructure. There are however hints that the numbers may soon dramatically change. For instance, growing 59% year over year (YoY), approximately 12 000 electric cars were sold across the US in January 2017, accounting for

approximately 1% of US auto sales¹. Similarly, the Chinese market had more than 32 000 new electric cars on the streets in March 2017, an 89% increase over the same month the previous year, with the annual growth rate at 31%². Numbers in Europe remain contradictory, with Northern countries leading the market (e.g., in 2017 Norway has the highest per capita number of all-electric cars in the world: more than 100 000 in a country of 5.2 million people³). However, things seem to be speeding up, recently Volvo have announced that all new cars launched from 2019 onwards will be partially or completely battery-powered. The company called this step a “historic end” to building models that only have an internal combustion engine⁴. The day after the Volvo announcement, Emmanuel Macron’s government announced that France will end sales of petrol and diesel vehicles by 2040, as part of an ambitious plan to meet the targets of the Paris climate accord⁵. Only few days later, a similar plan was unveiled to ban the sale of new diesel and petrol cars by 2040 in the UK in a bid to encourage people to buy electric vehicles⁶.

Despite such recent promising signals, still the percentage of traveling EV remains very low at a global scale. Some of the main factors hindering the widespread adoption of EVs from the point of view of customers are as follows:

1. **Price:** EVs have, to date, been expensive, even when subsidized. A major factor in the cost of such vehicles is the cost of the battery [13]. While battery costs are forecast to reduce dramatically over the next few years [27, 158], this is currently an important aspect in understanding the sales of EVs. In response to this, some companies, are proposing to lease batteries to the customer to offset some of the battery related costs.
2. **Vehicle size:** EVs are sometimes small with limited luggage space to reduce energy consumption, or to accommodate batteries (in some hybrid vehicles). This is sometimes a problem for potential purchasers of vehicles who, on occasion, would like to transport significant loads using their vehicles.
3. **Long charging times:** Charging times for plug-in EVs can be long [201]. An often cited fact by advocates of electric vehicles in response to this is that fast charging methods can service average vehicles in about 30 minutes [35, 28]. Such time-scales may be just about acceptable to a normal

¹<https://cleantechnica.com/2017/02/04/us-electric-car-sales-59-january-2017/>. Last Accessed July 2017.

²<https://evobsession.com/china-electric-car-sales-keep-soaring-march-2017/>. Last Accessed July 2017.

³<http://e360.yale.edu/features/with-norway-in-the-lead-europe-set-for-breakout-on-electric-vehicles>. Last Accessed July 2017.

⁴<https://www.theguardian.com/business/2017/jul/05/volvo-cars-electric-hybrid-2019>. Last Accessed July 2017.

⁵<https://www.theguardian.com/business/2017/jul/06/france-ban-petrol-diesel-cars-2040-emmanuel-macron-volvo>. Last Accessed July 2017.

⁶<http://www.telegraph.co.uk/news/2017/07/25/new-diesel-petrol-cars-banned-uk-roads-2040-government-unveils/>. Last Accessed July 2017.

car owner. However, in the presence of queuing, 30 minutes can rapidly become several hours, and push such fast charging stations into the realm of “not acceptable”. Thus, it is likely that overnight or workplace charging will be the principal method of vehicle charging for the foreseeable future. An associated issue in large cities concerns the availability of charging points. This is especially an issue in cities with large apartment block type dwellings.

4. **Limited range:** Maximum ranges of less than 300 km in favorable conditions are not unusual for EVs, and this reduces significantly when air-conditioning or heating is switched on [49]. Hence, the range is not only limited but to a certain degree also unpredictable, which worsens the issue. Additionally, other issues, that are a nuisance for normal ICE vehicles, are exacerbated as a result of the limited range. For example, the cost of searching for a parking space at the end of a journey is much higher than for a conventional vehicle, because the EV’s range is low and therefore energy should not be wasted searching for a parking spot. Research is ongoing to address these issues, with much of the current work focusing on new battery types, optimal vehicle charging, vehicle routing, and in-vehicle energy management systems with a view to minimizing wastage of energy and thereby increasing vehicle range [162].⁷

The latter two issues are often grouped together as one and discussed under the title of *range anxiety* [140, 180]. Further challenges that arise include the following.

1. **Charging (from the perspective of generation distributors):** The energy that will potentially be required to charge the large volumes of batteries of EVs will considerably increase the load on the distribution grid, and can cause power quality issues when not regulated.
2. **Traffic management:** While traffic management in general is an important factor, the issue becomes more pressing if EVs are present due to their limited energy availability. Hence, a traffic jam or rerouting due to road work or accidents, can have a strong impact on the energy required for the journey and in the worst case force the drivers to recharge before the end of the journey.
3. **Charging Infrastructure:** While momentarily most charging occurs at home during night-time, an important consideration is the availability and distribution of charging stations. This is related to the issue of limited

⁷Some of these issues lead to changes in driver behavior when faced with the need to increase range. For example, in [194], behavioral adaptations (in response to limited available energy) were observed among participants of a study group, who were leased a battery EV for a year. Some of these behavioral adaptations included turning off the air conditioning or heater and driving more slowly, as well as swapping vehicles with other users.

range and long charging times, i.e. range anxiety. A major issue in this context is charge point anxiety - that is the angst associated with not being able to access a charge point when needed.

4. **Electromagnetic emissions:** Another issue regarding EVs concerns electromagnetic emissions. While there is no evidence that electromagnetic radiation from EVs is dangerous, this issue is a focus point for regulatory authorities (see e.g. the EU Green Car Programme) and has been raised by several research agencies [7].
5. **Battery related issues:** A further concern is whether enough lithium can be sourced to build batteries to construct enough vehicles to replace the existing passenger vehicle fleet. Are we simply substituting one rare resource (oil) with another (lithium)? Also, the transportation of batteries is not trivial and necessitates special precautions [126, 9]. Finally, most reasonably sized batteries are not capable of realizing the range enjoyed by conventional ICE based vehicles, which comes in play in regard to the above mentioned issue of range anxiety. While this latter issue is the subject of much research, battery size and performance currently represent one of the major determinants in the design of EVs today [14, 13].

1.3 Contribution of the Book

Our objective in this book is to address some of the issues that impede the adoption of plug-in EVs. Rather than focusing on single vehicles, our focus shall be on developing techniques to better use networks of electric vehicles. We believe, at the time of writing this book, that this aspect of EV technology has not been significantly documented elsewhere.

To this end we partitioned the book into four parts. The first part of the book is concerned with energy management. Topics that we shall consider include: plug-and-play infrastructure for charging fleets of vehicles; how energy is dissipated in electric vehicles; how to avoid queuing at charging stations; routing of EVs to consume energy efficiently; and a consideration of some of the unintended consequence of plug-in EV usage.

The second part of the book will consider using ideas from the sharing economy to better share “road electrification”. Topics that we shall consider include: on demand mobility for EVs; and the sharing of personal charge points.

The third part of the book will focus on the actuation possibilities afforded by the use of PHEVs. By judiciously selecting when/where one

engages the electric motor, a range of new ideas can be implemented in cities. Specifically, we shall see how such ideas can be used to regulate emissions in a local region, better balance the needs of the grid and the transportation network, and manage energy consumption in a fleet of vehicles.

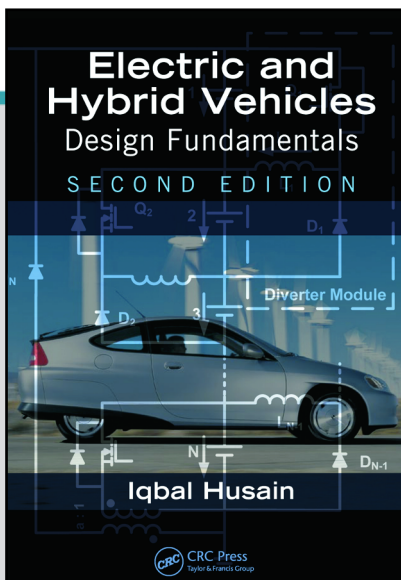
Finally, the last part of the book discusses analytics that can be used to support the design and testing of electro mobility (E-mobility) concepts without the need for large scale fleet testing.



CHAPTER

2

ELECTRIC MACHINES



This chapter is excerpted from

Electric and Hybrid Vehicles: Design Fundamentals, Second Edition

by Iqbal Husain

© 2010 Taylor & Francis Group. All rights reserved.



[Learn more](#)

6

Electric Machines

An *electric machine* is an electromechanical device used for energy conversion from electrical to mechanical and vice versa. In a vehicle system, the electric machine can be designed to process supplied energy and deliver power or torque to the transaxle for propulsion. The machine also processes the power flow in the reverse direction during regeneration when the vehicle is braking converting mechanical energy from the wheels into electrical energy. The term *motor* is used for the electric machine when energy is converted from electrical to mechanical, and the term *generator* is used when power flow is in the opposite direction with the machine converting mechanical energy into electrical energy. The braking mode in electric machines is referred to as *regenerative braking*. There are electrical, mechanical, and magnetic losses during the energy conversion process in either direction in an electric machine, which affect the conversion efficiency. Some energy is always lost from the system for any energy conversion process. However, the conversion efficiency of electric machines is typically quite high compared to that of other types of energy conversion devices.

In electric vehicles, the electric motor is the sole propulsion unit, while in hybrid vehicles, the electric motor and the internal combustion (IC) engine together in a series or parallel combination provide the propulsion power. In electric and hybrid vehicles, the electric traction motor converts electrical energy from the energy storage device to mechanical energy that drives the wheels of the vehicle. The major advantages of an electric motor over an IC engine is that the motor provides full torque at low speeds and the instantaneous power rating can be two or three times the rated power of the motor. These characteristics give the vehicle excellent acceleration with a nominally rated motor.

Electric motors can be DC type or AC type. The DC series motors were used in a number of prototype electric vehicles in the 1980s and prior to that due to its excellent match with the road load characteristics and ease of control. However, the size and maintenance requirements of DC motors are making their use obsolete not just in the automotive industry, but in all motor drive applications. The more recent electric and hybrid vehicles employ AC and brushless motors, which include induction motors, permanent magnet (PM) motors, and switched reluctance motors. The AC induction motor technology is quite mature, and significant research and development activities have taken place on induction motor drives over the past 50 years. The control of induction motors is much more complex than DC motors, but with the

availability of fast digital processors, the computational complexity can be easily managed. Vector control techniques developed for sinusoidal machines make the control of AC motors similar to that of a DC motor through reference frame transformation techniques. The computational complexity arises from these reference frame transformations, but today's digital processors are capable of completing complex algorithms in a relative short time.

The competitor to induction motors is the PM motors. The PM AC motors have magnets on the rotor, while the stator construction is the same as that of the induction motor. The PM motors can be of surface-mounted type or the magnets can be inset within the rotor in the interior permanent magnet (IPM) motors. The PM motor can also be classified as sinusoidal type or trapezoidal type, depending on the flux distribution in the air gap. The trapezoidal motors have concentrated three-phase windings and are also known as brushless DC motors. The PM motors are driven by a six-switch inverter just like an induction motor, but the control is relatively simpler than that of the induction motor. The use of high-density, rare earth magnets in PM motors provides high power density, but at the same time the cost of magnets is on the negative side for these motors. For electric and hybrid vehicle applications, the motor size is relatively large compared to the other smaller power applications of PM motors, which amplifies the cost problem. However, the hybrid vehicle motors are much smaller than electric vehicle motors, and the performance and efficiency achievable from PM motors may be enough to overcome the cost problem. The IPM motors have excellent performance characteristics, much superior than the surface-mount PM motors, but the manufacturing complexity is one of the drawbacks of these motors.

Another candidate for traction motors is the switched reluctance (SR) motors. These motors have excellent fault tolerance characteristics and their construction is fairly simple. The SR motors have no windings, magnets, or cages on the rotor, which helps increase the torque/inertia ratio and allows higher rotor operating temperature. The constant power speed range is the widest possible in SR motors compared to other technologies, which makes it ideally suitable for traction applications. The two problems associated with SR motors are acoustic noise and torque ripple. There are well-developed techniques to address both; moreover, for several traction applications, noise and torque ripple are not of big concern.

6.1 Simple Electric Machines

The torque in electric machines is produced utilizing the basic principles of electromagnetic theory in one of two ways: (1) by the mutual interaction of two orthogonal magnetomotive forces (mmf) utilizing the Lorentz force principle, and (2) by using a varying reluctance flux path where the rotor

moves toward attaining the minimum reluctance position. The DC and AC machines, including the PM machines, work on the first principle, while the switched and synchronous reluctance machines work on the latter principle. The fundamental machine phenomenon responsible for inducing voltage and producing torque is explained in this section followed by two simple machine configurations that operate based on the two different principles.

6.1.1 Fundamental Machine Phenomena

An electric machine converts electrical energy to mechanical energy in the motoring mode and mechanical energy to electrical energy in the generating mode. The same electric machine can be used to serve either as a motor or a generator with appropriate changes in the control algorithm. Two basic phenomena responsible for this electromechanical energy conversion occur simultaneously in electrical machines. These are

1. Voltage is induced when a conductor moves in an electric field.
2. When a current-carrying conductor is placed in an electric field, the conductor experiences a mechanical force.

6.1.1.1 Motional Voltage

When a conductor is moving in a uniform magnetic field \vec{B} with a velocity \vec{v} , there will be voltage induced in the conductor given by

$$\vec{e} = (\vec{v} \times \vec{B}) \cdot \vec{l} \quad (6.1)$$

The voltage induced is known as motional voltage or speed voltage. The above is a mathematical definition of Faraday's law of electromagnetic induction, which is written as

$$e = -\frac{d\lambda}{dt} = -N \frac{d\phi}{dt} \quad (6.2)$$

where

λ is the flux linkage

ϕ is the flux

N is the number of turns

For the conductor of length l shown in Figure 6.1, which is moving with a velocity \vec{v} in a magnetic field \vec{B} that is perpendicularly directed into the plane of the paper, the induced voltage is

$$e = Blv \quad (6.3)$$

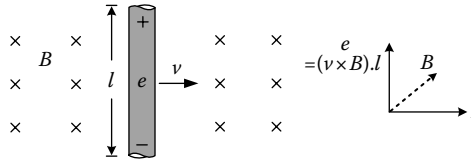


FIGURE 6.1
Induced voltage in a conductor.

6.1.1.2 Electromagnetic Force

A current-carrying conductor placed in a magnetic field experiences a force given by the Lorentz force equation. For a conductor-carrying current i in a uniform magnetic field \vec{B} , this electromagnetic force (emf) is given by

$$\vec{f} = i(\vec{l} \times \vec{B}) \tag{6.4}$$

Let us consider a magnetic field established by a pair of magnets and a conductor of length l carrying current i , as shown in Figure 6.2. The force in this case is

$$f = Bil \tag{6.5}$$

6.1.2 Simple DC Machine

Let us consider a simple one-turn loop placed in a magnetic field to understand the principles of voltage induced and torque developed. This magnetic field can be established by a magnet pole-pair directing flux from the North pole to the South pole, as shown in Figure 6.3a. The one-turn loop is placed in the gap between the pole-pair where it can freely rotate around a pivot axis under the influence of the magnetic field. The magnet pole-pair and the one-turn loop forms the simple electric machine that we will use to discuss the

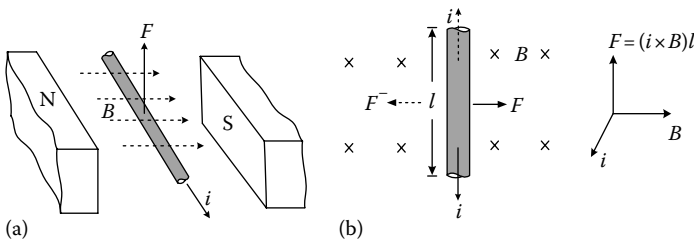


FIGURE 6.2
Force on a current-carrying conductor in a magnetic field; (a) magnets and conductor; (b) force, flux, and current directions.

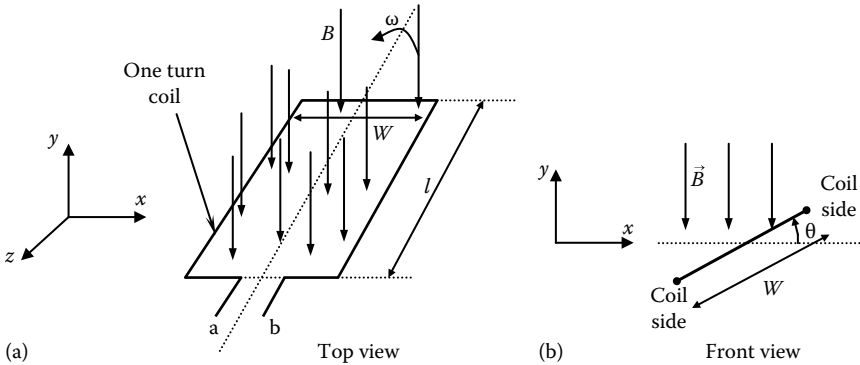


FIGURE 6.3
A one-turn coil in a magnetic field: (a) top view and (b) front view.

principles of electromagnetic energy conversion. Another view of the one-turn loop under the influence of the magnetic field is shown in Figure 6.3b. The one-turn coil cuts the magnetic field as it rotates around its pivot axis.

6.1.2.1 Induced Voltage

The one-turn rotating part of the simple machine is the rotor, while the permanent magnets (PMs) form the stator. The flux from the stator magnet pole-pair establish the magnetic field for the machine, which is known as the field flux. Let us assume that the flux established in between the magnet pole-pair is uniform, flowing from the North pole to South pole in the negative y -direction, as shown in Figure 6.3b. Now, if the single-turn conductor rotates in this uniform magnetic field at a constant angular velocity ω , a voltage will be induced in the sides of the coil according to Equation 6.1. The sides of the one-turn loop of length l , which passes under the pole faces, are called the *coil sides*. The side in the back of width W , which connects the coil sides, is known as the *end turn*. The one-turn coil rotating at an angular velocity of ω makes an angle θ with the magnetic field \vec{B} , as shown in the Figure 6.3a. The cross product $(\vec{v} \times \vec{B})$ for the coil sides at any instant of time is $vB\cos\theta$, and this resultant is always parallel with the length l of the coil sides. Therefore, the induced voltage in each of the coil sides is $vBl \cos\theta$ according to Equation 6.1. There will be no voltage induced on the end turn since $(\vec{v} \times \vec{B})$ is always perpendicular to the end turns that result in a zero dot product with the width W . Therefore, the total voltage induced in the one-turn loop accounting for the two coil sides and the end turn is

$$e_{ab} = 2vBl \cos\theta$$

Since the linear velocity v can be expressed in terms of the angular velocity ω as $v = \omega(W/2) = \omega r$, the voltage induced in the one-turn loop can be expressed as

$$e_{ab} = 2Blr\omega \cos \theta \quad (6.6)$$

The induced voltage can also be derived from the alternative form of Faraday's law ($e = -N(d\phi/dt)$) with the flux linkage for the one-turn coil expressed as

$$\phi(\theta) = -2Blr \sin \theta \quad (6.7)$$

The peak flux linking the coil is

$$\phi_p = 2Blr \quad (6.8)$$

The simple electric machine of Figure 6.3 will produce sinusoidal voltages when rotated at a constant speed in the uniform magnetic field. The alternating voltage generated at the terminals ab need to be rectified into unidirectional voltages to obtain a DC output. This is achieved with pairs of commutators and brushes attached at the ends of the one-turn conductor for the simple machine to produce a DC voltage (Figure 6.4). The commutators are connected to the ends of the turn and rotate with the coil. The brushes are stationary for connection with an external circuit. The two brushes are positioned in alignment with one of the stator magnetic poles such that they can collect the voltage created by that magnet pole and one of the coil sides through the commutator segment. The voltages seen by the brushes are thus unidirectional. The commutator and brush arrangement is a mechanical rectifier that converts the alternating voltage on the coil side e_{ab} into a unidirectional or DC voltage E_{12} . The field flux, the induced voltage, and the DC voltage are shown in Figure 6.5. The average DC voltage at the terminal of the brushes is

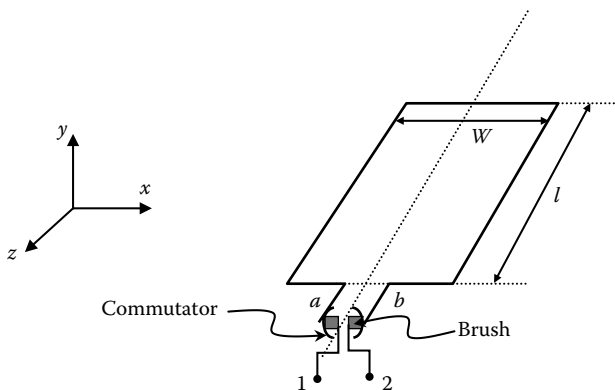


FIGURE 6.4
Commutators and brushes attached to the one-turn coil.

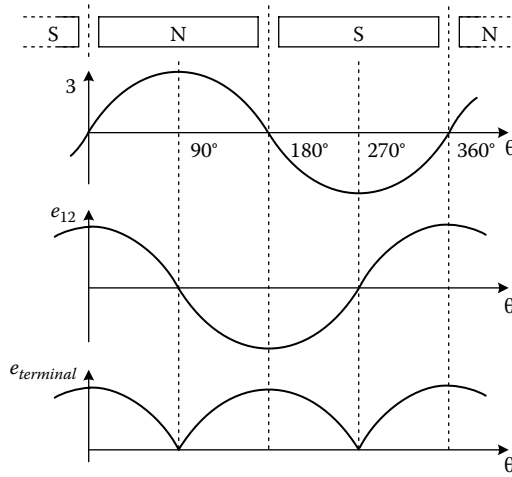


FIGURE 6.5
Field flux, induced voltage, and DC voltage.

$$E_{12} = \frac{2}{\pi} \int_{\pi/2}^{3\pi/2} \phi_P \omega \cos(\omega t) d(\omega t) = \frac{2}{\pi} \phi_P \omega \tag{6.9}$$

6.1.2.2 Force and Torque

In the one-turn coil of Figure 6.4, the circuit is open at the terminals 1–2. If a resistor is connected between the terminals 1–2, current starts to flow within the coil as long as there is motion of the conductor in the presence of the magnetic field. This current is the armature current in a DC machine; for the one-turn coil, the current for a resistance R is given by

$$I_a = \frac{e_{12}}{R} = \frac{2Blr}{R} \omega_m \cos \theta$$

The coil sides experience a force when current flows through the conductor according to Equation 6.5. The forces on the two coil sides, as shown in Figure 6.6, are given by

$$F_1 = F_2 = BI_a l$$

The electromagnetic torque of the machine can be derived from the two forces F_1 and F_2 forming a couple. The torque T_e on the armature turn about the axis-of-rotation is

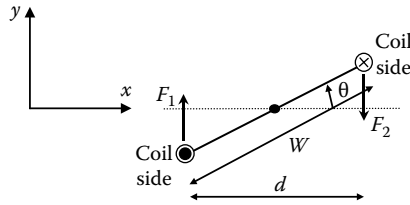


FIGURE 6.6
Forces on the coil sides due to current.

$$T_e = F_1 d = F_1 W \cos \theta$$

$$\Rightarrow T_e = \phi_p I_a \cos \theta$$

The average torque produced is

$$T_e = \frac{2}{\pi} \int_{\pi/2}^{3\pi/2} \phi_p I_a \cos(\omega t) d(\omega t) = \frac{2}{\pi} \phi_p I_a \quad (6.10)$$

6.1.2.3 DC Machine Back-EMF and Torque

In a practical machine, the coil would be wound around an iron structure which is the rotor of the electric machine. The rotor in the magnetic circuit is free to turn about the vertical axis. The reluctance of the iron is much smaller than the reluctance of the air. The rotor iron material must have much higher relative permeability than air to facilitate the flux flow from one stator pole to another through the rotor. The rotor iron, together with its curved shape, provides a constant width air gap between the stator and the rotor. The uniform air gap maintained between the stator and rotor poles allows the flux to be radially directed between the stator and the rotor.

The simple machine of Figure 6.3 is shown to have two poles only, one N-pole and one S-pole. The number "2" in Equation 6.9 represents those two poles in the machine. In a practical machine, there can be more than two poles, but always in pairs, for better utilization of the space around the stator and rotor circumference, and also for different torque–speed characteristics of the machine. In general, the higher speed machines will have few number of pole pairs, and higher torque machines will have more number of pole pairs. In addition, the machine geometry is better utilized when there are multiple turns in a coil instead of the single turn shown in Figure 6.3 for the simple machine. The multiple turns will increase the induced voltage. The multi-turn arrangement, known as the *conductor*, is shown in Figure 6.7. The sides of the turn along the z-direction are known as the *coil side* similar

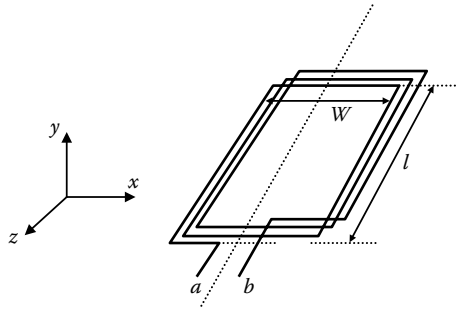


FIGURE 6.7
A multi-turn conductor.

to the one-turn coil. In the machine, many conductors are arranged radially along the rotor surface and connected in a series-parallel combination depending on the number of poles used. In DC machines, the conductor connectors are arranged in one of two winding patterns known as lap winding or wave winding. The induced voltage and torque equations for the simple machine can be generalized using the number of turns N_t in each conductor, the number of poles P , and the type of winding arrangement used. The equations then become

$$E_a = K_m \phi_P \omega \tag{6.11}$$

$$T_e = K_m \phi_P I_a \tag{6.12}$$

where K_m is a machine constant given by $K_m = N_t P / \pi a$, a is the number of parallel paths used in the conductor arrangement; $a = 2$ for wave winding, while $a = P$ for lap winding. E_a is the induced voltage or motional voltage, more commonly known as back-emf of the machine. Equation 6.12 shows that for the DC machine, the back-emf E_a is proportional to speed while the torque is proportional to current when the flux is held constant, since for a designed machine K_m is constant.

The end turns in a conductor, as was shown earlier, does not contribute to voltage generation or torque production, but contributes only to losses due to the resistances in that segment of the coil length. Therefore, one of the objectives in machine design is to minimize the end-turn lengths.

The flux in the simple machine shown is radially directed from the rotating component to the stationary component. The rotor rotates around the axis-of-rotation resulting in rotary motion. These machines are known as *radial flux machines*. Electric machines can also be constructed to deliver linear motion, which are known as *linear machines*. The movable component in a linear machine has linear or translator motion over the stationary structure.

6.1.3 Simple Reluctance Machine

The reluctance machines have a variable reluctance path for the magnetic flux as the rotor rotates about its axis-of-rotation. The saliencies in both the stator and the rotor poles provide a variable reluctance path for the magnetic flux as the rotor position changes. The windings are on the stationary member, while the rotor is a stack of laminations without any windings or magnets. A simple reluctance machine with only one phase is shown in Figure 6.8. The reluctance of the air gap varies as a function of the rotor angular displacement θ . The reluctance of the air gap is minimum when the rotor and the stator are in perfect alignment at $\theta=0^\circ$. The minimum reluctance position corresponds to the maximum inductance seen by the current flowing through the coil. The reluctance becomes maximum when the rotor attains the position with the largest air gap, which occurs when $\theta=90^\circ$. The inductance in this position is the minimum. The stator coil inductance variation as a function θ can be expressed by

$$L(\theta) = L_1 + L_2 \cos(2\theta)$$

The torque for the simple reluctance machine can be expressed as

$$T_e = \frac{1}{2} i^2 \frac{\partial L}{\partial \theta} \quad (6.13)$$

The single-phase simple reluctance machine operates as a synchronous machine when supplied with an AC voltage. The machine will produce torque as long as the stator excitation frequency is synchronized with the rotor speed. If the initial rotor position is δ , the rotor angular displacement for a rotor speed ω is given by

$$\theta = \omega t + \delta$$

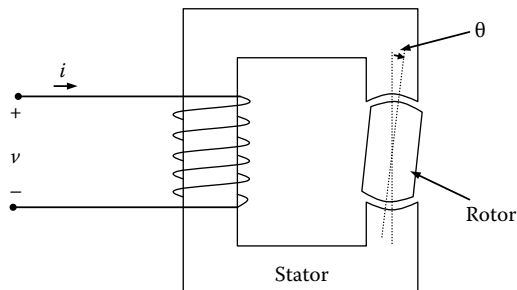


FIGURE 6.8

A simple reluctance machine.

The average torque produced for an excitation current of $i = I_m \cos \omega t$ at the synchronous speed is

$$T_e = -\frac{1}{4} L_2 I_m^2 \sin \delta$$

The simple reluctance machine will produce the average torque only at synchronous speed. The torque will be maximum when the initial position is 45° and zero when it is 0° . The machine will not be able to start rotation if the rotor is in the aligned position initially.

The reluctance machines used for high power applications are of multiple phases irrespective of whether they are of synchronous or switched types. Both the type of machines use power electronic inverters for controlling the torque and the speed of the machine. However, the fundamental principle for torque production is essentially the same as that described in this section with the simple reluctance machine. The principles and characteristics of the switched reluctance machines will be discussed further later in the chapter.

6.2 DC Machines

DC machines have two sets of windings, one in the rotor and the other in the stator, which establish the two fluxes; hence, the mmfs that interact with each other produce the torque. The orthogonality of the two mmfs, which is essential for maximum torque production, is maintained by a set of mechanical components called commutators and brushes. The winding in the rotor is called the *armature winding*, while the winding in the stationary part of the machine is called the *field winding*. Both the armature and the field windings are supplied with DC currents. The armature windings carry the bulk of the current, while the field windings carry a small field excitation current. The armature and the field currents in the respective windings establish the armature and field mmfs. The magnitude of the mmfs is the product of the number of turns in the windings and the current. Depending on the number of supply sources and the type of connection between the armature and field windings, there can be several types of DC machines. When the armature and field windings are supplied from independently controlled DC sources, then it is known as a separately excited DC machine. The separately excited DC machine offers the maximum flexibility of torque and speed control through independent control of the armature and field currents. The DC shunt machine has the similar parallel configuration of the armature and field windings as in the separately excited motor, except that the same DC source supplies both the armature and field windings. In the shunt motors, the simplicity in power supply is compromised for the reduced flexibility in

control. In another type of DC machine, known as the series DC machine, the armature and the series windings are connected in series and the machine is supplied from a single source. Since the armature and the field windings carry the same current, the field is wound with a few turns of heavy gauge wires to deliver the same mmf or ampere-turns as in the separately excited machine. The greatest advantage of the series machine is the very high starting torque that helps achieve rapid acceleration. However, the control flexibility is lost due to the series connection of armature and field windings.

The positive attributes of DC machines are

- Ease of control due to linearity
- Capability for independent torque and flux control
- Established manufacturing technology

The disadvantages of DC machines are

- Brush wear that leads to high maintenance
- Low maximum speed
- Electromagnetic interference (EMI) due to commutator action
- Low power-to-weight ratio

The separately excited DC motor used in an electric or hybrid electric vehicle has two separate DC/DC converters supplying the armature and field windings from the same energy source, as shown in Figure 6.9. The DC/DC converters process the fixed supply voltage of the energy source to deliver a variable DC to the armature and field circuits. The power rating of the converter supplying the armature windings is much larger than that of the converter supplying the field winding. The control inputs to the converter circuits are the desired torque and speed of the motor, and the outputs of the converters are the voltages that are applied to the armature and field circuits of the DC motor.

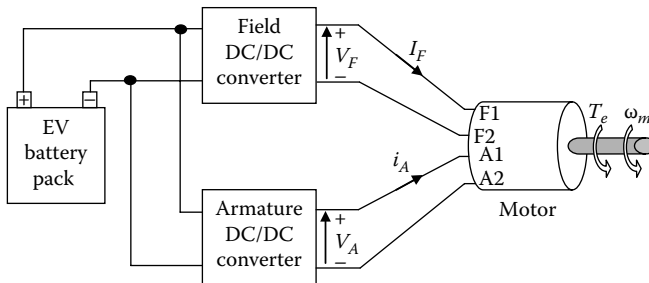


FIGURE 6.9

DC motor drive including the power electronics and battery source.

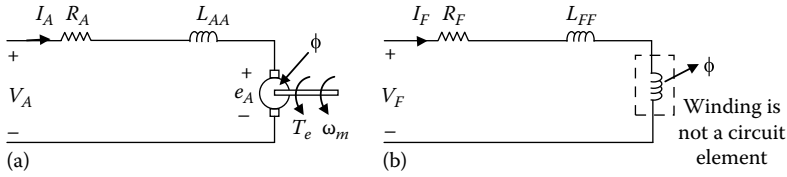


FIGURE 6.10 Equivalent circuit representation of a DC motor: (a) armature circuit; (b) field circuit.

The independent armature voltage and field current control, possible in separately excited DC machines or motors, offer the possibility of additional performance optimization in addition to meeting the torque–speed requirements of the machine. The indices used for measuring performance in motor drives include efficiency, torque per ampere, torque ripple, response time, etc. The weights on the individual performance indices depend on the application and the design requirements. The most critical performance index for electric and hybrid vehicle applications is the efficiency. The analysis to follow on DC motors, based on separately excited DC motors, is intended to set forth the premise for performance analysis of DC drives in the next chapter.

The armature equivalent circuit of a DC motor is shown in Figure 6.10a. The circuit consists of the armature winding resistance R_A , the self-inductance of armature winding L_{AA} , and the back-emf e_A . The variables shown in the figure are

- V_A = armature voltage
- I_A = armature current
- T_e = developed motor torque
- ω_m = shaft speed
- ϕ = armature linking flux (primarily from field current)

Applying Kirchhoff’s voltage law (KVL) around the armature circuit, the voltage balance equation is

$$V_A = R_A i_A + L_{AA} \frac{di_A}{dt} + e_A \tag{6.14}$$

where

$$\begin{aligned} e_A &= K\phi\omega_m \\ T_e &= K\phi i_A \end{aligned} \tag{6.15}$$

where

- e_A is known as the back-emf
- K is a machine constant that depends on the machine construction, number of winding, and core material properties

The field equivalent circuit of the DC motor is shown in Figure 6.10b. The field circuit consists of the field winding resistance R_F and the self-inductance of the field winding L_{FF} . V_F is the voltage applied to the field.

The field circuit equation is

$$V_F = R_F i_F + L_{FF} \frac{di_F}{dt}$$

The resistance of the field winding in separately excited and shunt DC motors is very high, since there are a lot of turns in the winding. The transient response in the field circuit is thus much faster than the armature circuit. The field voltage is also typically not adjusted frequently, and for all practical purposes, a simple resistor fed from a DC source characterizes the electrical unit of the field circuit. The field current establishes the mutual flux or field flux, which is responsible for torque production in the machine. The field flux is a nonlinear function of field current and can be described by

$$\phi = f(i_F)$$

The electromagnetic properties of the machine core materials is defined by the relationship

$$B = \mu H$$

where

B is the magnetic flux density in T or Wb/m²

H is the magnetic field intensity in A turn/m

μ is the permeability of the material

The permeability in turn is given by $\mu = \mu_0 \mu_r$, where $\mu_0 = 4\pi \times 10^{-7}$ H/m is the permeability of free space and μ_r is the relative permeability. The relative permeability of air is 1. The B - H relationship of magnetic materials is nonlinear and is difficult to describe by a mathematical function. Likewise, the field circuit of the DC machines is characterized by nonlinear electromagnetic properties of the core, which is made of ferromagnetic materials. The properties of core materials are often described graphically in terms of the B - H characteristics, as shown in Figure 6.11. The nonlinearity in the characteristics is due to the saturation of flux for higher currents and the hysteresis effects. When an external magnetization force is applied through the currents in the windings, the magnetic dipole moments tend to align to orient in a certain direction. This dipole orientation establishes a large magnetic flux,

which would not exist without the external magnetization force applied on the core. The magnetic dipole moments relax toward their random orientation up on removal of the applied magnetic force, but few dipole moments retain their orientation in the direction of the previously existing magnetization force. The retention of direction phenomenon of the dipole moments is known as magnetic hysteresis. The hysteresis causes magnetic flux density B to be a multivalued function that depends on the direction of magnetization. The magnetic effect that remains in the core after the complete removal of the magnetization force is known as the residual magnetism (denoted by B_r in Figure 6.11). The direction of the residual flux, as mentioned previously, depends on the direction of field current change. The B – H characteristics can also be interpreted as the ϕ – i_F characteristics, since B is proportional to ϕ and H is proportional to i_F for a given machine. The saturation in the characteristics reflects the fact that more magnetic dipole moments remain to be oriented once sufficient magnetization force has been applied and the flux has reached the maximum or saturation level.

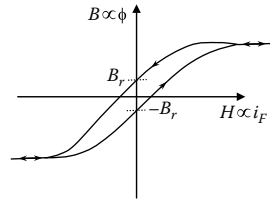


FIGURE 6.11 Typical DC motor magnetization characteristics.

The energy required to cause change in the magnetic orientations is wasted in the core material and is referred to as hysteresis loss. The area of the hysteresis loop in the magnetization characteristics is proportional to the hysteresis loss.

For most applications, it is sufficient to show the magnetic properties of core materials through a single-valued, yet nonlinear function, which is known as the DC magnetization curve. The magnetization curve of a DC machine is typically shown as a curve of open-circuit-induced voltage E_0 versus field current i_F at a particular speed. The open-circuit-induced voltage is nothing but the back-emf e_A , which is linearly proportional to the flux at a constant speed (refer to Equation 6.15). Therefore, the shape of this characteristic, shown in Figure 6.12, is similar to that of the magnetic characteristics of the core material.

The torque–speed relationship of a DC motor can be derived from Equations 6.14 and 6.15 and is given by

$$\omega_m = \frac{V_A}{K\phi} - \frac{R_A}{(K\phi)^2} T_e \tag{6.16}$$

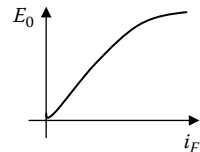


FIGURE 6.12 Magnetization characteristics of DC machines.

The torque–speed characteristic is shown in Figure 6.13. The positive torque axis represents the motoring characteristics, while the negative torque region represents the generating characteristics. The

torque–speed characteristic is adjusted through either the armature voltage or the field current. For a given speed and torque (i.e., a point (T^*, ω_m^*) in the ω - T plane), there are an infinite number of corresponding armature voltage and field current, as shown in Figure 6.14a that would satisfy Equation 6.16. A possible control design is one that optimizes one or more performance indices and operates the motor on the optimized characteristic curve. To follow up on the concept, let us assume that the controller can set both the field current and the armature voltage and we are interested in minimizing the loss in the machine. The driver input commands set the desired torque and speed (T^*, ω_m^*) of the machine. Inserting the operating point in the armature voltage Equation 6.14, we have

$$V_A = R_A I_A^* + K\phi\omega_m^*$$

$$\Rightarrow V_A = \frac{R_A}{K\phi} T^* + K\phi\omega_m^* \quad \text{or} \quad \omega_m^* K^2 \phi^2 - V_A K\phi + R_A T^* = 0 \quad (6.17)$$

Equation 6.17 gives all the possible combinations of armature voltage and field flux that will give the same operating point (T^*, ω_m^*) . The possible combinations are shown graphically in Figure 6.14b. The optimization algorithm will select the right combination of V_A and ϕ that will minimize the losses. The loss in DC machines is minimized when armature circuit-dependent losses equal the field circuit dependent losses [1]. Knowing the machine parameters, V_A and ϕ commands can be set such that the armature circuit losses equals the field circuit losses to minimize the overall loss, hence maximizing the efficiency.

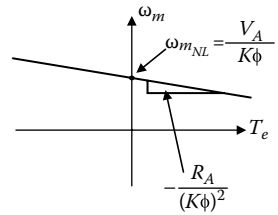


FIGURE 6.13
Torque–speed characteristics of a DC motor.

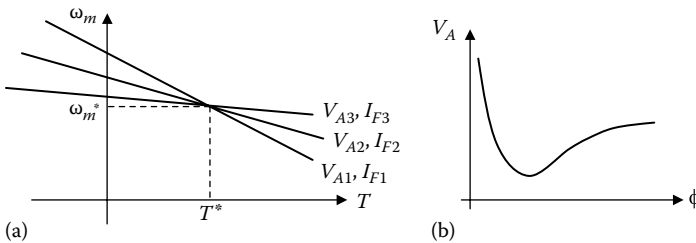


FIGURE 6.14
(a) Steady-state operating point. (b) Required armature voltage vs. flux at a fixed operating point.

6.3 Three-Phase AC Machines

The primary difference between AC and DC machines is that the armature circuit of the former is located in the stationary piece of the structure while for the latter it is in the rotor. The advantage gained in having the armature circuit in the stator is the elimination of the commutator and brushes of the DC machines. The AC machines require alternating supply that can be derived from a DC source using a DC/AC inverter. The machines can be single-phase or multiple-phase types. Single-phase AC machines are used for low-power appliance applications, while higher power machines are always of three-phase configuration. The second mmf required for torque production in AC machines (equivalent to the field mmf of DC machines) comes from the rotor circuit. Depending on the way the second mmf is established, the AC machines can be induction type or synchronous type. For either of the two types of AC machines, the stator windings are similar in configuration.

6.3.1 Sinusoidal Stator Windings

The three-phase stator windings of AC machines are sinusoidally distributed spatially along the stator circumference, as shown in Figure 6.15a to establish a sinusoidal mmf waveform. Although the windings are shown as concentrated in locations aa' , bb' , and cc' for the three phases, the number of turns for each of the phase windings vary sinusoidally along the stator circumference. This space sinusoidal distribution of Phase-a winding is shown in Figure 6.15b, which has been represented by an equivalent concentrated winding $a-a'$ in Figure 6.15a. The equivalent distribution of Phase-a windings in a horizontally laid stator axis as if the stator cross section was split along the radius at $\theta=0$ and developed longitudinally is shown in Figure 6.16a. The current passing through these Phase-a stator windings causes a sinusoidal

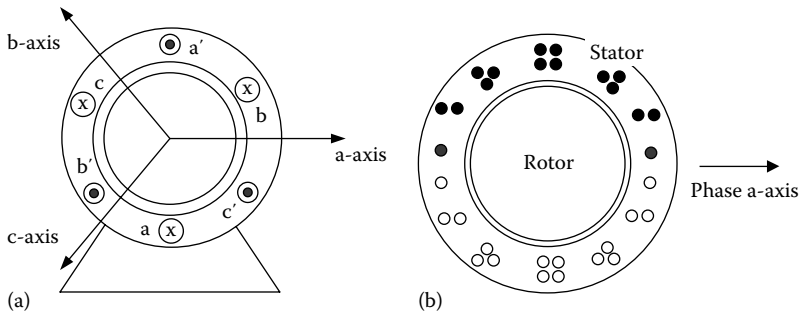
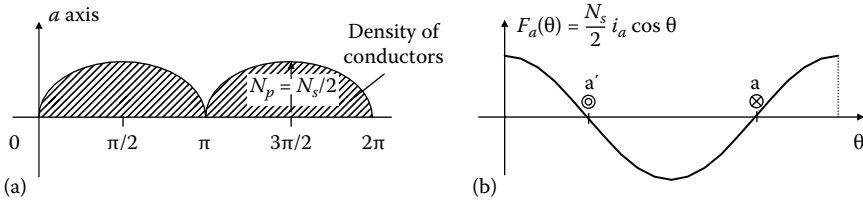


FIGURE 6.15 (a) Three-phase winding and magnetic axes of an AC machine. (b) Sinusoidal distribution of Phase-a winding along the stator circumference.

**FIGURE 6.16**

(a) Equivalent distribution of Phase-a winding; (b) mmf distribution of Phase a.

Phase-a mmf $F_a(\theta)$, which is shown in Figure 6.16b. The mmf primarily exists in the air gap due to the high permeability of the stator and rotor steel and tends to be radial in direction due to the short length of air gap relative to stator inside diameter. The sinusoidal distribution of the windings can be expressed as

$$\begin{aligned} n_{as}(\theta) &= N_p \sin \theta, & 0 \leq \theta \leq \pi \\ &= -N_p \sin \theta, & \pi \leq \theta \leq 2\pi \end{aligned}$$

where N_p is the maximum turns or conductor density expressed in turns per radian. Suppose Phase-a winding has an N_s equivalent number of turns (i.e., $2N_s$ conductors), which would give the same fundamental sinusoidal component as the actual winding distribution. Therefore, the integral of the conductor density in Figure 6.16b between 0 and π has a total of N_s conductors (accounting for half the turns in a winding-half), which is

$$\begin{aligned} N_s &= \int_0^{\pi} N_p \sin \theta d\theta = 2N_p \\ \Rightarrow N_p &= \frac{N_s}{2} \end{aligned}$$

The sinusoidal conductor–density distribution in Phase-a winding is

$$n_s(\theta) = \frac{N_s}{2} \sin \theta, \quad 0 \leq \theta \leq \pi \quad (6.18)$$

The equivalent conductor–density is used to calculate the air gap magnetic field parameters, which consist of field intensity, flux density, and mmf. The basic relationship between magnetic field intensity H and current i is given by Ampere’s law, which states that the line integral of H around a closed path is equal to the net current enclosed $\left(\oint H \cdot dl = \sum Ni \right)$. $\sum Ni$ is the ampere-turn product defining the net current enclosed and is known as the total mmf

in magnetic circuit terms. The radial magnetic field intensity H_a in the AC machine under discussion is established in the air gap when current i_a flows through Phase-a windings, which can be derived using Ampere's law as

$$H_a(\theta) = \frac{N_s}{2l_g} i_a \cos \theta$$

where l_g is the length of the air gap. The flux density $B_a(\theta)$ and mmf $F_a(\theta)$ can be derived as

$$B_a(\theta) = \mu_0 H_a(\theta) = \frac{\mu_0 N_s}{2l_g} i_a \cos \theta$$

where μ_0 is the permeability of free space or air and

$$F_a(\theta) = l_g H_a(\theta) = \frac{N_s}{2} i_a \cos \theta \quad (6.19)$$

The mmf, flux intensity, and field intensity are all 90° phase shifted in space with respect to the winding distribution. The angle θ is measured in the counterclockwise direction with respect to the Phase-a magnetic axis. The field distribution shown in Figure 6.16b is for positive current. Irrespective of the direction of current, the peak of the mmf (positive or negative) will always appear along the Phase-a magnetic axis, which is the characteristic of mmf produced by a single-phase winding.

6.3.2 Number of Poles

The two equivalent Phase-a conductors in Figure 6.15a represent two poles of the machine. Electric machines are designed with multiple pairs of poles for the efficient utilization of the stator and rotor magnetic core material. In multiple pole-pair machines, the electrical and magnetic variables (such as induced voltages, mmfs, and flux densities) complete more cycles during one mechanical revolution of the motor. The electrical and mechanical angles of revolution and the corresponding speeds are related by

$$\begin{aligned} \theta_e &= \frac{P}{2} \theta_m \\ \omega_e &= \frac{P}{2} \omega_m \end{aligned} \quad (6.20)$$

where P is the number of poles. The four-pole machine cross section is represented, as shown in Figure 6.17a, while the Phase-a mmf F_a as a function of θ_e or θ_m is illustrated in Figure 6.17b. The mmf is mathematically represented as

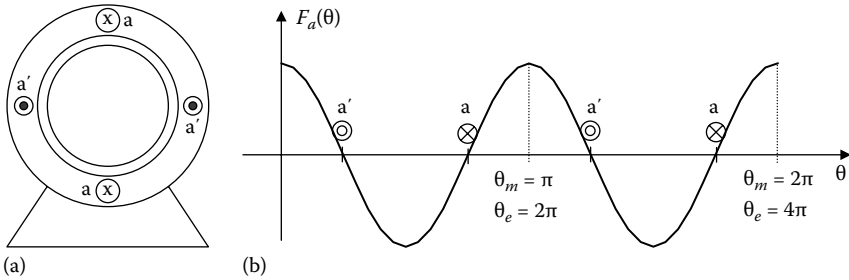


FIGURE 6.17

(a) Cross-section of a four-pole machine showing Phase-a windings only. (b) Phase-a mmf distribution.

$$F_a(\theta_e) = \frac{N_s}{P} i_a \cos(\theta_e) \quad (6.21)$$

6.3.3 Three-Phase Sinusoidal Windings

Phases b and c of the three-phase machine have identical sets of windings as the Phase-a winding described in Section 6.3.2, except that they are displaced 120° spatially with respect to each other, as shown in Figure 6.15a. The resulting mmfs due to currents in phases b and c can be expressed as

$$\begin{aligned} F_b(\theta) &= \frac{N_s}{2} i_b \cos\left(\theta - \frac{2\pi}{3}\right) \\ F_c(\theta) &= \frac{N_s}{2} i_c \cos\left(\theta + \frac{2\pi}{3}\right) \end{aligned} \quad (6.22)$$

6.3.4 Space Vector Representation

The extensive amount of coupling existing among the circuits of three-phase AC machines makes the analysis a formidable task. Axes transformations or reference frame theory is necessary to decouple the voltage expressions of the phases as well as to implement control algorithms that achieve the best performance. The *space vector representation* is a convenient method of expressing the equivalent resultant effect of the sinusoidally space-distributed electrical and magnetic variables in AC machines, in a way that is similar to the use of phasors in describing the sinusoidally time-varying voltages and currents in electrical circuits. The space vectors provide a very useful and compact form of representing the machine equations, which not only simplifies the representation of three-phase variables, but also facilitates the transformation between three-phase and two-phase variables. The two-phase system is an equivalent representation of the three-phase variables in a dq (two-axis)

coordinate system, which is necessary for control implementation. The dq coordinate system will be elaborated in Section 9.2.

The concept of reference frame transformations originates from Park's transformations [2], which provided a revolutionary new approach of analyzing three-phase electric machines by transforming three-phase variables (voltages, currents, and flux linkages) into two-phase variables with the help of a set of two fictitious windings (known as dq windings) rotating with the rotor. The notations of space vector evolved later as a compact set of representation of the three-phase machine variables either in the three-phase abc reference frame or in the fictitious two-phase dq reference frame [3–5]. The space vectors are more complex than the phasors, since they represent time variation as well as space variation. The space vectors, just like any other vectors, have a magnitude and an angle, but the magnitude can be time varying. For example, the stator mmfs of the three phases in the AC machine can be represented by space vectors as

$$\begin{aligned}\vec{F}_a(t) &= \frac{N_s}{2} i_a(t) \angle 0^\circ \\ \vec{F}_b(t) &= \frac{N_s}{2} i_b(t) \angle 120^\circ \\ \vec{F}_c(t) &= \frac{N_s}{2} i_c(t) \angle 240^\circ\end{aligned}\quad (6.23)$$

Note that space vectors are complex numbers and “ \rightarrow ” is used to denote the vector characteristic. The time dependence is also explicitly shown. The magnitude of the vector represents the positive peak of the sinusoidal spatial distribution, and the angle represents the location of the peak with respect to the Phase-a magnetic axis (chosen by convention). The space vectors of the individual phases can now be added conveniently by vector addition to give the resultant stator mmf as

$$\vec{F}_s(t) = \vec{F}_a(t) + \vec{F}_b(t) + \vec{F}_c(t) = \hat{F}_s \angle \theta_F \quad (6.24)$$

where

\hat{F}_s is the stator mmf space vector amplitude

θ_F is the spatial orientation with respect to the Phase-a reference axis

In general, if f represents a variable (mmf, flux, voltage, or current) in a three-phase AC machine, the corresponding resultant space vector can be calculated as

$$\vec{f}_{abc}(t) = f_a(t) + af_b(t) + a^2 f_c(t)$$

where

$f_a(t)$, $f_b(t)$, and $f_c(t)$ are the magnitudes of the phase space vectors of the variables

a and a^2 are spatial operators that handle the 120° spatial distribution of the three windings, one with respect to the other along the stator circumference

The operators a and a^2 are $a = e^{j2\pi/3}$ and $a^2 = e^{j4\pi/3}$, and hence, the space vector can also be represented as

$$\vec{f}_{abc}(t) = f_a(t) + f_b(t)\angle 120^\circ + f_c(t)\angle 240^\circ \quad (6.25)$$

The space vector can be used to represent any of the AC machine sinusoidal variables either in the stator circuit or in the rotor circuit. For example, the flux density, current, and voltage space vectors of the stator can be expressed as

$$\begin{aligned} \vec{B}_S(t) &= \frac{\mu_0 N_S}{2l_g} i_a(t) + \frac{\mu_0 N_S}{2l_g} i_b(t)\angle 120^\circ + \frac{\mu_0 N_S}{2l_g} i_c(t)\angle 240^\circ = \hat{B}_S \angle \theta_B \\ \vec{i}_S(t) &= i_a(t) + i_b(t)\angle 120^\circ + i_c(t)\angle 240^\circ = \hat{I}_S \angle \theta_I \\ \vec{v}_S(t) &= v_a(t) + v_b(t)\angle 120^\circ + v_c(t)\angle 240^\circ = \hat{V}_S \angle \theta_V \end{aligned} \quad (6.26)$$

The space vector \vec{f}_{abc} for a balanced set of three-phase variables f_a , f_b , and f_c has a magnitude $3/2$ times greater than the magnitude of the phase variables; its spatial orientation is at an angle ωt at time t with respect to the reference Phase-a axis. Here, ω is the angular frequency of the phase variables. Therefore, the amplitude of the space vector is constant for a balanced set of variables, but the phase angle (i.e., the spatial orientation) is a function of time. The space vector at any instant of time can be obtained by the vector sum of the three-phase variables, as shown in Figure 6.18 for stator currents. Note that there is a unique set of phase variables that would sum up to give the resultant space vector \vec{f}_{abc} since $f_a + f_b + f_c = 0$ for a balanced set of variables. Some examples with numerical values are given in the following to supplement the theory.

Example 6.1

The stator currents of a three-phase machine at $\omega t = 40^\circ$ are

$$\begin{aligned} i_a &= 10 \cos 40^\circ = 7.661 \text{ A} \\ i_b &= 10 \cos(40^\circ - 120^\circ) = 1.74 \text{ A} \\ i_c &= 10 \cos(40^\circ - 240^\circ) = -9.4 \text{ A} \end{aligned}$$

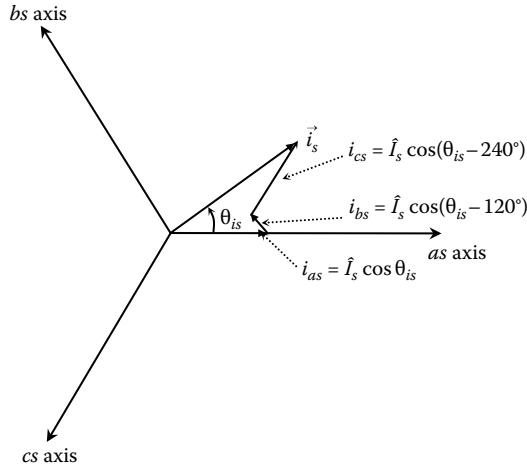


FIGURE 6.18 Space vector and its components in *abc* reference frame.

Calculate the resultant space vector.

Solution

The space vector at $\omega t = 40^\circ$ is

$$\begin{aligned} \vec{i}_s &= i_a(t) + i_b(t)\angle 120 + i_c(t)\angle 240 \\ &= 7.66 + 1.74\angle 120 + (-9.4)\angle 240 \\ &= \frac{3}{2}(7.66 + j6.43) \\ &= \frac{3}{2} \cdot 10\angle 40 \text{ A} \end{aligned}$$

The projection of \vec{i}_s on the phase-a axis is $15 \cos 40 = 11.49$, which is $3/2$ times i_a .

Example 6.2

- (a) The phase voltage magnitudes of a three-phase AC machine at time $\omega t = 0$ are $v_a = 240 \text{ V}$, $v_b = -120 \text{ V}$, and $v_c = -120 \text{ V}$. Calculate the resulting space vector voltage.
- (b) Recalculate the space vector at a different time when $v_a = 207.8 \text{ V}$, $v_b = 0 \text{ V}$, and $v_c = -207.8 \text{ V}$.
- (c) Plot the space vector distribution in the air gap in the two cases.

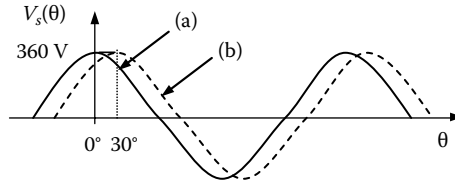


FIGURE 6.19
Plot of space vectors for Example 6.2 (a) and (b).

Solution

- (a) The resulting space vector using Equation 6.25 is

$$\begin{aligned}\vec{v}_S(t) &= v_a(t) + v_b(t)\angle 120^\circ + v_c(t)\angle 240^\circ \\ \Rightarrow \vec{v}_S(t_0) &= 240 + (-120)(\cos 120^\circ + j \sin 120^\circ) + (-120)(\cos 240^\circ + j \sin 240^\circ) \\ &= 360\angle 0^\circ \text{ V}\end{aligned}$$

- (b) The resulting space vector using Equation 6.25 is

$$\begin{aligned}\vec{v}_S(t) &= v_a(t) + v_b(t)\angle 120^\circ + v_c(t)\angle 240^\circ \\ \Rightarrow \vec{v}_S(t_0) &= 207.8 + (0)(\cos 120^\circ + j \sin 120^\circ) + (-207.8)(\cos 240^\circ + j \sin 240^\circ) \\ &= 360\angle 30^\circ \text{ V}\end{aligned}$$

- (c) The plot is given in Figure 6.19.

Example 6.3

The phase voltage magnitudes of a three-phase AC machine at time t_0 are $v_a = 240 \text{ V}$, $v_b = 50 \text{ V}$, and $v_c = -240 \text{ V}$. Calculate the resulting space vector voltage and plot the space vector distribution in the air gap.

Solution

The resulting space vector using Equation 6.25 is

$$\begin{aligned}\vec{v}_S(t) &= v_a(t) + v_b(t)\angle 120^\circ + v_c(t)\angle 240^\circ \\ \Rightarrow \vec{v}_S(t_0) &= 240 + (50)(\cos 120^\circ + j \sin 120^\circ) + (-240)(\cos 240^\circ + j \sin 240^\circ) \\ &= 418.69\angle 36.86^\circ \text{ V}\end{aligned}$$

The voltage space vector and its sinusoidal plot is shown in Figure 6.20.

The voltages given in Example 6.2 are a balanced set at two different times which correspond to $\omega t = 0$ and $\omega t = 30^\circ$ for parts (a) and (b), respectively. The peak magnitude of the resulting voltage space vector remain the same in the two cases

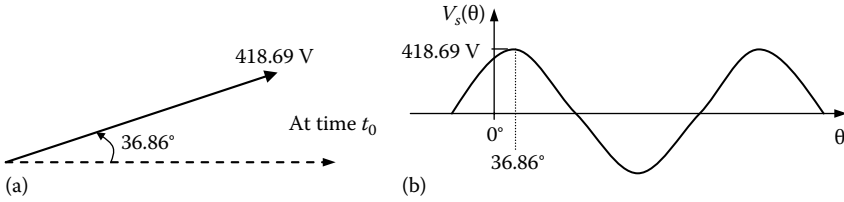


FIGURE 6.20 (a) Resultant voltage space vector; (b) voltage space vector sinusoidal distribution in the air gap at t_0 .

and the location of these peaks along the machine axes are at $\theta=0^\circ$ and $\theta=30^\circ$, which corresponds to the time dependence of the voltages. This is not coincidental, but will be so for a balanced set of voltages. In Example 6.3, the voltages are unbalanced and the magnitude of the space vector depends on instantaneous values of the phase voltages.

6.3.4.1 Interpretation of Space Vectors

The space vectors, through one convenient and compact vector form, express the same resultant effect that the three individual phase variables would produce. For example, the stator mmf distribution in the air gap is a result of three phase currents i_a , i_b , and i_c , while the equivalent space vector current $\vec{i}_s(t)$ is developed in such a way that this resultant current flowing through an equivalent winding of N_s turns would produce the same resultant mmf distribution.

The relationships between electrical and magnetic quantities are conveniently expressed with the help of space vectors. Using Equations 6.23, 6.24, and 6.26, we can write

$$\vec{F}_s(t) = \frac{N_s}{2} \vec{i}_s(t) \tag{6.27}$$

The mmf and current vector magnitudes are related by the scalar constant $N_s/2$ and they have the same angular orientation.

The flux density can be similarly shown to be

$$\vec{B}_s(t) = \frac{\mu_0 N_s}{2l_g} \vec{i}_s(t) \tag{6.28}$$

6.3.4.2 Inverse Relations

The phase quantities can be derived from the space vectors through the inverse relations established using the complex variable mathematics. We know that

$$|A|\angle\theta = |A|\cos\theta + j|A|\sin\theta$$

Applying this to (6.25), we get

$$\vec{f}_{abc}(t) = f_a(t) - \frac{1}{2}(f_b(t) + f_c(t)) + j\frac{\sqrt{3}}{2}(f_b(t) - f_c(t)) = \frac{3}{2}f_a(t) + j\frac{\sqrt{3}}{2}(f_b(t) - f_c(t))$$

since $f_a(t) + f_b(t) + f_c(t) = 0$ for balanced three-phase systems and for circuits without a neutral connection. Therefore, the inverse relation for Phase-a variable is

$$f_a(t) = \frac{2}{3} \operatorname{Re} \left[\vec{f}_{abc}(t) \right] \quad (6.29)$$

Similarly, it can be shown that

$$f_b(t) = \frac{2}{3} \operatorname{Re} \left[\vec{f}_{abc}(t) \angle 240^\circ \right] \quad (6.30)$$

and

$$f_c(t) = \frac{2}{3} \operatorname{Re} \left[\vec{f}_{abc}(t) \angle 120^\circ \right] \quad (6.31)$$

6.3.4.3 Resultant mmf in a Balanced System

In the typical operation of an AC machine, the stator windings are supplied with a balanced set of voltages, and since the windings are electrically symmetrical, a balanced set of currents flows through the windings. Let us assume that the rotor is open circuited and all the current that is flowing through the stator winding is the magnetizing current required to establish the stator mmf. The three-phase currents have the same magnitude and frequency, but are 120° shifted in time with respect to each other. The currents in the time domain can be expressed as

$$\begin{aligned} i_a(t) &= \hat{I}_M \cos \omega t \\ i_b(t) &= \hat{I}_M \cos(\omega t - 120^\circ) \\ i_c(t) &= \hat{I}_M \cos(\omega t - 240^\circ) \end{aligned} \quad (6.32)$$

The space vector for the above balanced set of currents is (using Equation 6.25)

$$\vec{i}_M(t) = \frac{3}{2} \hat{I}_M \angle \omega t \tag{6.33}$$

The resultant stator mmf space vector is

$$\vec{F}_{ms}(t) = \frac{N_s}{2} \vec{i}_M(t) = \frac{3}{2} \frac{N_s}{2} \hat{I}_M \angle \omega t = \hat{F}_{ms} \angle \omega t \tag{6.34}$$

The result shows that the stator mmf has a constant peak amplitude \hat{F}_{ms} (since N_s and \hat{I}_M are constants) that rotates around the stator circumference at a constant speed equal to the angular speed of the applied stator voltages. This speed is known as the synchronous speed. Unlike the single-phase stator mmf (shown in Figure 6.16b), the peak of the stator mmf resulting in the three-phase AC machine is rotating synchronously along the stator circumference with the peak always located at $\theta = \omega t$. The mmf peak position is time-varying for the three-phase winding, whereas the peak mmf position for the single-phase winding is *not* time-varying. The mmf wave is a sinusoidal function of the space angle θ . The wave has constant amplitude and a space-angle ωt , which is linear with respect to time. The angle ωt provides rotation of the entire wave around the air gap at a constant angular velocity ω . Thus, at a fixed time t_x the wave is a sinusoid in space with its positive peak displaced ωt_x from the reference $\theta = 0$. The resultant space vector at three different times is shown in Figure 6.21. The polyphase windings excited by balanced polyphase currents produce the same general effect as that of spinning a PM about an axis perpendicular to the magnet, or as in the rotation of the DC-excited field poles.

The three-phase stator mmf is known as the rotating mmf, which can be equivalently viewed as a magnet rotating around the stator circumference at a constant speed. Note that with the vector sum of $F_a(\theta)$, $F_b(\theta)$, and $F_c(\theta)$, as described in Equations 6.21 and 6.22, with $i_a(t)$, $i_b(t)$, and $i_c(t)$ replaced by the balanced set of Equation 6.32, we will arrive at the same result.

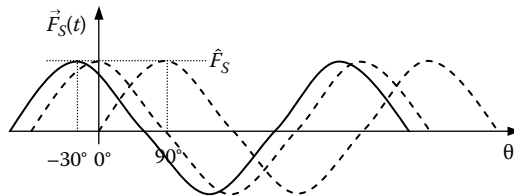


FIGURE 6.21
Resultant mmf space vector for $\omega t = -30^\circ, 0^\circ,$ and 90° .

Exercise 6.1

Show that $F_a(\theta_e) + F_b(\theta_e) + F_c(\theta_e) = \frac{3}{2} \frac{N_S}{2} \hat{I}_M \angle \omega t$ with

$$i_a(t) = \hat{I}_M \cos \omega t$$

$$i_b(t) = \hat{I}_M \cos(\omega t - 120^\circ)$$

$$i_c(t) = \hat{I}_M \cos(\omega t - 240^\circ)$$

6.3.4.4 Mutual Inductance L_m and Induced Stator Voltage

In an ideal situation, the equivalent electrical circuit for the stator windings with no rotor existing consists of the applied stator voltage source and a set of winding that is represented by an inductance known as magnetizing or mutual inductance. The practical circuit extends on this ideal circuit by adding the stator winding resistance and the stator leakage inductance in series with the magnetizing inductance. The magnetizing inductance for the three-phase AC machine, including the effects of mutual coupling among the three phases, can be shown to be [4,5]

$$L_m = \frac{3}{2} \left[\frac{\pi \mu_0 r l}{l_g} \left(\frac{N_S}{2} \right)^2 \right] \quad (6.35)$$

where

r is the radius to the air gap

l is the rotor axial length

l_g is the air gap length

Note that the form of Equation 6.35 is the same as that of a simple inductor given by $L = N^2/\mathfrak{R}$, where N is the number of turns and $\mathfrak{R} = \text{Reluctance} = (\text{flux-path length})/(\mu \times \text{cross-sectional area})$. The voltage induced in the stator windings due to the magnetizing current flowing through L_m in space vector form is

$$\vec{e}_{ms}(t) = j\omega L_m \vec{i}_M(t) \quad (6.36)$$

The magnetizing flux density $\vec{B}_{ms}(t)$ established by the magnetizing current $\vec{i}_M(t)$ is (from Equation 6.28)

$$\vec{B}_{ms}(t) = \frac{\mu_0 N_S}{2l_g} \vec{i}_M(t)$$

which gives

$$\vec{i}_M(t) = \frac{2l_g}{\mu_0 N_S} \vec{B}_{ms}(t) \quad (6.37)$$

Using the expression for L_m from Equation 6.35 and the expression for $\vec{i}_M(t)$ in terms of $\vec{B}_{ms}(t)$, the induced voltage is

$$\vec{e}_{ms}(t) = j\omega \frac{3}{2} \pi r l \frac{N_S}{2} \vec{B}_{ms}(t)$$

The induced voltage can be interpreted as the back-emf induced by the flux density B_{ms} , which is rotating at the synchronous speed. For a P -pole machine, the expression for the induced voltage is

$$\vec{e}_{ms}(t) = j\omega \frac{3}{2} \pi r l \frac{N_S}{P} \vec{B}_{ms}(t) \quad (6.38)$$

6.3.5 Types of AC Machines

The second rotating mmf needed for torque production in AC machines is established by the rotor circuit. The interaction of the two rotating mmfs, essentially chasing each other at synchronous speed, is what produces torque. The method through which the rotor mmf is established differentiates the different types of AC machines. Broadly, the AC machines can be classified into two categories, synchronous machines and asynchronous machines. In synchronous machines, the rotor always rotates at synchronous speed. The rotor mmf is established either by using a PM or an electromagnet created by feeding DC currents into a rotor coil. The latter-type synchronous machines are typically the large machines that are used in electric power generating systems. The PM machines are more suitable for the electric and hybrid vehicle applications, since these offer higher power density and superior performance compared to the rotor-fed synchronous machines. The several types of PM AC machines will be discussed later in the chapter. The rotor-fed synchronous machines will not be discussed further in this book, since these are not of interest for the electric and hybrid vehicle applications. In the asynchronous-type AC machine, the rotor rotates at a speed that is close to but different from the synchronous speed. These machines are known as induction machines, which in the more common configurations are fed only from the stator. The voltages in the rotor circuit are induced from the stator, which in turn induces the rotor rotating mmf, and hence the name induction machines. The induction machines that are generally labeled as AC machines are the subject of treatment in the following section.

6.4 Induction Machines

The two types of induction machines are the squirrel cage induction machines and the wound rotor induction machines. The squirrel cage induction machines are the workhorse of the industry, because of their rugged construction and low cost. The rotor windings consist of short-circuited copper bars that form the shape of a squirrel cage. The squirrel cage of an induction motor is shown in Figure 6.22. The rotor winding terminals of the wound rotor induction machines are brought outside with the help of slip rings for external connections, which are used for speed control. The squirrel cage induction motors are of greater interest for electric and hybrid vehicles and most other general purpose applications, and hence, are discussed further.

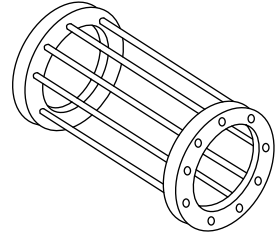


FIGURE 6.22
The squirrel cage of an induction motor.

The stator windings of the induction machines are exactly the same as that discussed in the previous section. The rotor, usually made of stacked laminations, has copper or aluminum rotor bars molded around the periphery in axial direction. The bars are short-circuited at the ends through electrically conducting end rings. The electrical equivalent circuit of a three phase induction machine along with the direction of Phase-a stator and rotor magnetic axes are shown in Figure 6.23. The rotor windings have been short-circuited and the angle between the rotor and stator axes is θ_r , which is the integral of the rotor speed ω_r .

When a balanced set of voltages is applied to the stator windings, a magnetic field is established which rotates at synchronous speed, as described in Section 6.3.4. By Faraday’s law, as long as the rotor rotates at a speed other

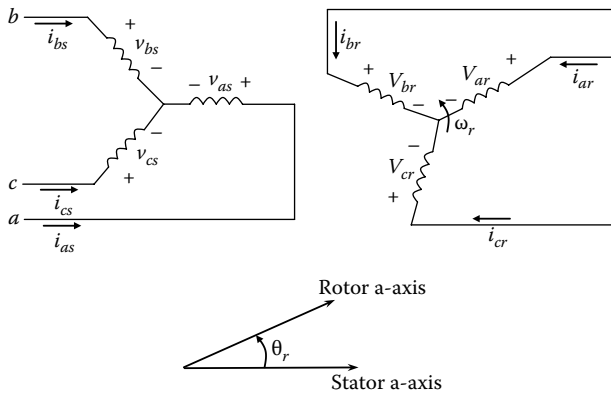


FIGURE 6.23
Stator and rotor electric circuit and magnetic axes of three-phase induction machine.

than the synchronous speed (even at zero rotor speed), the rotor conductors are cutting the stator magnetic field and there is a rate of change of flux in the rotor circuit, which will induce a voltage in the rotor bars. This is also analogous to transformer action where a time-varying AC flux established by the primary winding induces voltage in the secondary set of windings. The induced voltage will cause rotor currents to flow in the rotor circuit, since the rotor windings or bars are short-circuited in the induction machine. The induction machine can be thought of as a transformer with a short-circuited secondary or rotor windings. The rotor-induced voltages and the current have a sinusoidal space distribution, since these are created by the sinusoidally varying (space sinusoids) stator magnetic field. The resultant effect of the rotor bar currents is to produce a sinusoidally distributed rotor mmf acting on the air gap.

The difference between the rotor speed and the stator synchronous speed is the speed by which the rotor is slipping from the stator magnetic field, and is known as the slip speed:

$$\omega_{slip} = \omega_e - \omega_m \quad (6.39)$$

where

ω_e is the synchronous speed

ω_m is the motor or rotor speed

The slip speed expressed as a fraction of the synchronous speed is known as the slip:

$$s = \frac{\omega_e - \omega_m}{\omega_e} \quad (6.40)$$

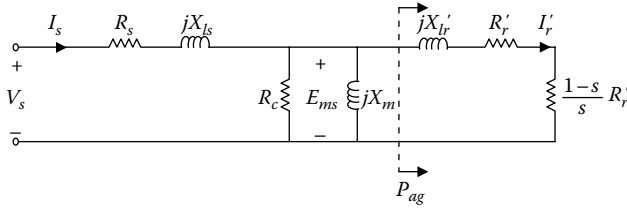
The rotor bar voltage, current, and magnetic field are of the slip speed or slip frequency with respect to the rotor. The slip frequency is given by

$$f_{slip} = \frac{\omega_e - \omega_m}{2\pi} = sf, \quad \text{where } f = \frac{\omega_e}{2\pi} \quad (6.41)$$

From the stator perspective, the rotor voltages, currents, and rotor mmfs all have the synchronous frequency, since the rotor speed of ω_m is superimposed on the rotor variables' speed of ω_{slip} .

6.4.1 Per-Phase Equivalent Circuit

The steady-state analysis of induction motors is often carried out using the per-phase equivalent circuit. A single-phase equivalent circuit is used for the three-phase induction machine assuming a balanced set, as shown in Figure 6.24. The per-phase equivalent circuit consists of the stator loop and

**FIGURE 6.24**

Steady-state per-phase equivalent circuit of an induction motor.

the rotor loop with the magnetic circuit parameters in the middle. The inductance representing the magnetization current path is in the middle of the circuit along with an equivalent core loss resistance. For the stator and rotor electrical parameters, the circuit includes the stator winding resistance and leakage reactance and the rotor winding resistance and leakage reactance. A slip-dependent equivalent resistance represents the mechanical power delivered at the shaft due to the energy conversion in the air gap-coupled electromagnetic circuit. The electrical input power supplied at the stator terminals converts to magnetic power and crosses the air gap. The air gap power P_{ag} is converted to mechanical power delivered at the shaft after overcoming the losses in the rotor circuit.

Although the per-phase equivalent circuit is not enough for designing controllers with good dynamic performance like that required in an electric or hybrid vehicle, the circuit helps develop the basic understanding of induction machines. The vast majority of applications of induction motors are for adjustable speed drives where controllers designed for good steady-state performance are adequate. The circuit does allow the analysis of a number of steady-state performance features. The parameters of the circuit model are as follows:

E_{ms} = stator-induced emf per phase

V_s = stator terminal voltage per phase

I_s = stator terminal current

R_s = stator resistance per phase

X_{ls} = stator leakage reactance

X_m = magnetizing reactance

X'_{lr} = rotor leakage reactance referred to stator

R'_r = rotor resistance referred to stator

I'_r = rotor current per phase referred to stator

Note that the voltages and currents described here in relation to the per-phase equivalent circuit are phasors and not space vectors. The power and torque relations are

$$P_{ag} = \text{Air gap power} = 3 \left| I_r' \right|^2 \frac{R_r'}{s}$$

$$\begin{aligned} P_{dev} &= \text{Developed mechanical power} = 3 \left| I_r' \right|^2 \frac{(1-s)R_r'}{s} \\ &= (1-s)P_{ag} \\ &= T_e \omega_m \end{aligned}$$

$$P_R = \text{Rotor copper loss} = 3 \left| I_r' \right|^2 R_r'$$

The electromagnetic torque is given by

$$\begin{aligned} T_e &= 3 \left| I_r' \right|^2 \frac{(1-s)R_r'}{s \omega_m} \\ &= \frac{3R_r'}{s \omega_s} \frac{V_s^2}{(R_s + R_r' s)^2 + (X_s + X_r')^2} \end{aligned} \tag{6.42}$$

The steady-state speed–torque characteristics of the machine are as shown in Figure 6.25. The torque produced by the motor depends on the slip and the stator currents among other variables. The induction motor starting torque, while depending on the design, is lower than the peak torque achievable from the motor. The motor is always operated in the linear region of the speed–torque curve to avoid the higher losses associated with the high

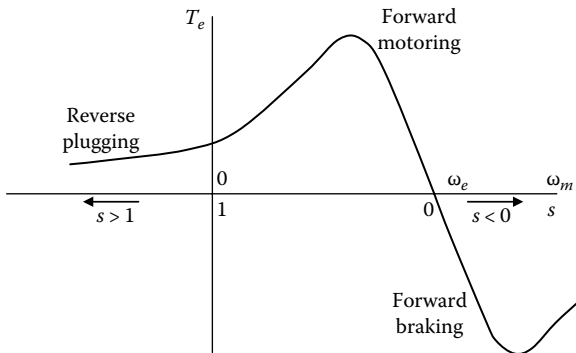


FIGURE 6.25 Steady-state torque–speed characteristics of an induction motor.

slip operation. In other words, operating the machine at small slip values improves the efficiency.

The value of the rotor circuit resistance determines the speed at which the maximum torque will occur. In general, the starting torque is low and the maximum torque occurs close to the synchronous speed when the slip is small. The motor draws a large current during line starting from a fixed AC source, which gradually subsides as the motor reaches the steady-state speed. If the load requires a high starting torque, the motor will accelerate slowly. This will make a large current flow for a longer time, thereby creating a heating problem.

The nonlinearity at speeds below the rated condition is due to the effects of the leakage reactances. At higher slip values, the frequencies of the rotor variables are large resulting in dominating impedance effects from the rotor leakage inductance. The air gap flux cannot be maintained at the rated value under this condition. Also, large values of rotor current (which flows at high slip values) cause a significant voltage drop across the stator winding leakage impedance ($R_s + j\omega L_{ls}$), which reduces the induced voltage and in turn the stator mmf flux density \hat{B}_{ms} .

6.4.2 Simplified Torque Expression

A simplified linear torque expression is sufficient to analyze the motor-load interaction, since the induction motor is invariably always operated in the linear region at maximum flux density \hat{B}_{ms} with the help of a power electronic feed circuit. The segment of interest in the torque speed characteristic curve of the induction motor is shown by the solid line in Figure 6.26. The synchronous speed is set by the applied voltage frequency and the slope of the linear region is set by the design parameters and material properties. Hence, assuming that the stator flux density is kept constant

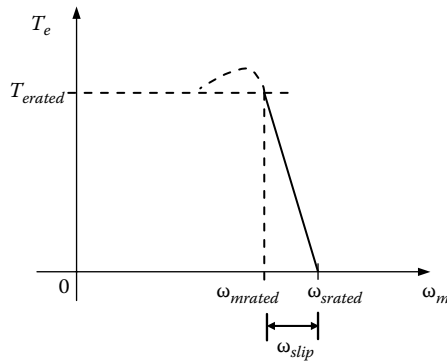


FIGURE 6.26

Torque–speed characteristics of induction motor for rated flux condition.

at its rated value, the steady-state torque can be expressed linearly as a function of slip:

$$T_e = K_{IM}\omega_{slip}$$

Here K_{IM} is a constant; the constant originates from the dependence of torque production with the geometry and the number of turns of the induction machine. The electromagnetic torque is produced by the tendency of the stator and rotor mmfs trying to align with each other. The rotor mmf is due to the rotor current. The principle of torque production essentially lies in the Lorentz force law ($F = Bil$). Therefore, the electromagnetic torque produced in an induction machine at steady state can be expressed as

$$T_e = k_M \hat{B}_{ms} \hat{I}'_r \tag{6.43}$$

where

k_M is a machine constant

\hat{B}_{ms} is the equivalent peak stator mmf flux density for the three-phase machine

\hat{I}'_r peak equivalent rotor current

Note that these are different from the single-phase equivalent circuit per-phase quantities. Mohan in [5] showed that this machine constant is $k_M = \pi r l (N_s/2)$ where r is the radius to the air gap, l is axial length of the machine, and N_s is the equivalent number of turns.

In order to find a relation between \hat{B}_{ms} and rotor current \hat{I}'_r let us denote the rotor mmf by the space vector $\vec{F}_r(t)$. The stator windings must carry currents in addition to the magnetizing current $\vec{i}_M(t)$ to support the currents induced in the rotor by transformer action to create $\vec{F}_r(t)$. These rotor currents referred to stator, or in other words, the additional stator current is represented by $\vec{i}'_r(t)$ (with magnitude- \hat{I}'_r) and is related to $\vec{F}_r(t)$ by

$$\vec{i}'_r(t) = \frac{\vec{F}_r}{N_s/2}$$

The total stator current is the sum of magnetizing current and referred rotor current

$$\vec{i}_s(t) = \vec{i}_M(t) + \vec{i}'_r(t) \tag{6.44}$$

These space vectors are shown in Figure 6.27. The rotor leakage inductance L'_{lr} has been neglected in this diagram for simplification. Although this is

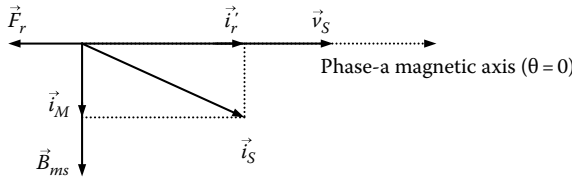


FIGURE 6.27
Space vector diagram of stator and rotor variables at $t=0$.

an ideal situation, it is a very important assumption that helps one grasp the basic concepts of torque production in induction machines. Neglecting the rotor leakage reactance is equivalent to assuming that all of the flux created by the rotor bar currents crosses the air gap and links the stator windings, and that there are no leakage fluxes in the rotor. The rated speed on induction machines is close to the synchronous speed and the machine usually operates near the rated condition with a very small slip. At small slip values, the slip speed ω_{slip} is very small and it is justified to neglect the effect of rotor leakage inductance, which is small anyway. Mohan [5] showed that under this simplifying assumption, the rotor bar currents induced by Faraday's law are proportional to the stator flux density and slip speed, the peak of which can be given by

$$\hat{I}'_r = k_r \hat{B}_{ms} \omega_{slip} \quad (6.45)$$

where k_r is a machine design constant. Substituting \hat{I}'_r from Equation 6.45 in the torque equation

$$T_e = k_m k_r \hat{B}_{ms}^2 \omega_{slip}$$

The electromagnetic torque for fixed stator flux density is

$$T_e = K_{IM} \omega_{slip} \quad (6.46)$$

where $K_{IM} = k_m k_r \hat{B}_{ms}^2$.

The simple torque expression presents a convenient method of defining the torque–speed relationship of an induction machine linearly near the rated operating point very much similar to the DC machine relationship. The expression can be used to find the steady-state operating point of an induction machine-driven electric and hybrid vehicles by finding the point of intersection of the machine torque–speed characteristics and the road load force–speed characteristics. When the motor rotates at synchronous speed, the slip speed is zero and the motor does not produce any torque. In practice,

the machine never reaches the synchronous speed even in an unloaded condition, since a small electromagnetic torque is needed to overcome the no-load losses that include the friction and windage losses. The slip speed is small up to the rated torque of the machine, and hence, it is reasonable to neglect the rotor leakage inductance, which gives the linear torque–speed relationship. The machine runs close to the synchronous speed under no-load condition with a very small slip. As the machine is loaded from the no-load condition, the slip starts to increase and the speed approaches the rated speed condition. Beyond the rated condition, the machine operates with a higher slip and the assumption of neglecting the leakage inductance starts to fall apart. This portion of the torque–speed characteristics is shown by a dotted curve in Figure 6.26.

The induction motors for electric and hybrid vehicles and other high-performance applications are supplied from a variable voltage, variable frequency AC source. Varying the frequency changes the rated flux and synchronous speed of the machine, which essentially causes the linear torque–speed curve of Figure 6.26 to move horizontally along the speed axis toward the origin.

Example 6.4

The vehicle road load characteristics on a level road is $T_{TR} = 24.7 + 0.0051\omega_{wh}^2$. The induction motor torque–speed relationship in the linear region is given by $T_e = K_{IM}(40 - \omega_m)$, including the gear ratio of the transmission system. The rated torque of 40 N m is available at a speed of 35 rad/s. Find the steady-state operating point of the vehicle.

Solution

The induction motor torque constant is

$$K_{IM} = \frac{40}{(40 - 35)} = 8 \text{ N m/rad/s}$$

The steady-state operating point is obtained by solving the vehicle road load characteristic and the motor torque–speed characteristic, which gives

$$\omega^* = 36.08 \text{ rad/s} \quad \text{and} \quad T^* = 31.34 \text{ N m}$$

6.4.3 Speed Control Methods

The speed of an induction motor can be controlled in two ways by varying the stator terminal voltage and by varying the stator frequency. Changing the terminal voltage changes the torque output of the machine, as is evident from Equation 6.42. Note that changing the applied voltage does not change the slip for maximum torque. The speed control through changing the

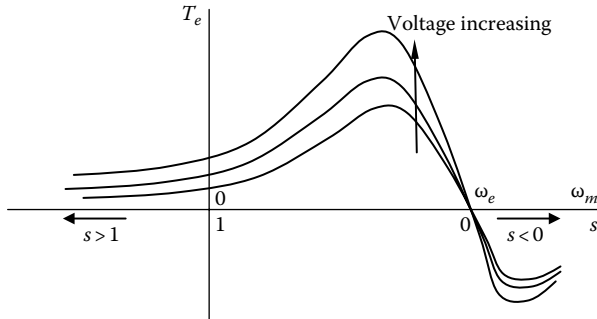


FIGURE 6.28

Torque–speed profile at different voltages with fixed supply frequency.

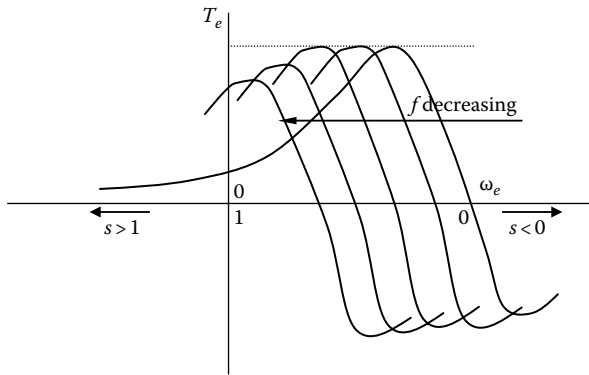


FIGURE 6.29

Torque–speed profile with variable frequency, but constant V/f ratio.

applied frequency is based on the frequency and synchronous speed relation $\omega_e = 4\pi f/p$; changing f changes ω_e . Figures 6.28 and 6.29 show the variations in torque–speed characteristics with changes in voltage and frequency, respectively. What is needed to drive the induction motor is a power electronics converter that will convert the available constant voltage into a variable voltage, variable frequency output according to the command torque and speed. The top-level block diagram of such a drive system is shown in Figure 6.30. The first generation controllers of induction motor drives used in electric vehicles employed slip control (constant V/Hz control) using a table of slip versus torque. The performance of such a drive for vehicle applications is very poor, since the concept of V/Hz control is based on steady-state equivalent circuit of the machine. The dynamic performance of the machine improves significantly using vector control. The dq -axes transformation theory for induction motors pertaining to vector control theory will be covered in Chapter 9, which discusses high-performance AC motor control methods.

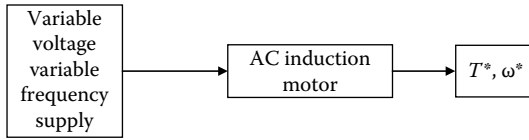


FIGURE 6.30
Induction motor drive.

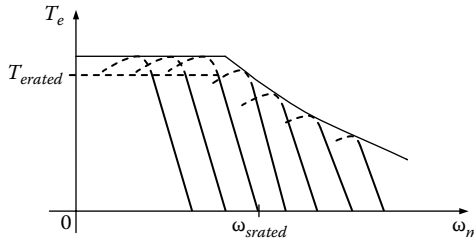


FIGURE 6.31
Torque–speed operating envelop for the induction motor.

Figure 6.31 shows the envelope of the torque–speed characteristics of an induction motor. Using a power electronics controlled drive, it is possible to achieve constant power characteristics from an induction motor at higher speeds, a feature that is so important for electric and hybrid vehicle motor drives.

6.4.4 Regenerative Braking

One of the advantages of using electric motors for vehicle propulsion is to save energy during vehicle braking through regeneration. The regenerated energy can be used to recharge the batteries of an electric or hybrid vehicle. It is important to note that it will not be possible to capture all of the energy that is available during vehicle braking, especially when sudden stops are commanded. The energy that is available during braking is the kinetic energy that was acquired by the vehicle during acceleration. The energy is typically too high to be processed by the electric motor that is used for propulsion. Processing high energy at a relatively short time would require a large motor, or, in other words, a motor with very high power ratings, which is impractical. Hence, electric and hybrid vehicles must be equipped with the mechanical brake system even though the electric motor drive is designed with regeneration capability. However, regeneration can recapture a significant portion of kinetic energy extending the vehicle range. The vehicle supervisory controller decides the amount of braking that is needed from the mechanical system based on the driver braking command, the amount of regeneration possible, and the vehicle velocity.

In the regenerative braking mode, the vehicle kinetic energy drives the shaft of the electric machine and the flow of energy is from the wheels to the energy storage system. The electric machine converts the mechanical power available from the vehicle kinetic energy and converts it to electrical energy. From the machine perspective, this is no different than operating the machine in the generator mode. Regenerative braking can increase the range of electric vehicle by a small percentage (about 10%–15%).

The induction machine works as a generator when it is operated with a negative slip, i.e., the synchronous speed is less than the motor speed ($\omega_m > \omega_s$). The negative slip makes the electromagnetic torque negative during regeneration or generating mode. In the negative slip mode of operation, the voltages and currents induced in the rotor bars are of opposite polarity compared to those in the positive slip mode. The electromagnetic torque acts on the rotor to oppose the rotor rotation, thereby decelerating the vehicle.

The motor drives for electric and hybrid vehicles are always four-quadrant drives meaning that the electric motor is controlled by the drive to deliver positive or negative torque at positive or negative speed. The transition from forward motoring to regeneration can be explained with the help of Figure 6.32 for four-quadrant induction motor drives. The linear segments of the induction motor torque–speed curves for several operating frequencies are shown in the figure. Consider the frequencies f_1 and f_2 . The curves are extended in the negative torque region to show the characteristics during regeneration. Suppose initially, the vehicle is moving forward being driven by the positive torque delivered by the induction motor, and the steady-state operating point in this condition is at point “1.” Now, the vehicle driver presses the brake pedal to slow down the vehicle. The vehicle system controller immediately changes the motor drive frequency to f_2 such that $\omega_{s2} < \omega_{m1}$. The operating point shifts to point “2” immediately, since the motor speed cannot change instantaneously due to the inertia of the system. At point

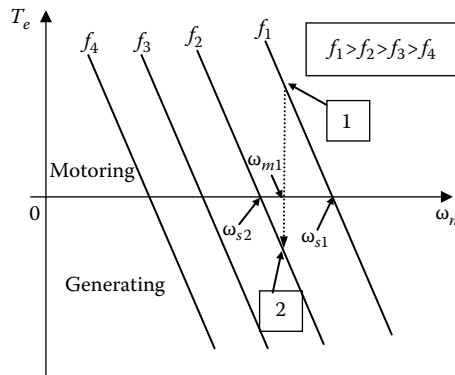


FIGURE 6.32

Transition from motoring to generating using a four-quadrant drive.

“2,” the slip and the electromagnetic torque are negative and the motor is regenerating. The vehicle will decelerate from this condition onward. As the motor speed decreases and falls below the synchronous speed, the operating frequency needs to be changed to a lower value so that generating mode operation can be maintained. The power electronics drive is responsible for establishing the shifted linear torque–speed curves with different synchronous speeds for the induction machine at different frequencies, as shown. The drive circuit does so by changing the frequency of the supply voltage. The regenerative braking mode continues as long as there is kinetic energy available and the driver wishes to slow down the vehicle. Similar to starting, the regeneration also has to be achieved in a controlled way so that the power rating of the machine is not exceeded. The amount of kinetic energy to be converted within the desired stopping time determines the power that is to be handled by the machine.

6.5 Permanent Magnet Machines

The machines that use magnets to produce air-gap magnetic flux instead of field coils as in DC commutator machines or magnetizing component of stator current as in induction machines are called *PM machines*. This configuration eliminates the rotor copper loss as well as the need for maintenance of the field exciting circuit. The PM machines can be broadly classified into two categories:

- PM synchronous machines (PMSM): These machines have uniformly rotating stator field as in induction machines. The induced waveforms are sinusoidal and hence dq transformation and vector control are possible.
- PM trapezoidal or brushless DC machines (PM BLDC): The induced voltages in these machines are trapezoidal in nature; the phase currents are rectangular or square wave in nature. These PM machines are also known as *square wave* or *electronically commutated machines*. The stator field is switched in discrete steps with square wave pulses.

There are several advantages of using PMs for the field excitation in AC machines. The PMs provide a loss-free excitation in a compact way without complications of connections to the external stationary electric circuits. This is especially true for smaller machines, since there is always an excitation penalty associated with providing the rotor field through electrical circuits. The large synchronous machines use rotor conductors to provide the excitation, since the losses in the exciter circuit, referred to as excitation penalty, are small, especially when compared to the high costs of magnets. For smaller machines, the mmf required is small and the resistive effects often become

comparable and dominating, resulting in lower efficiency. The smaller cross-sectional area of the windings for small power machines further deteriorates the resistive loss effect. Moreover, the cross-sectional area available for winding decreases as the motor size gets smaller. The loss-free excitation of PM in smaller machines with a compact arrangement is a definite plus with the only drawback being the high costs of the PMs. Nevertheless, PM machines are a strong contender for electric and hybrid vehicle drives despite the larger size of these machines. All the production passenger hybrid vehicles use PM machines for the traction motor. The factors guiding the trend are the excellent performance and the high power density achievable from the PM machine drives.

6.5.1 Permanent Magnets

The PMs are a source of mmf, much like a constant current source with relative permeability μ_r , just greater than air, i.e., $\mu_r \approx 1.05\text{--}1.07$. The PM characteristics are displayed in the second quadrant of the $B\text{--}H$ plot, as shown in Figure 6.33, conforming with the fact that these are sources of mmf. The magnets remain permanent as long as the operating point is within the linear region of its $B\text{--}H$ characteristics. However, if the flux density is reduced beyond the knee-point of the characteristics (B_d), some magnetism will be lost permanently. On removal of the demagnetizing field greater than the limit, the new characteristics will be another straight line parallel to but lower than the original. The common types of magnets used in PM machines are the ferrites, samarium cobalt (SmCo), and neodymium-iron-boron (NdFeB). The features and properties of these three magnets are discussed below [6].

6.5.1.1 Ferrites

- They have been available for decades.
- Their cost is low.

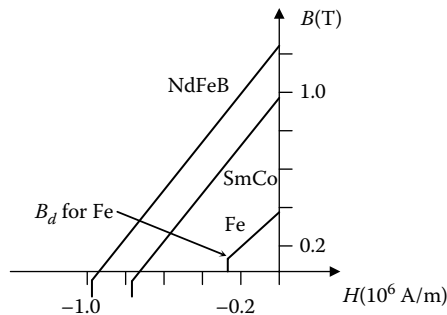


FIGURE 6.33

Characteristics of commonly used PMs.

- The residual flux density B_r at 0.3–0.4T is much lower than the desired range of gap flux density for high power density.
- B_d is higher for those ferrites for which B_r is higher.
- Ferrites have high resistivity and low core losses.
- They can be operated up to 100°C.
- An increase in temperature increases B_r and decreases B_d .

6.5.1.2 Samarium Cobalt

- This material has a higher value of B_r , 0.8–1.1 T.
- B_d is well into the third quadrant.
- B_r decreases somewhat with temperature, while B_d increases. This leads to increased sensitivity to demagnetization as temperature increases.
- The resistivity is 50 times that of Cu.
- Their cost is relatively high, reflecting the cost of rare earth element and an expensive metal.

6.5.1.3 Neodymium–Iron–Boron

- Sintered NdFeB developed in Japan in 1983 provided the major impetus to PM motors.
- B_r is in the range of 1.1–1.25 T at room temperature. This is adequate to produce a flux-density of 0.8–0.9 T across a relatively large air gap.
- B_r decreases by about 0.1% for each degree rise in temperature.
- The knee-point of flux density (B_d) increases rapidly with temperature. This imposes a limit on maximum temperature for NdFeB in the range of 100°C–140°C, depending on the detailed composition.
- The cost of these sintered NdFeB materials is still high mainly because of the manufacturing complexity of the sintering process.
- The cost may reduce in the future with increase in volume use. Fe(77%), B(8%) cost relatively little and Nd is one of the more prevalent rare earth elements.
- Bonded NdFeB magnets can be produced at a lower cost, but B_r is lower at about 0.6–0.7 T.

PM machines are designed with adequate PM considerations for magnet protection. Demagnetization may occur if flux density is reduced below the knee-point of flux density B_d . Most PM motors are designed to withstand considerable overload currents (2–4 times the rated) without danger to the magnets.

6.5.2 PM Synchronous Motors

The PMSM is a synchronous motor with sinusoidal mmf, voltage, and current waveforms where the field mmf is provided by PMs. The use of rare earth magnet materials increases the flux density in the air gap and accordingly increases the motor power density and torque-to-inertia ratio. In high-performance motion control systems that require servo-type operation, the PMSM can provide fast response, high power density, and high efficiency. In certain applications like robotics and aerospace actuators, it is preferable to have the weight as low as possible for a given output power. The PMSM, similar to the induction and DC machines, is fed from a power electronic inverter for its operation. The smooth torque output is maintained in these machines by shaping the motor currents, which requires a high-resolution position sensor and current sensors. The control algorithm is implemented in a digital processor using feedback from the sensors. A flux weakening mode that enables a higher speed operation in the constant power region is possible in PMSM by applying a stator flux in opposition to the rotor magnet flux. The motor high speed limit depends on the motor parameters, its current rating, the back-emf waveform, and the maximum output voltage of the inverter.

PMSM and induction motors have good performance in terms of torque response and have rugged motor structures, although broken magnet chips in PM machines is a concern. The slip speed calculation makes the induction motor control more complicated than that of the PMSM. Without a rotor cage, the PMSM has a lower inertia that helps the electrical response time, although the induction motor electrical response characteristics will be the fastest because of the smaller time constant. The electrical time constant of magnetic circuits is determined by the L/R ratio. The load current transient in induction machines is limited only by the small leakage inductance, where the time constant inductance in PM machines is the much higher self-inductance. With a higher power density, the PMSM is smaller in size compared to an induction motor with the same power rating. The PMSM is more efficient and easier to cool due to the absence of rotor copper loss compared to the induction machines. The induction motor has lower cost and zero cogging torque because of the absence of PMs. Also, it is less sensitive to higher operating temperatures. The induction motor can sustain a higher peak stator current at several times the rated current without the danger of demagnetizing the magnets. Both the induction motors and the PMSM suffer from limited field weakening speed range.

The PMs in PMSMs are not only expensive, but also sensitive to temperature and load conditions, which constitute the major drawbacks of PM machines. Most of the PMSMs are found in small-to-medium power applications, although there are some high-power applications for which PMSMs are being used.

PMSM has a stator with a set of three-phase sinusoidally distributed copper windings similar to the windings described in Section 6.2 on AC machines. A balanced set of applied three-phase voltages forces a balanced set of sinusoidal currents in the three-phase stator windings, which in turn establishes the constant amplitude rotating mmf in the air gap. The stator currents are regulated using rotor position feedback so that the applied current frequency is always in synchronism with the rotor. The PMs in the rotor are appropriately shaped and their magnetization directions are controlled such that the rotor flux linkage created is sinusoidal. The electromagnetic torque is produced at the shaft by the interaction of these two stator and rotor magnetic fields.

The PMSMs are classified according to the position and shape of the PMs in the rotors. The three common arrangements of PMs in the rotors are surface mounted, inset, and interior or buried, which are shown in Figure 6.34. The difference between surface-mounted and inset magnets is that the magnets in the latter are inside the rotor surface, but still exposed to the air gap. The surface-mounted and inset rotor PMSMs are often collectively called

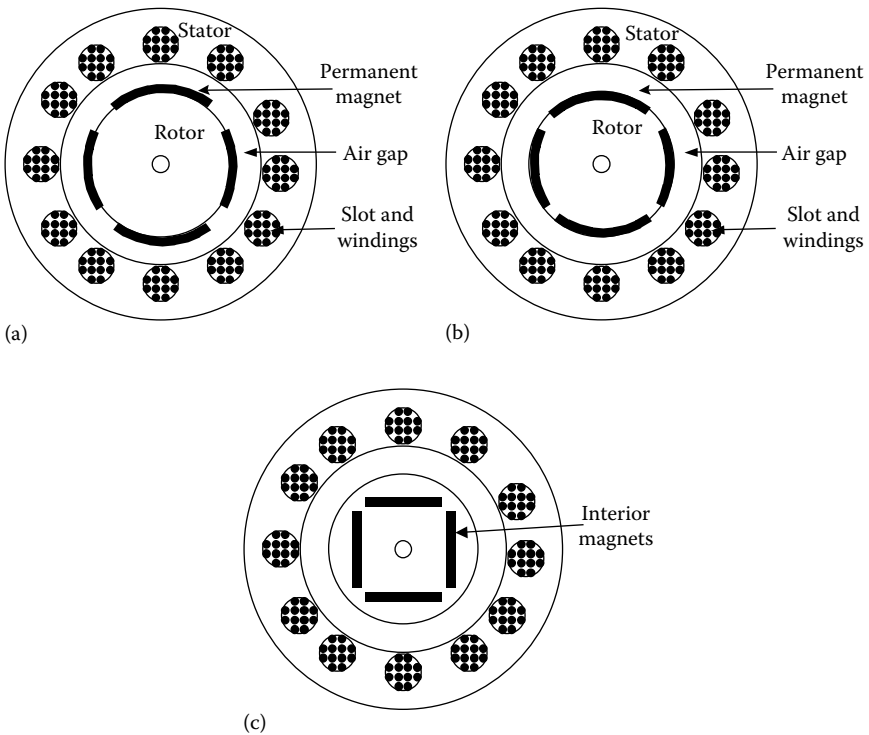


FIGURE 6.34 PM machines: (a) surface-mounted, (b) inset, and (c) interior.

the *surface-mount PMSMs*. In the surface-mounted PMSM, the magnets are epoxy-glued or wedge-fixed to the cylindrical rotor. Nonmagnetic stainless steel or carbon fiber sleeves are also used to contain the magnets. The manufacturing of this kind of rotor is simple, although the mechanical strength of the rotor is only as good as that of the epoxy glue. In the inset PMSM, the magnets are put into the rotor surface slots, which make the magnet more secured. The other type of PMSM is the interior PMSM, so named because the magnets are buried inside the rotor. The manufacturing process is complicated and expensive for the interior PMSM.

6.5.3 PMSM Models

The modeling and control of PMSMs can be done using either scalar or vector methods. In the scalar control method, the per-phase equivalent circuit is derived from the three-phase abc system. With vector control method, the three-phase variables are transformed into an equivalent two-phase system, and both amplitude and angle of the current are controlled. The three-phase abc reference directions, and the fictitious two-phase $\alpha\beta$ and dq reference directions are shown in Figure 6.35. For the dq systems, d stands for direct axis and q stands for quadrature axis. The abc and $\alpha\beta$ reference frames are fixed in the stator with the direction of α -axis chosen in the same direction as the a -axis. The β -axis lags the α -axis by 90° space angle. The abc to $\alpha\beta$ transformation essentially transforms the three-phase stationary variables to a set of two-phase stationary variables. In the dq reference, the d -axis is aligned with the magnet flux direction, while the q -axis lags the d -axis by 90° space angle.

The direct and quadrature-axes inductances of a PMSM play an important role in the control of the machine. For the surface-mounted PMSM, the two inductances are approximately equal, since the permeability of the flux path between the stator and the rotor is equal all around the stator circumference. The uniformity in the magnetic path despite the presence of magnets is because the permeability of magnets is approximately equal to that of the air. The space needed to mount the magnets increases the radial distance of the effective air gap, making the self-inductance relatively smaller in PMSMs.

The direct and quadrature-axes reluctances are unequal in inset PMSMs, since space is occupied by magnet in the direct axis and by iron in the quadrature axis. The q -axis inductance L_q is larger than the d -axis inductance L_d , since the d -axis flux path has larger effective air gap, and hence, higher reluctance, although the length of the air gap between the stator and rotor is the same. These inductances

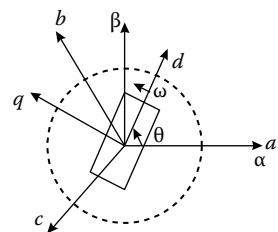


FIGURE 6.35

The stationary and synchronous frames in PMSM.

consist of the magnetizing inductances and the leakage inductances, and are given as

$$L_q = L_{ls} + L_{mq} \quad (6.47)$$

and

$$L_d = L_{ls} + L_{md} \quad (6.48)$$

The interior PMSM has its magnets buried inside the rotor. The q -axis inductance L_q in the interior PMSM can be much larger than the d -axis inductance L_d . The larger difference in the d and q -axes inductances make the interior PM more suitable for flux weakening operation, delivering a wider constant power region compared to the surface-mount or inset PMSMs. The extended constant power range capability is extremely important for an electric and hybrid vehicle application to eliminate the use of multiple gear ratios. Because of the unequal reluctance paths in the direct and quadrature axes, a reluctance torque exists in buried and inset PMSMs.

The per-phase equivalent circuit model and the scalar control of PMSM are discussed in the following section. The vector control methods are presented in Chapter 9 after the theory of reference frame transformation is addressed in further detail.

6.5.3.1 Voltage Equations

The stator circuit of a PMSM is similar to that of an induction motor or a wound rotor synchronous motor with the applied voltage being balanced by the stator winding resistance drop and the induced voltage in the winding. The PMSM model is derived below, assuming that the stator windings in the three phases are symmetrical and sinusoidally distributed. The eddy current and hysteresis losses are neglected in the model and the damper or cage windings are also not considered. The damper windings are not necessary in PMSMs, since PM is a poor electrical conductor and eddy currents are negligible. Large armature currents can be tolerated in these machines without significant demagnetization. The stator phase voltage equation in the stationary abc reference frame is

$$\vec{v}_{abc} = \bar{R}_s \vec{i}_{abc} + \frac{d}{dt} \vec{\lambda}_{abc} \quad (6.49)$$

where

$$\begin{aligned} (\vec{f}_{abc})^T &= [f_{as} \ f_{bs} \ f_{cs}] \quad (f \text{ represents } v, i \text{ or } \lambda) \\ \bar{R}_s &= \text{diag}[R_s \ R_s \ R_s] \end{aligned}$$

The flux linkages are

$$\vec{\lambda}_{abc_s} = \bar{L}_s \vec{i}_{abc_s} + \vec{\lambda}_f \tag{6.50}$$

where \bar{L}_s is the inductance matrix which is the same for all synchronous machines. $\vec{\lambda}_f$ is due to the PM and is given by

$$\vec{\lambda}_f = \lambda_f \begin{bmatrix} \sin \theta_r \\ \sin \left(\theta_r - \frac{2\pi}{3} \right) \\ \sin \left(\theta_r + \frac{2\pi}{3} \right) \end{bmatrix} \tag{6.51}$$

where λ_f is the amplitude of the flux linkage established by the PM, as viewed from the stator phase windings.

6.5.3.2 Per-Phase Equivalent Circuit

A simplified per-phase equivalent circuit can be derived for the special case of surface-mount PM machines and also when the magnets are only slightly inset in the rotor. The air-gap inductances along the d and q -axes are equal in this case, and can be denoted by

$$L_m = L_{md} = L_{mq} \tag{6.52}$$

In the per-phase equivalent circuit, the fundamental frequency components of voltages and currents of the inverter-driven machine are regarded as balanced three-phase sets for steady-state and slowly varying transient conditions. The PM machine can then be represented by the per-phase equivalent circuit shown in Figure 6.36a. The current source I_f represents the root mean square (rms) value of the equivalent magnet current i_{fd} that would create

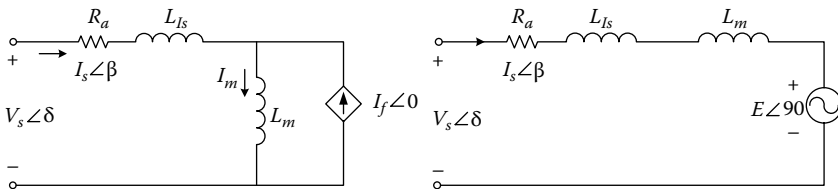


FIGURE 6.36 PM synchronous motor equivalent circuits showing (a) equivalent magnet current and (b) induced voltage.

the PM flux λ_f . The PM flux, in terms of the equivalent current, is given by $\lambda_f = L_m i_{fd}$. Assuming sinusoidal distribution of stator windings, only the fundamental component of magnet flux density link with the stator windings. The magnetizing inductance L_m for PM machines is much smaller than that of induction machines because of much larger effective air gap.

From the stator terminals, the effect of the PM flux is seen as a back-emf voltage given by $E = j\omega L_m I_m$. This back-emf or induced voltage is shown in the alternative representation of the per-phase equivalent circuit in Figure 6.36b. The stator per-phase rms current is denoted by I_s , which leads the reference axis (d -axis in this case) by an angle γ . The PM machine provides continuous torque only when rotor speed is synchronized with the stator frequency. For the per-phase model, the torque is given by

$$T_e = 3 \times \frac{P}{2} L_m I_f I_s \sin \gamma \tag{6.53}$$

The torque is maximum when $\gamma=90^\circ$. The vector diagram for this maximum torque condition is shown in Figure 6.37a. The input power factor in this condition is lagging. Operation in this mode is practical up to the limit of the inverter supply voltage. At higher speeds, the appropriate operating condition is that for unity power factor, which maximizes the inverter volt-amp rating utilization. The vector diagram for this condition is given in Figure 6.37b. The motor can also be operated with a leading power factor by increasing the voltage angle δ , as shown in Figure 6.37c. This condition is desired for some large synchronous drives that allows the use of a load-commutated inverter.

The per-phase equivalent circuit is useful for developing an understanding of the basic operation of synchronous machines. The per-phase equivalent circuit and the corresponding torque equations signify that torque is maximized at $\gamma=90^\circ$ where the stator current is aligned in quadrature with the magnet field axis. The magnet field axis is along the direct or d -axis

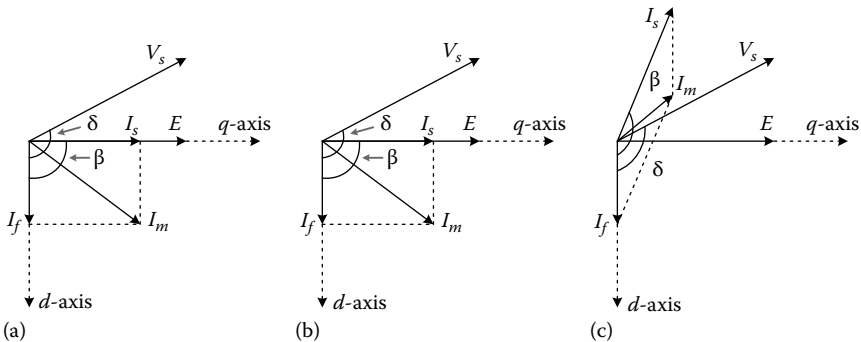


FIGURE 6.37 Vector diagrams with three power factors for the per-phase equivalent circuit: (a) lagging, (b) unity, and (c) leading.

and the stator current is along the quadrature or q -axis in this condition. Maintaining such orthogonality consistently and continuously through both magnitude and angle controls of the stator current form the basis of vector controls, which is used for traction motor drives. Motor operation for $\gamma > 90^\circ$ is known as field weakening operation, which is also used in vector control methods. It can also be noted that for regeneration, the rotor angle γ is made negative through current control.

6.5.4 PM Brushless DC Motors

The PM AC machines with trapezoidal back-emf waveforms are the PM brushless DC (PM BLDC) machines. The trapezoidal-shaped back-emf waveforms in these machines are due to the concentrated windings of the machine used instead of the sinusoidally distributed windings used in the PMSMs. The PM BLDC motors are used in a wide variety of applications ranging from computer drives to sophisticated medical equipment. The reason behind the popularity of these machines is the simplicity of control. Only six discrete rotor positions per electrical revolution are needed in a three-phase machine to synchronize the phase currents with the phase back-emfs for effective torque production. A set of three Hall sensors mounted on the stator facing a magnet wheel fixed to the rotor and placed 120° apart can easily give this position information. This eliminates the need for a high-resolution encoder or position sensor required in PMSMs, but the penalty paid for position sensor simplification is in the performance. Vector control is not possible in PM BLDC machines because of the trapezoidal shape of the back-emfs.

The three-phase back-emf waveforms and the ideal phase currents of a PM BLDC motor are shown in Figure 6.38. The back-emf waveforms are fixed with respect to the rotor position. Square wave phase currents are supplied such that they are synchronized with the peak back-emf segment of the respective phase. The controller achieves this objective using rotor position feedback information. The motor basically operates like a DC motor with its electronic controller; hence, the motor is called the brushless DC motor.

6.5.4.1 PM BLDC Machine Modeling

The PM in the rotor can be regarded as a constant current source, giving rise to the back-emfs in the stator windings. The three stator windings for the three phases are assumed to be identical with 120° (electrical) phase displacement among them. Therefore, the stator winding resistances and the self-inductance of each of the three phases can be assumed to be identical. Let

$$\begin{aligned} R_s &= \text{stator phase winding resistance} \\ L_{aa} = L_{bb} = L_{cc} = L &= \text{stator phase self-inductance} \\ L_{ab} = L_{ac} = L_{bc} = M &= \text{stator mutual inductance} \end{aligned}$$

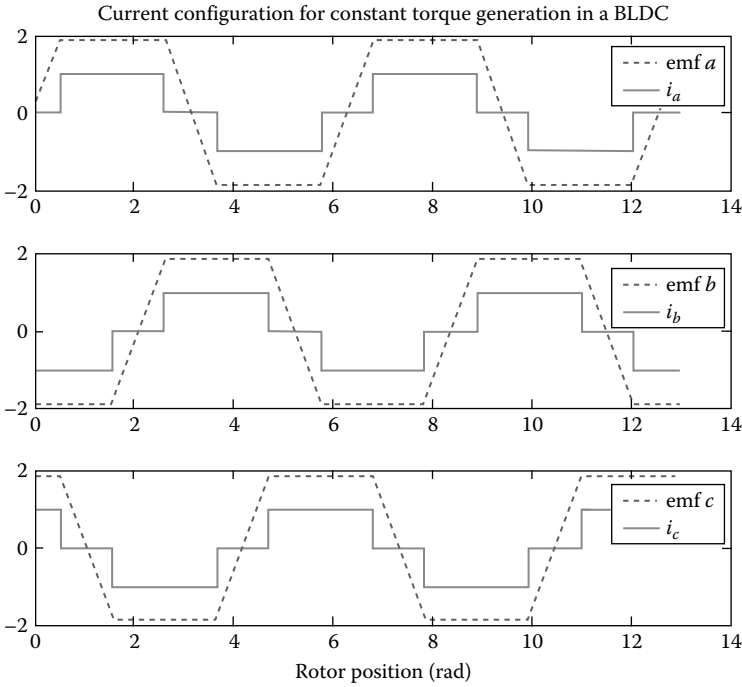


FIGURE 6.38

Back-emf and ideal phase currents in the three phases of a PM brushless DC motor.

The voltage balance equations for the three phases are

$$\begin{bmatrix} v_a \\ v_b \\ v_c \end{bmatrix} = R \cdot \begin{bmatrix} i_a \\ i_b \\ i_c \end{bmatrix} + \begin{bmatrix} L & M & M \\ M & L & M \\ M & M & L \end{bmatrix} \cdot p \cdot \begin{bmatrix} i_a \\ i_b \\ i_c \end{bmatrix} + \begin{bmatrix} e_a \\ e_b \\ e_c \end{bmatrix} \tag{6.54}$$

where

p is the operator d/dt

$e_a, e_b,$ and e_c are the back-emfs in the three phases, respectively

The back-emf is related to the phase flux linkage as

$$e = \frac{d\lambda}{dt} = \frac{d\lambda}{d\theta} \cdot \frac{d\theta}{dt}$$

However, $d\theta/dt = \omega_r$, which is the rotor speed. Then,

$$e = \omega_r \cdot \frac{d\lambda}{d\theta} \tag{6.55}$$

Similar to the back-emfs, the currents are also shifted by 120° , and they satisfy the condition $i_a + i_b + i_c = 0$. Therefore, we have $M \cdot i_b + M \cdot i_c = -M \cdot i_a$; similar expressions exist for the two other phases. Equation 6.9 can then be simplified as

$$\begin{bmatrix} v_a \\ v_b \\ v_c \end{bmatrix} = R \cdot \begin{bmatrix} i_a \\ i_b \\ i_c \end{bmatrix} + \begin{bmatrix} L-M & 0 & 0 \\ 0 & L-M & 0 \\ 0 & 0 & L-M \end{bmatrix} \cdot p \cdot \begin{bmatrix} i_a \\ i_b \\ i_c \end{bmatrix} + \begin{bmatrix} e_a \\ e_b \\ e_c \end{bmatrix}$$

The rate of change of currents with the applied voltages can be expressed as

$$p \cdot \begin{bmatrix} i_a \\ i_b \\ i_c \end{bmatrix} = \frac{1}{L-M} \cdot \begin{bmatrix} v_a \\ v_b \\ v_c \end{bmatrix} - R \cdot \begin{bmatrix} i_a \\ i_b \\ i_c \end{bmatrix} - \begin{bmatrix} e_a \\ e_b \\ e_c \end{bmatrix} \quad (6.56)$$

The electrical power transferred to the rotor is equal to the mechanical power $T_e \omega_r$, available at the shaft. Using this equality, the electromagnetic torque for the PM BLDC motor is

$$T_e = \frac{e_a \cdot i_a + e_b \cdot i_b + e_c \cdot i_c}{\omega_r} \quad (6.57)$$

For the control strategy described previously where only two-phase currents are active at a time, the torque expression for equal currents in two phases simplifies to

$$T_e = \frac{2 \cdot e_{max} \cdot I}{\omega_r} \quad (6.58)$$

Since the currents are controlled to synchronize with the maximum back-emf only, e_{max} has been used in Equation 6.58 instead of e as a function of time or rotor position. Assuming magnetic linearity, Equation 6.55 can be written as

$$e = K \cdot \omega_r \cdot \frac{dL}{d\theta}$$

Hence, the maximum back-emf is

$$e_{max} = K \cdot \left[\frac{dL}{d\theta} \right]_{max} \cdot \omega_r \quad \text{or} \quad e_{max} = K' \cdot \omega_r \quad (6.59)$$

Equations 6.58 and 6.59 are very similar to $E = K \cdot \phi \cdot \omega$ and $T = K \cdot \phi \cdot I$ equations associated with regular DC machines. Therefore, with the described control strategy, a PM BLDC machine can be considered to behave like a DC machine.

6.6 Switched Reluctance Machines

The switched reluctance motor (SRM) is a doubly salient, singly excited reluctance machine with independent phase windings on the stator. The stator and the rotor are made of magnetic steel laminations, with the latter having no windings or magnets. The SRMs can be of various stator-rotor pole combinations related to different phase configurations. The cross-sectional diagrams of a four-phase, 8-6 SRM and a three-phase, 12-8 SRM are shown in Figure 6.39. The three-phase, 12-8 machine is a two-repetition version of the basic 6-4 structure within the single stator geometry. The two-repetition machine can alternately be labeled as a four-poles/phase machine, compared to the 6-4 structure that can be called a two-poles/phase machine. The stator windings on diametrically opposite poles are connected either in series or in parallel to form one phase of the motor. When a stator phase is energized, the most adjacent rotor pole-pair is attracted toward the energized stator in order to minimize the reluctance of the magnetic path. Therefore, it is possible to develop constant torque in either direction of rotation by energizing consecutive phases in succession.

The aligned position of a phase is defined to be the orientation when the stator and rotor poles of the phase are perfectly aligned with each other,

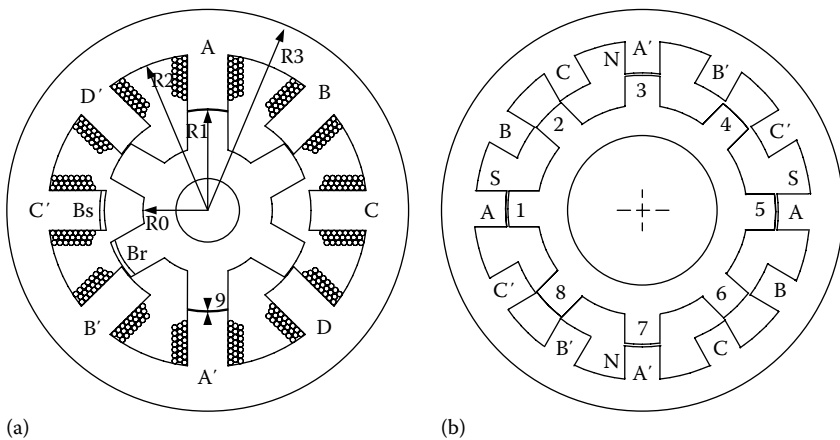


FIGURE 6.39 Cross-sections of three-phase SR machines: (a) four-phase 8/6 structure; (b) 12/8, two-repetition (two-channel) structure.

attaining the minimum reluctance position. The unsaturated phase inductance is maximum (L_{iu}) in this position. The phase inductance decreases gradually as the rotor poles move away from the aligned position in either direction. When the rotor poles are symmetrically misaligned with the stator poles of a phase, the position is said to be the unaligned position. The phase has the minimum inductance (L_{il}) in this position. Although, the concept of inductance is not valid for a highly saturating machine like SRM, the unsaturated aligned and unaligned inductances are two key reference positions for the controller.

Several other combinations of the number of stator and rotor poles exist, such as 10–4, 12–8, etc. A 4–2 or a 2–2 configuration is also possible, but these have the disadvantage that if the stator and rotor poles are aligned exactly, then it would be impossible to develop a starting torque. The configurations with higher number of stator/rotor pole combinations have less torque ripple and do not have the problem of starting torque.

6.6.1 Advantages and Disadvantages

The switched reluctance machines or motors possess few unique features that make them strong competitors to existing AC and DC motors in various adjustable speed drive and servo applications. The machine construction is simpler due to the absence of rotor winding and PMs. The bulk of the losses in the machine occur in the stator, which is relatively easier to cool. The starting torque of the SRM can be very high without the problem of excessive inrush current due to its higher self-inductance. Another great advantage of SRMs is that the maximum permissible rotor temperature is higher. The SRMs can be designed with a wide constant power region, which is a feature particularly attractive for traction applications. The SRM also has some unique fault tolerance features that do not exist in other AC machines. Since each phase winding is connected in series with converter switching elements, there is no possibility of shoot-through faults between the DC buses in the SRM drive converter. The independent stator phases enable drive operation in spite of loss of one or more phases, and the drive can be brought to a safe shutdown instead of a sudden stop.

The SRM also comes with a few disadvantages among which torque ripple and acoustic noise are the most critical. The double saliency construction and the discrete nature of torque production by the independent phases lead to higher torque ripple compared to other machines. The higher torque ripple also causes the ripple current in the DC supply to be quite large, necessitating a large filter capacitor. The doubly salient structure of the SRM also causes higher acoustic noise compared to other machines. The main source of acoustic noise is the radial magnetic force-induced resonance with the circumferential mode-shapes of the stator. The drawbacks have been addressed through research, and solutions for torque ripple minimization and acoustics noise reduction do exist. Besides, all applications are not highly sensitive to torque ripple and acoustic noise.

The absence of PMs imposes the excitation burden on the stator windings and converter, which increases the converter kVA requirement. Compared to PM brushless machines, the per-unit stator copper losses will be higher, reducing the efficiency and torque per ampere. However, the maximum speed at constant power is not limited by the fixed magnet flux as in the PM machine, and hence, an extended constant power region of operation is possible in SRMs. The control can be simpler than the field-oriented control of induction machines, although for torque ripple minimization significant computations may be required for an SRM drive.

6.6.2 SRM Design/Basics

The fundamental design rules governing the choice of phase numbers, pole numbers, and pole arcs are discussed in detail by Lawrenson et al. [7] and also by Miller [8]. From a designer's point of view, the objectives are to minimize the core losses, to have good starting capability, to minimize the unwanted effects due to varying flux distributions and saturation, and to eliminate mutual coupling. The choice of the number of phases and poles is open, but a number of factors need to be evaluated prior to making a selection. A comprehensive design methodology of SRM appears in [9].

The fundamental switching frequency is given by

$$f = \frac{n}{60} N_r \text{ Hz} \quad (6.60)$$

where

n is the motor speed in rpm

N_r is the number of rotor poles

The "step angle" or "stroke" of an SRM is given by

$$\text{Step Angle } \varepsilon = \frac{2\pi\delta}{N_{ph} \cdot N_{rep} \cdot N_r} \quad (6.61)$$

The step angle is an important design parameter related to the frequency of control per rotor revolution. N_{rep} represents the multiplicity of the basic SRM configuration, which can also be stated as the number of pole pairs per phase. N_{ph} is the number of phases. N_{ph} and N_{rep} together set the number of stator poles.

The regular choice of the number of rotor poles in an SRM is

$$N_r = N_s \pm k_m \quad (6.62)$$

where

k_m is an integer such that $k \bmod q \neq 0$

N_s is the number of stator poles

Some combinations of parameters allowed by Equation 6.62 are not feasible, since sufficient space must exist between the poles for the windings. The most common choice of Equation 6.62 for the selection of stator and rotor pole numbers is $k_m = 2$ with the negative sign.

The SRM is always driven into saturation to maximize the utilization of the magnetic circuit, and hence, the flux-linkage λ_{ph} is a nonlinear function of stator current and rotor position given by

$$\lambda_{ph} = \lambda_{ph}(i_{ph}, \theta)$$

The electromagnetic profile of an SRM is defined by the $\lambda - i - \theta$ characteristics shown in Figure 6.40. The highest possible saliency ratio (the ratio between the maximum and minimum unsaturated inductance levels) is desired to achieve the highest possible torque per ampere, but as the rotor and stator pole arcs are decreased, the torque ripple tends to increase. The torque ripple adversely affects the dynamic performance of an SRM drive. For many applications, it is desirable to minimize the torque ripple, which can be partially achieved through appropriate design. The torque dip observed in the $T - i - \theta$ characteristics of an SRM (see Figure 6.41) is an indirect measure of the torque ripple expected in the drive system. The torque dip is the difference between

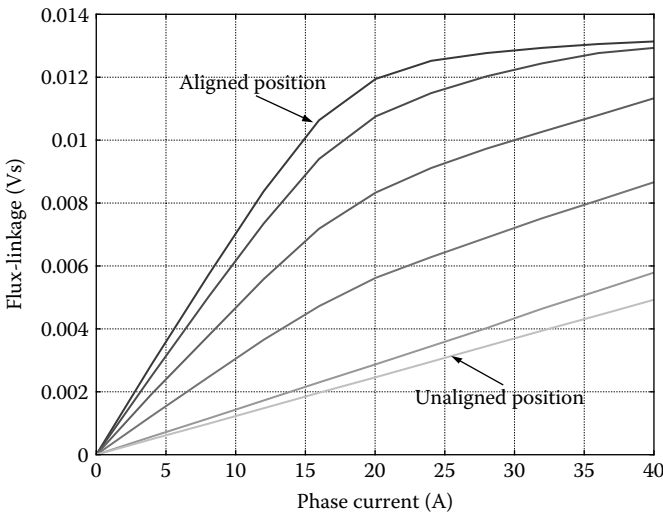


FIGURE 6.40

Flux-angle-current characteristics of a four-phase SRM.

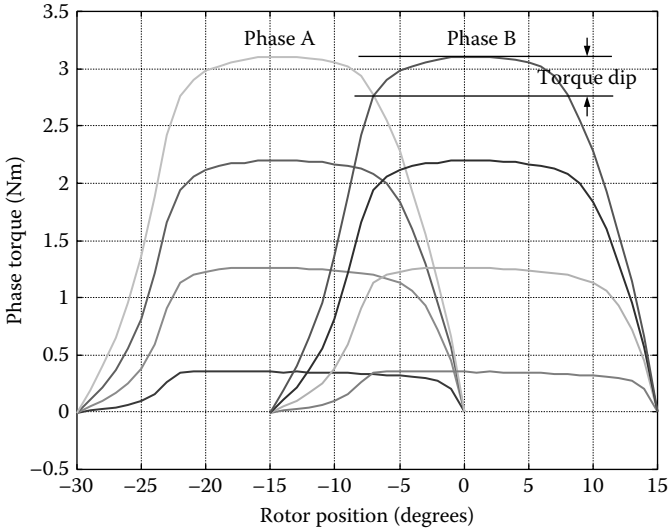


FIGURE 6.41 Torque–angle–current characteristics of a four-phase SRM for four constant current levels.

the peak torque of a phase and the torque at an angle where two overlapping phases produce equal torque at equal levels of current. The smaller the torque dip, the less will be the torque ripple. The $T-i-\theta$ characteristics of the SRM depend on the stator–rotor pole overlap angle, pole geometry, material properties, number of poles, and number of phases. A design tradeoff needs to be considered to achieve the desired goals. The $T-i-\theta$ characteristics must be studied through finite element analysis during the design stage to evaluate both the peak torque and torque dip values.

6.6.3 Principle of Operation

6.6.3.1 Voltage-Balance Equation

The general equation governing the flow of stator current in one phase of an SRM can be written as

$$V_{ph} = i_{ph}R_s + \frac{d\lambda_{ph}}{dt} \tag{6.63}$$

where

- V_{ph} is the DC bus voltage
- i_{ph} is the instantaneous phase current
- R_s is the winding resistance
- λ_{ph} is the flux linking the coil

The stator phase voltage can be expressed as

$$V_{ph} = i_{ph}R_s + \frac{\partial \lambda_{ph}}{\partial i_{ph}} \frac{di_{ph}}{dt} + \frac{\partial \lambda_{ph}}{\partial \theta} \frac{d\theta}{dt} = i_{ph}R_s + L_{inc} \frac{di_{ph}}{dt} + k_v \omega \quad (6.64)$$

where

L_{inc} is the incremental inductance

k_v is the current-dependent back-emf coefficient

$\omega = d\theta/dt$ is the rotor angular speed

Assuming magnetic linearity (where $\lambda_{ph} = L_{ph}(\theta)i_{ph}$), the voltage expression can be simplified as

$$V_{ph} = i_{ph}R_s + L_{ph}(\theta) \frac{di_{ph}}{dt} + i_{ph} \frac{dL_{ph}(\theta)}{dt} \omega \quad (6.65)$$

The last term in Equation 6.65 is the “back-emf” or “motional-emf” and has the same effect on SRM as the back-emf has on DC motors or PM BLDC motors. However, the back-emf in SRM is generated in a different way from the DC machines or PM BLDC motors where it is caused by a rotating magnetic field. In an SRM, there is no rotor field and back-emf depends on the instantaneous rate of change of phase flux linkage and the phase current.

In the linear case, which is always valid for lower levels of phase current, the per-phase equivalent circuit of an SRM consists of a resistance, an inductance, and a back-emf component. The back-emf vanishes when there is no phase current or the phase inductance is constant relative to the rotor position. Depending on the magnitude of current and rotor angular position, the equivalent circuit changes its structure from being primarily an R - L circuit to primarily a back-emf-dependent circuit.

6.6.3.2 Energy Conversion

The energy conversion process in an SRM can be evaluated using the power balance relationship. Multiplying Equation 6.65 by i_{ph} on both sides, the instantaneous input power can be expressed as

$$\begin{aligned} P_{in} = V_{ph}i_{ph} &= i_{ph}^2 R_s + \left(L_{ph}i_{ph} \frac{di_{ph}}{dt} + \frac{1}{2} i_{ph}^2 \frac{dL_{ph}}{d\theta} \omega \right) + \frac{1}{2} i_{ph}^2 \frac{dL_{ph}}{d\theta} \omega \\ &= i_{ph}^2 R + \frac{d}{dt} \left(\frac{1}{2} L_{ph} i_{ph}^2 \right) + \frac{1}{2} i_{ph}^2 \frac{dL_{ph}}{d\theta} \omega \end{aligned} \quad (6.66)$$

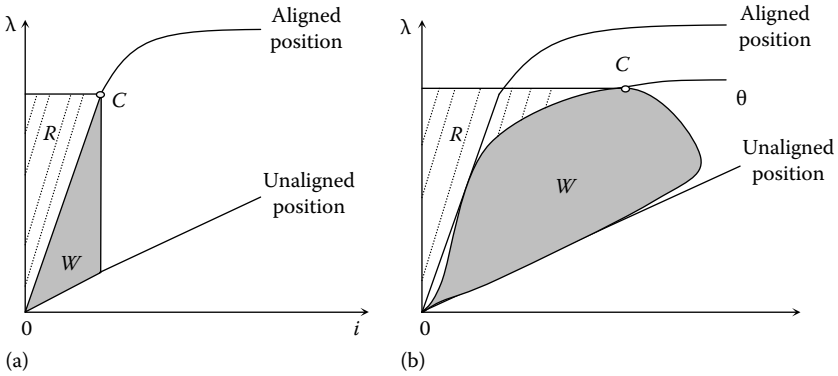


FIGURE 6.42 Energy partitioning during one complete working stroke. (a) Linear assumption. (b) Practical case. W =energy converted into mechanical work. R =energy returned to the DC supply.

The first term represents the stator winding loss, the second term denotes the rate of change of magnetic stored energy, while the third term is the mechanical output power. The rate of change of magnetic stored energy always exceeds the electromechanical energy conversion term. The most effective use of the energy supplied is when the current is maintained constant during the positive $dL_{ph}/d\theta$ slope. The magnetic stored energy is not necessarily lost, but can be retrieved by the electrical source if an appropriate converter topology is used. In the case of a linear SRM, the energy conversion effectiveness can be at most 50%, as shown in the energy division diagram of Figure 6.42a. The drawback of lower effectiveness is the increase in converter volt-amp rating for a given power conversion of the SRM. The division of input energy increases in favor of energy conversion if the motor operates under magnetic saturation. The energy division under saturation is shown in Figure 6.42b, where the effectiveness is clearly much more than 50%. This is the primary reason for operating the SRM always under saturation. The term energy ratio instead of efficiency is often used for SRM, because of the unique situation of the energy conversion process. The energy ratio is defined as

$$ER = \frac{W}{W + R} \tag{6.67}$$

where

W is the energy converted into mechanical work

R is the energy returned to the source using a regenerative converter

The term *energy ratio* is analogous to the term *power factor* used for AC machines.

6.6.3.3 Torque Production

The torque is produced in the SRM by the tendency of the rotor to attain the minimum reluctance position when a stator phase is excited. The general expression for instantaneous torque for such a device that operates under the reluctance principle is

$$T_{ph}(\theta, i_{ph}) = \left. \frac{\partial W'(\theta, i_{ph})}{\partial \theta} \right|_{i=\text{constant}} \quad (6.68)$$

where W' is the coenergy defined as

$$W' = \int_0^i \lambda_{ph}(\theta, i_{ph}) di$$

Obviously, the instantaneous torque is not constant. The total instantaneous torque of the machine is given by the sum of the individual phase torques

$$T_{inst}(\theta, i) = \sum_{\text{phases}} T_{ph}(\theta, i_{ph}) \quad (6.69)$$

The SRM electromechanical properties are defined by the static $T-i-\theta$ characteristics of a phase shown in Figure 6.39. The average torque is a more important parameter from the user's perspective and can be derived mathematically by integrating Equation 6.69.

$$T_{avg} = \frac{1}{T} \int_0^T T_{inst} dt \quad (6.70)$$

The average torque is also an important parameter during the design process.

When magnetic saturation can be neglected, the instantaneous torque expression becomes

$$T_{ph}(\theta, i) = \frac{1}{2} i_{ph}^2 \frac{dL_{ph}(\theta)}{d\theta} \quad (6.71)$$

The linear torque expression also follows from the energy conversion term (last term) in Equation 6.66. The phase current needs to be synchronized with the rotor position for effective torque production. For positive or motoring torque, the phase current is switched such that rotor is moving from the unaligned position toward the aligned position. The linear SRM model is very insightful in understanding these situations. Equation 6.71 clearly shows that for motoring torque, the phase current must coincide with the

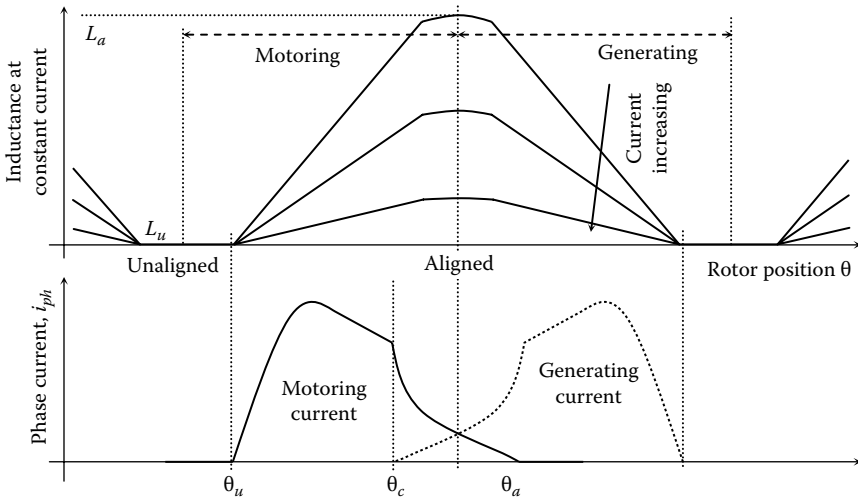


FIGURE 6.43 Phase currents for motoring and generating modes with respect to rotor position and idealized inductance profiles.

rising inductance region. On the other hand, the phase current must coincide with the decreasing inductance region for braking or generating torque. The phase currents for motoring and generating modes of operation are shown in Figure 6.43 with respect to the phase inductance profiles. The torque expression also shows that the direction of current is immaterial in torque production. The optimum performance of the drive system depends on the appropriate positioning of phase currents relative to the rotor angular position. Therefore, a rotor position transducer is essential to provide the position feedback signal to the controller.

6.6.3.4 Torque–Speed Characteristics

The torque–speed plane of an SRM drive can be divided into three regions, as shown in Figure 6.44. The constant torque region is the region below the base speed ω_b , which is defined as the highest speed when maximum rated current can be applied to the motor at rated voltage with fixed firing angles. In other words, ω_b is the lowest possible speed for the motor to operate at its rated power.

Region 1: In the low-speed region of operation, the current rises almost instantaneously after turn-on, since the back-emf is small. The current can be set at any desired level by means of regulators, such as hysteresis controller or voltage pulse-width modulation (PWM) controller.

As the motor speed increases, the back-emf soon becomes comparable to the DC bus voltage, and it is necessary to phase advance the turn-on angle

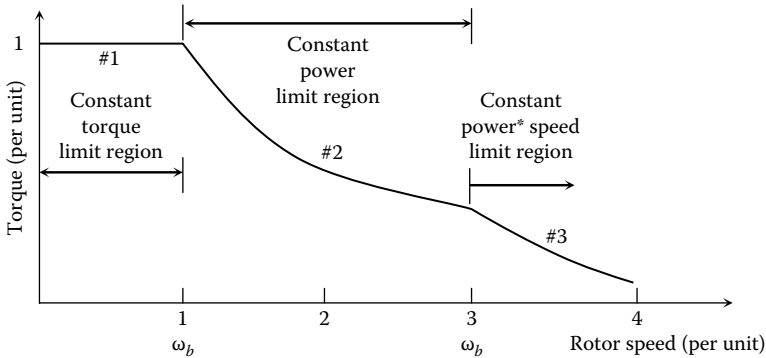


FIGURE 6.44

Torque–speed characteristics of an SRM drive.

so that the current can rise up to the desired level against a lower back-emf. Maximum current can still be forced into the motor by PWM or chopping control to maintain the maximum torque production. The phase excitation pulses also need to be turned off at a certain time before the rotor passes alignment to allow the freewheeling current to decay so that no braking torque is produced.

Region 2: When the back-emf exceeds the DC bus voltage in high-speed operation, the current starts to decrease once pole overlap begins and PWM or chopping control is no longer possible. The natural characteristic of the SRM, when operated with fixed supply voltage and fixed conduction angle θ_{dwell} (also known as the dwell angle), begins when the phase excitation time falls off inversely with speed and so does the current. Since the torque is roughly proportional to the square of the current, the rapid fall in torque with speed is countered by adjusting the conduction angle. Increasing the conduction angle increases the effective amps delivered to the phase. The torque production is maintained at a level high enough in this region by adjusting the conduction angle θ_{dwell} with the single-pulse mode of operation. The controller maintains the torque inversely proportional to the speed; hence, this region is called the constant power region. The conduction angle is also increased by advancing the turn-on angle until the θ_{dwell} reaches its upper limit at speed ω_p .

The medium speed range through which constant power operation can be maintained is quite wide and very high maximum speeds can be achieved.

Region 3: The θ_{dwell} upper limit is reached when it occupies half the rotor pole pitch, i.e., half the electrical cycle. θ_{dwell} cannot be increased further because otherwise the flux would not return to zero and the current conduction would become continuous. The torque in this region is governed by the natural characteristics, falling off as $1/\omega^2$.

The torque–speed characteristics of the SRM are similar to that of a DC series motor, which is not surprising considering that the back-emf is proportional to current, while the torque is proportional to the square of the current.

Problems

- 6.1 A 460 V, 60 Hz, 6 pole, 1176 rpm, Y-connected induction motor has the following parameters referred to the stator at rated condition:

$$R_s = 0.19 \, \Omega, R_r = 0.07 \, \Omega, X_s = 0.75 \, \Omega, X_r = 0.67 \, \Omega \text{ and } X_m = \infty$$

- Find the speed of the motor for a braking torque of 350 N m and the inverter frequency of 40 Hz when the motor is supplied at rated voltage.
- 6.2 A three-phase induction machine is operated from a variable voltage, fixed frequency source. (a) Derive an expression for machine efficiency in terms of slip (not in terms of torque and speed). Include only stator and rotor copper losses and core loss in P_{loss} . Model core loss by a constant resistance in the equivalent circuit. To simplify the analysis, assume that core loss resistance and magnetizing reactance are large compared to the other parameters. Under this assumption, you can use an approximate equivalent circuit where the core loss resistance and magnetizing reactance are directly across the stator terminals. (b) Does motor efficiency depend on terminal voltage? Calculate the slip that maximizes motor efficiency.
- 6.3 Find the condition of operation that minimizes the losses in a separately excited DC machine. (Start by writing an equation for P_{loss} in terms of the field currents and armature currents. Assuming linearity for all the non-linear functions, establish the relation between armature current and field current and then find the condition for minimum P_{loss} .)
- 6.4 Present an argument for why it is impossible to achieve maximum efficiency at every operating point (T^*, ω^*) for a PM DC machine. (Start by writing an equation for P_{loss} in terms of T , ω , and machine flux ϕ .)
- 6.5 Proceeding as in Problem 6.2, explain why it is impossible to minimize losses at any operating point (T^*, ω^*) for a series DC motor.
- 6.6 (a) A PM brushless DC has a torque constant of 0.12 N m/A referred to the DC supply. Estimate its no-load speed in rpm when connected to a 48 V DC supply.
 (b) If the armature resistance is 0.15 Ω /phase and the total voltage drop in the controller transistors is 2 V, determine the stall current and the stall torque.

- 6.7 Consider a three-phase 6/8 SRM. The stator phases are excited sequentially with a total time of 25 ms required to excite all the three phases. Find the angular velocity of the rotor. Express your answer both in rad/s and rpm.
- 6.8 The following flux equation describes the nonlinear characteristics of a three-phase, 6/4 SRM:

$$\lambda_j(i, \theta) = \lambda_s(1 - \exp(-i_j f_j(\theta))), \quad i_j \geq 0$$

where $\lambda_s =$ saturation flux $= 0.2 \text{ V s}$ and $f(\theta) = a + b^* \cos(N_r \theta - (j - 1)2\pi/m)$.

Here, $j = 1, 2, 3$ denotes the phase number and $m = 3$. Also, given $a = .024$ and $b = .019$

- Derive the expression for the phase torque $T_j(i, \theta)$.
- Plot the $\lambda-i-\theta$ characteristics for six angles between and including the unaligned and aligned positions. Take the maximum current as 100 A.
- Plot the $T-i-\theta$ characteristics between the unaligned and aligned rotor positions. Take the maximum current as 100 and 10 A current steps for the torque characteristics.

References

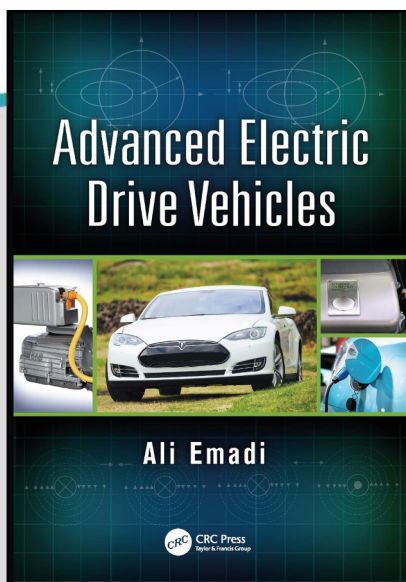
- G. Dubey, *Power Semiconductor Controlled Drives*, Prentice Hall, Englewood Cliffs, NJ, 1989.
- R.H. Park, Two-reaction theory of synchronous machines—Generalized method of analysis—Part I, *AIEE Transactions*, 48, 716–727, July 1929.
- P. Vas, *Electric Machines and Drives: A Space-Vector Theory Approach*, Oxford University Press, Oxford, U.K., 1992.
- D.W. Novotny and T.A. Lipo, *Vector Control and Dynamics of AC Drives*, Oxford University Press, Inc., New York, 1996.
- N. Mohan, *Electric Drives—An Integrated Approach*, MNPERE, Minneapolis, MN, 2001.
- T.J.E. Miller, *Brushless Permanent Magnet and Switched Reluctance Motor Drives*, Oxford University Press, Oxford, U.K., 1989.
- P.J. Lawrenson, J.M. Stephenson, P.T. Blenkinsop, J. Corda, and N.N. Fulton, Variable-speed switched reluctance motors, *IEE Proceedings*, Pt. B, 127(4), 253–265, July 1980.
- T.J.E. Miller, *Switched Reluctance Motors and Their Control*, Magna Physics Publishing, Hillsboro, OH and Oxford Science Publications, Oxford, U.K., 1993.
- M.N. Anwar, I. Husain, and A.V. Radun, A comprehensive design methodology for switched reluctance machines, *IEEE Transactions on Industry Applications*, 37(6), 1684–1692, November–December 2001.



CHAPTER

3

FUNDAMENTALS OF CONVENTIONAL VEHICLES AND POWERTRAINS



This chapter is excerpted from
Advanced Electric Drive Vehicles
by Ali Emadi

© 2014 Taylor & Francis Group. All rights reserved.



[Learn more](#)

2 Fundamentals of Conventional Vehicles and Powertrains

William Long and Berker Bilgin

CONTENTS

2.1	Longitudinal Vehicle Model	15
2.2	Longitudinal Resistance	16
2.2.1	Aerodynamic Drag	16
2.2.2	Grading Resistance	16
2.2.3	Rolling Resistance	17
2.3	Total Tractive Force	17
2.4	Maximum Tractive Effort and Powertrain Tractive Effort.....	18
2.5	Vehicle Performance.....	19
2.5.1	Maximum Speed of a Vehicle	19
2.5.2	Gradeability	20
2.5.3	Acceleration Performance	20
2.6	Braking Performance and Distribution	21
2.6.1	Braking Force	21
2.6.2	Braking Characteristics of a Two-Axle Vehicle	22
2.7	Vehicle Power Plant and Transmission Characteristics.....	22
2.7.1	Power Plant Characteristics	22
2.7.2	Transmission Characteristics.....	23
2.7.2.1	Manual Transmission.....	24
2.7.2.2	Automatic Transmission	24
2.7.2.3	Continuously Variable Transmission	25
	Chapter Review Problems.....	25

2.1 LONGITUDINAL VEHICLE MODEL

In practical terms, a vehicle not only travels on a level road but also up and down the slope of a roadway as well as around corners. In order to model this motion, the description of the roadway can be simplified by considering a straight roadway with two-dimensional movement. This two-dimensional model will focus on vehicle performance, including acceleration, speed, and gradeability, as well as braking performance.

Figure 2.1 shows the forces acting on a vehicle as it travels at a given speed along a roadway with a specific grade. Fundamental principles of mechanical systems can be used to express the relationship between the vehicle acceleration and the forces acting on the vehicle body as:

$$ma = F_t - F_w - F_g - F_r \quad (2.1)$$

where m is the vehicle mass, a is the acceleration of the vehicle. F_t is the total tractive force acting upon the vehicle body, F_w is the aerodynamic drag force, F_g is the grading resistance force, and F_r is the rolling resistance force.

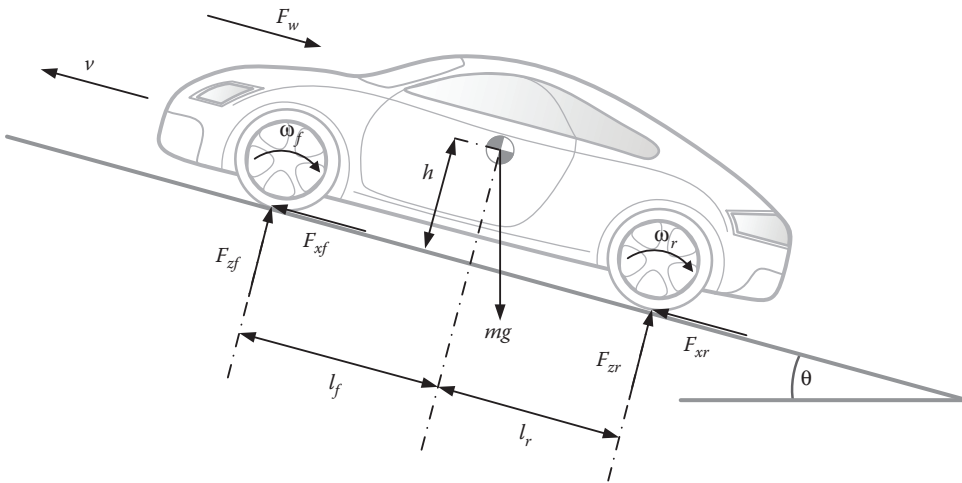


FIGURE 2.1 Forces acting on a vehicle.

2.2 LONGITUDINAL RESISTANCE

2.2.1 AERODYNAMIC DRAG

As air travels over the body of the vehicle, it generates normal pressure and shear stress on the vehicle's body. The external aerodynamic resistance is comprised of two components, shape drag and skin friction. The shape drag arises from high-pressure areas in front of the vehicle and low-pressure areas behind the vehicle that are created as the vehicle propels itself through the air. These high-and low-pressure zones act against the motion of the vehicle, while the skin friction is due to the shear stress in the boundary layer on the surface of the body of the vehicle. In comparison, shape drag is much larger in magnitude than skin friction and constitutes more than 90% of the total external aerodynamic drag of a vehicle. Aerodynamic drag is a function of effective vehicle frontal area, A , and the aerodynamic drag coefficient, C_d , which are highly dependent on the design of the vehicle body:

$$F_w = \frac{1}{2} \rho A C_d (V + V_w)^2 \quad (2.2)$$

where ρ is the air density, V is the vehicle longitudinal speed, and V_w is the wind speed.

2.2.2 GRADING RESISTANCE

As a vehicle travels up or down an incline, gravity acting on the vehicle produces a force which is always directed downward, as shown in Figure 2.1. This force opposes the forward motion during grade climbing and aids in the forward motion during grade descending. In typical vehicle performance models, only uphill operation is considered as it resists the total tractive force. The equation for this force is a function of the road angle θ , vehicle mass m , and the gravitational acceleration g :

$$F_g = mg \sin(\theta) \quad (2.3)$$

For a relatively small angle of θ , $\tan \theta = \sin \theta$. Using this approximation, the grade resistance can be approximated by $mg \tan \theta$, or mgG , where G is the slope of the grade.

2.2.3 ROLLING RESISTANCE

Rolling resistance force is a result of the hysteresis of the tire at the contact patch as it rolls along the roadway. In a stationary tire, the normal force due to the road balances the force due to the weight of the vehicle through the contact patch which is in line with the center of the tire. When the tire rolls, as a result of tire distortion or hysteresis, the normal pressure in the leading half of the contact patch is higher than that in the trailing half. The normal force due to the road is shifted from the center of the tire in the direction of motion. This shift produces a moment that exerts a retarding torque on the wheel. The rolling resistance force is the force due to the moment, which opposes the motion of the wheel, and always assists in braking or retarding the motion of the vehicle. The equation for this force is a function of the normal load F_z and the rolling resistance coefficient f_r , which is derived by dividing the distance the normal force due to the road is shifted by the effective radius of the tire r_d .

$$F_r = F_z f_r \cos(\theta) \quad (2.4)$$

2.3 TOTAL TRACTIVE FORCE

Equation 2.1 shows the factors affecting vehicle performance with a particular interest in the overall tractive force of the vehicle.

$$ma = F_t - F_w - F_g - F_r \Rightarrow ma = (F_{tf} + F_{tr}) - (F_w + F_g + F_{rf} + F_{rr}) \quad (2.5)$$

By rearranging Equation 2.1 we arrive at an equation that expresses longitudinal vehicle motion as a combination of total tractive effort minus the resistance. In order to determine the total tractive effort, the normal forces, F_{zf} and F_{zr} , need to be determined. The front and rear tire contact points should satisfy the equilibrium equations for moments:

$$\sum M_r = 0, \quad \sum M_f = 0 \quad (2.6)$$

Therefore,

$$F_{zf}(l_f + l_r) + F_w h_w + (mg \sin(\theta)h) + (mah) - (mg \cos(\theta)l_r) = 0 \quad (2.7)$$

and

$$F_{zr}(l_f + l_r) - F_w h_w - (mg \sin(\theta)h) - (mah) - (mg \cos(\theta)l_f) = 0 \quad (2.8)$$

where F_{zf} and F_{zr} are the normal forces on the front and rear tires, l_f and l_r are the distances between the front and rear axles and vehicle center of gravity, respectively. h_w is the height for effective aerodynamic drag force and h is the height of vehicle center of gravity. For simplicity, usually h_w is assumed to be equal to h . Equations 2.7 and 2.8 can be rearranged to solve for the normal forces on the front and rear tires:

$$F_{zf} = \frac{-F_w h - mg \sin(\theta)h - mah + mg \cos(\theta)l_r}{l_f + l_r} \quad (2.9)$$

$$F_{zr} = \frac{F_w h + mg \sin(\theta)h + mah + mg \cos(\theta)l_f}{l_f + l_r} \quad (2.10)$$

The total tractive force can be expressed as the tractive forces acting on each tire:

$$F_t = F_{xf} + F_{xr} \tag{2.11}$$

where F_{xf} and F_{xr} are the longitudinal forces on the front and rear tires, respectively. The friction generated between the tire–road contact patch creates the longitudinal force. Therefore, the longitudinal force generated on each tire can be represented as a function of the tire friction coefficient and the normal force:

$$F_{xf} = \mu_f F_{zf}, \quad F_{xr} = \mu_r F_{zr} \tag{2.12}$$

where F_{zf} and F_{zr} are the normal forces on the front and rear tires given by Equations 2.9 and 2.10 and μ_f and μ_r are the friction coefficients on the front and rear tires, respectively.

2.4 MAXIMUM TRACTIVE EFFORT AND POWERTRAIN TRACTIVE EFFORT

The maximum tractive effort of the vehicle is proportional to the slip ratio of the tire, which represents the difference between the angular tire speed and the vehicle speed. During acceleration, the slip ratio of the front and rear tires can be expressed as:

$$\sigma_r = \frac{r_{wr}\omega_r - V}{r_{wr}\omega_r}, \quad \sigma_f = \frac{r_{wf}\omega_f - V}{r_{wf}\omega_f} \tag{2.13}$$

where r_{wf} and r_{wr} are the radii of the front and rear tires, and ω_f and ω_r represent their angular speed. Slip-friction coefficient characteristics of a tire have a nonlinear relationship and depend on the road surface conditions, as shown in Figure 2.2. The Pacejka Tire Model is widely used to define these characteristics:

$$\mu_{f/r} = D \sin(C \arctan(B \sigma_{f/r} - E(B \sigma_{f/r} - a \tan(B \sigma_{f/r})))) \tag{2.14}$$

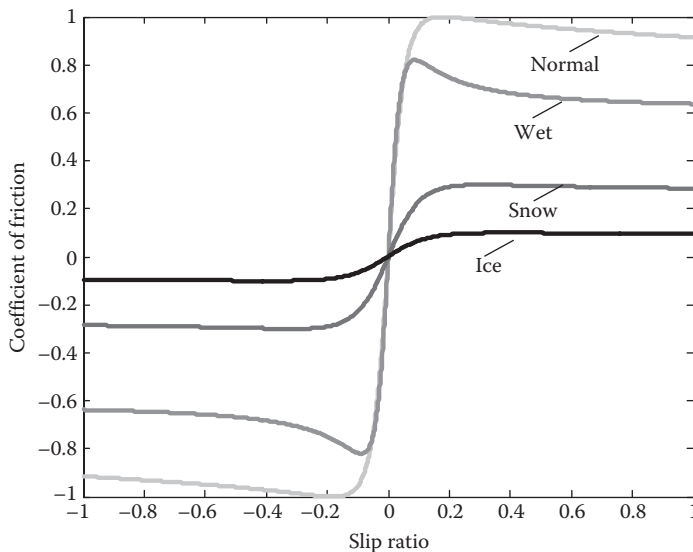


FIGURE 2.2 Typical tire slip ratio–friction coefficient characteristics.

where μ_{fr} and σ_{fr} are the friction coefficient and slip ratio of the front or rear tire. B , C , D , and E are tire coefficients and their values depend on the road surface conditions.

The sum of the torques on each wheel determines the rate of change of wheel speeds:

$$J_f \frac{d\omega_f}{dt} = T_{ef} - T_{rf}, \quad J_r \frac{d\omega_r}{dt} = T_{er} - T_{rr} \quad (2.15)$$

where J_f and J_r are the inertias, T_{ef} and T_{er} are the traction torques delivered from the drivetrain, T_{rf} and T_{rr} are the reaction torques due to the tractive force of the front and rear tires, respectively. The reaction and friction torques on the front and rear tires can be defined as:

$$T_{rf} = r_{wf} F_{xf}, \quad T_{rr} = r_{wr} F_{xr} \quad (2.16)$$

where ω_f and ω_r are the angular speed, and C_f and C_r are the friction coefficients of the front and rear tires, respectively.

The traction torques on the tires, T_{ef} and T_{er} are provided from the powertrain. If the vehicle is rear wheel or front wheel driven, the nondriven wheel provides no traction torque. Therefore, for nondriven wheels, Equation 2.15 can be expressed as:

$$J_r \frac{d\omega_r}{dt} = -r_{wr} F_{xr} \quad (2.17)$$

In conventional vehicles, the source of the traction torque is the internal combustion engine and the output power of the engine is supplied to the tires through the clutch, the transmission, and the differential. Therefore, the traction torque applied for either a front or a rear wheel drive vehicle can be expressed as:

$$T_p = T_{en} i_t i_0 \eta_p \quad (2.18)$$

where T_{en} is the torque from the engine, i_t is the gear ratio of the transmission, i_0 is the gear ratio of the differential, and η_p is the total efficiency of the powertrain.

2.5 VEHICLE PERFORMANCE

Performance characteristics of a road vehicle refer to its capability to both accelerate and decelerate, and negotiate grades in a straight-line motion. These characteristics are different depending on the vehicle's type and size. Mass of the vehicle is of great importance to vehicle performance. By researching not only vehicle electrification, but lightweight materials as well, all aspects of vehicle performance would be improved, including fuel economy. The tractive and braking effort developed by the tires and the resisting forces acting on the vehicle determine the performance potential of the vehicle. Typically, overall vehicle performance is also concerned with cornering ability, but as this is mainly a function of suspension geometry and vehicle design it is outside the scope of this chapter.

2.5.1 MAXIMUM SPEED OF A VEHICLE

The maximum speed of a vehicle is the highest constant cruising speed that the vehicle can achieve at full power on a level road. The maximum speed of a vehicle is calculated with full torque from the traction source on a flat road when the tractive force and the resistive force are at equilibrium.

Since the vehicle acceleration and road gradient are zero at this point, the equilibrium can be represented as:

$$F_t = F_w + F_r \quad (2.19)$$

Considering that the wheel speed is also constant, the tractive force can be expressed in terms of the torque applied to the wheels:

$$F_t = \frac{T_p}{r_d} \quad (2.20)$$

where T_p can be expressed as in Equation 2.18.

The aerodynamic drag force F_w and the rolling resistance force F_r have been derived in Equations 2.2 and 2.4, respectively.

Combining Equations 2.19, 2.20, 2.2, 2.4, and 2.18 yields:

$$\frac{T_{en} i_t i_0 \eta_p}{r_d} = mgf_r + \frac{1}{2} \rho AC_d V^2 \quad (2.21)$$

$$V = \sqrt{\frac{2(((T_{en} i_t i_0 \eta_p)/r_d) - mgf_r)}{\rho AC_d}} \quad (2.22)$$

2.5.2 GRADEABILITY

The gradeability of a vehicle is the maximum gradient on which the vehicle can start climbing from stand-still with all the wheels of the vehicle on the gradient at the time of start.

As a vehicle drives on a road with a small grade and constant speed, the tractive effort and resistance equilibrium can be written as an extension of Equations 2.19 and 2.21 to include gradeability for small angles, as calculated in Equation 2.3.

$$F_t = F_w + F_r + F_g \quad (2.23)$$

$$\frac{T_{en} i_t i_0 \eta_p}{r_r} = mgf_r + \frac{1}{2} \rho AC_d V^2 + mgG \quad (2.24)$$

$$G = \frac{((T_{en} i_t i_0 \eta_p)/r_r) - mgf_r - (1/2)\rho AC_d V^2}{mg} \quad (2.25)$$

2.5.3 ACCELERATION PERFORMANCE

When high-performance vehicles are compared to one another, one of the first statistics to be reviewed is the acceleration performance. It is most often referred to as a vehicle's 0–60 mph time. Referring to Equation 2.1, the acceleration of the vehicle on level ground can be written as:

$$a = \frac{F_t - F_r - F_w}{m\delta} \quad (2.26)$$

where δ is the mass factor which takes into account the mass moments of inertia of the rotating components involved during a change of acceleration.

Combining Equations 2.26, 2.20, 2.2, 2.4, and 2.18 yields:

$$a = \frac{((T_{en} i_t i_0 \eta_p)/r_d) - mgf_r - (1/2)\rho AC_d AV^2}{m\delta} \quad (2.27)$$

By integrating Equations 2.28 and 2.29 from zero to potentially 60 mph, the predicted acceleration time and distance for a vehicle can be calculated:

$$t = m\delta \int_{v_1}^{v_2} \frac{V}{((T_{en} i_t i_0 \eta_p)/r_d) - mgf_r - (1/2)\rho AC_d AV^2} dV \quad (2.28)$$

$$S = m\delta \int_{v_1}^{v_2} \frac{1}{((T_{en} i_t i_0 \eta_p)/r_d) - mgf_r - (1/2)\rho AC_d AV^2} dV \quad (2.29)$$

The torque of the engine during acceleration is not constant which makes these equations very difficult to solve analytically, thus numerical methods are typically used. These methods are outside the scope of this chapter.

2.6 BRAKING PERFORMANCE AND DISTRIBUTION

Conventional brakes, disc or drum, are the single most important safety device on any vehicle. By transferring kinetic energy into thermal energy through friction between a rotating surface and a stationary brake pad, the vehicle speed is decreased, but that thermal energy is typically wasted in conventional vehicles. With the introduction of vehicle electrification, through regenerative braking with electric motors, the kinetic energy can be recovered into stored electrical energy and it can be reused rather than being wasted. This can greatly increase the overall efficiency of the vehicle. Careful attention should be paid to the brake balance of the vehicle when designing a powertrain with regenerative braking capability. In high-performance vehicles, up to 80% of the braking force may be on the front axle, which creates a much larger potential to recapture energy at the front wheels when compared with a rear wheel setup.

Proper brake balance during the braking cycle is extremely important as the vehicle will not achieve the maximum braking deceleration unless all four tires are brought to the peak friction level simultaneously. Improper brake balance will cause either the front or rear wheels to lock up prematurely and these stationary wheels will lose cornering traction. Proper brake balance is a function of the loads on the wheels, which is in turn a function of the deceleration.

2.6.1 BRAKING FORCE

The braking force F_b , due to the brake system, which is developed on the interface between the road and the tire, is the primary braking force. When the braking force is below the tire–road adhesion limit, the braking force is given by:

$$F_b = \frac{T_b - \sum I\alpha_{an}}{r} \quad (2.30)$$

where T_b is the applied brake torque, I is the rotating inertia connected with the wheel being decelerated, α_{an} is the corresponding angular deceleration, and r is the rolling radius of the tire. Once

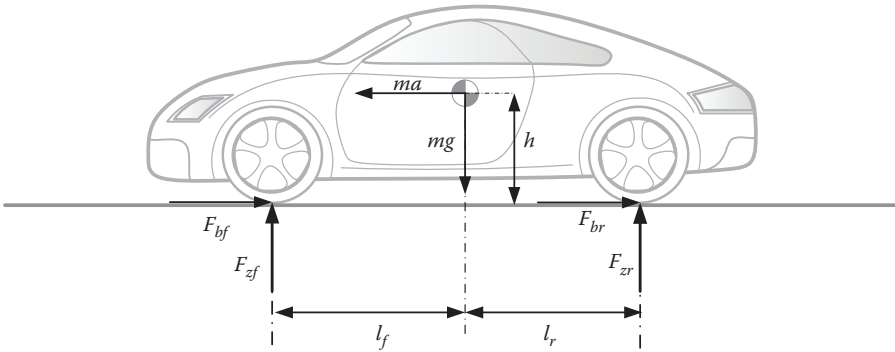


FIGURE 2.3 Vehicle braking forces on a level road.

the braking force reaches the limit of tire–road adhesion, it cannot increase any further. In addition to the braking force, the rolling resistance of tires, aerodynamic resistance, grade resistance, and powertrain resistance, as discussed previously, also affect vehicle motion during braking. For the purpose of this vehicle model, it is assumed that these are minor losses and can be neglected.

2.6.2 BRAKING CHARACTERISTICS OF A TWO-AXLE VEHICLE

When a vehicle is under braking or deceleration, an inertial reaction force is developed that is similar to the centrifugal force. Figure 2.3 shows the braking forces acting on a vehicle on a level road.

The braking force is directly proportional to the normal load acting on the tire, which is proportional to the tire–road adhesion. Similar to when total tractive force was calculated, the front and rear tire contact points should once again satisfy the equilibrium equations for moments:

$$F_{zf} = \frac{mg}{(l_f + l_r)} \left(l_r + \frac{ha}{g} \right), \quad F_{zr} = \frac{mg}{(l_f + l_r)} \left(l_f - \frac{ha}{g} \right) \quad (2.31)$$

The maximum braking force that the tire–road adhesion will support can be determined by multiplying the normal force at the front and rear wheels by the coefficient of road adhesion, μ , as expressed in Equation 2.12.

2.7 VEHICLE POWER PLANT AND TRANSMISSION CHARACTERISTICS

The two factors that limit conventional vehicle performance are the maximum tractive effort that the tire–ground adhesion can support, and the tractive effort that the overall powertrain can provide. The performance limits of the vehicle are dictated by the lesser of the tractive efforts. With the transmission in low gear and the engine throttle at maximum, the tractive effort may be limited by the nature of tire–road adhesion and loss of traction. As the transmission is shifted into higher gears, the tractive effort is often determined by the engine and transmission characteristics, which have to be taken into consideration when predicting the overall performance of a road vehicle.

2.7.1 POWER PLANT CHARACTERISTICS

For conventional vehicles, the ideal performance characteristic of a power plant is an unchanging power output across the entire operating range. At low speeds, motor torque is forced to maintain a constant value so as not to exceed the adhesion limit between the tire–ground contact area. After

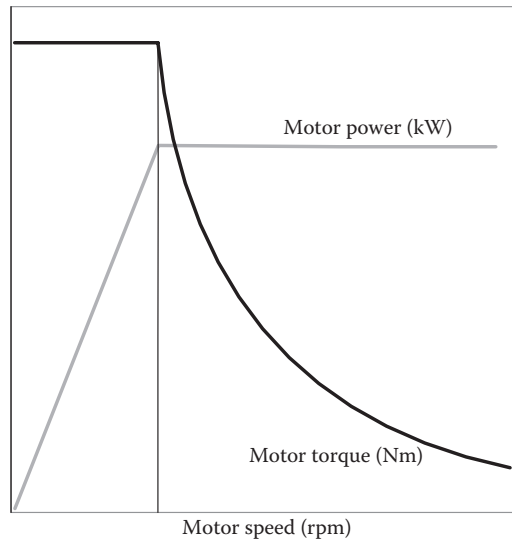


FIGURE 2.4 Ideal performance characteristics for vehicular power plants.

the constant torque low-speed range, the torque varies with speed steeply, as shown in Figure 2.4. Constant power characteristics provide conventional vehicles with a high tractive effort at low speeds, which improves acceleration, grade climbing, and towing capacity. The internal combustion engine has been the standard power plant in conventional vehicles for over a century because of its relatively high power-to-weight ratio and low cost, but it is not without its shortcomings. Typically, an internal combustion engine has torque–speed characteristics that do not directly correlate with the ideal performance characteristics required by traction.

When compared with an ideal torque–speed profile, as shown in Figure 2.4, typical internal combustion engines have a relatively flat profile, which is why a multiple gear transmission is usually employed to modify it. As an internal combustion engine moves through its typical torque and power curves, representative characteristics are developed in each speed range that can be used to predict vehicle performance. The engine begins operating smoothly at idle speed, and as the engine speed approaches an intermediate range, good combustion quality and maximum engine torque are reached. As the speed increases further, the increasing losses in the air-induction manifold and the steady decline in engine torque cause the mean effective pressure to decrease. Power output continues to increase to its maximum at a specific high engine speed. Beyond this peak power point the engine torque decreases more rapidly as the engine speed is increased, which results in the decline of engine power output.

2.7.2 TRANSMISSION CHARACTERISTICS

The term “transmission” refers to all of the systems or subsystems used for transmitting the engine power to the driven wheels or sprockets. The principal requirements for the transmission are to attain the desired maximum vehicle speed with an appropriate engine, to be able to move the vehicle on a steep slope as well as maintain speed on a gentle slope in high gear, and to properly match the engine characteristics to achieve the desired operating fuel economy and acceleration rate.

The two most common types of transmissions for conventional vehicles are the manual gear transmission and the automatic transmission with a torque converter. Other types of transmissions, such as the continuous variable transmission, are also in use and are beginning to gain popularity due to their relatively high overall efficiency.

2.7.2.1 Manual Transmission

Manual transmissions were the first gearbox designs used in conventional vehicles and were used for decades before automatic transmissions were introduced. These transmissions are still popular due to their simplicity, low cost, and high efficiency. The term “manual” implies that the driver must perform the shifting from gear to gear manually. A manual gear transmission consists of a clutch, gearbox, final drive, and driveshaft. The gearbox provides a number of gear reduction ratios, between three and five for passenger cars, and more for heavy commercial vehicles.

In determining maximum and minimum gear ratios, we can think back to the two factors that limit conventional vehicle performance. The maximum speed requirement determines the ratio of the highest gear. On the other hand, the gear ratio of the lowest gear is determined by the requirement of the maximum tractive effort or the gradeability, which is often assumed to be 33%. Choosing the ratios between high and low gear should be spaced in such a way that they will provide the tractive effort–speed characteristics as close to the ideal as possible, but unfortunately this is not always achievable. Traditionally, in conventional vehicles, the gear ratios are often chosen to minimize the time required to reach a specific speed or the maximum speed of the vehicle. With fuel economy moving to the forefront of vehicle design, a geometric progression approach, where consecutive gear ratios are very close to one another, could be used. The basis for this is to have the engine operating within the same speed range in each gear. This would ensure that in each gear, the operating fuel economy is similar.

2.7.2.2 Automatic Transmission

With an automatic transmission a driver no longer needs to actively change gears during driving, thus making the vehicle easier to drive. Automatic transmissions use fluid to transmit power in the form of torque and speed and are widely used in conventional passenger vehicles. In a conventional automatic transmission, the clutch is replaced with a fluid coupling or torque converter to eliminate engaging and disengaging action during gear changes. The torque converter’s three major components, shown in Figure 2.5 are the pump impeller, the turbine runner, and the stator. When the impeller is driven by the engine, the fluid in the impeller rotates with it, and as the speed increases, centrifugal force causes the fluid to flow into the turbine. The hydraulic fluid in the converter transfers torque through the kinetic energy of the transmission fluid as it is forced from the pump impeller to the turbine. The higher the engine speed the greater the torque applied to the turbine. The stator is located between the pump impeller and the turbine. The vanes of the stator catch the fluid as it leaves the turbine runner and redirects it so that it strikes the back of the vanes of the pump impeller giving it added torque. The major advantages of the automatic transmission are that it

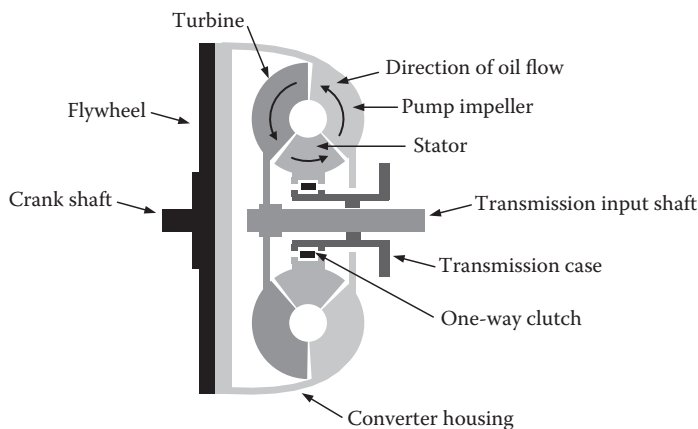


FIGURE 2.5 Torque converter cutaway schematic.

prohibits the engine from stalling, and it provides torque–speed characteristics that approach the ideal characteristics discussed previously. The major disadvantages of the automatic transmission are its low efficiency in a stop and go drive cycle and its very complicated construction.

2.7.2.3 Continuously Variable Transmission

As the interest in improving the fuel economy of automotive vehicles continues to grow, continuously variable transmissions (CVT) have attracted a great deal of attention. This type of transmission provides a continuously variable reduction ratio within a certain range, thus providing an infinite number of gear ratios. This allows the engine to operate under the most economical conditions over a wide range of vehicle speeds. It is therefore possible to achieve an ideal torque–speed profile, because any engine power output to the transmission can be applied to the wheels at any speed.

A belt CVT system is similar to standard belt–pulley drive, with one pulley connected to the engine shaft and the other connected to the output shaft. The exception, however, is that the half pulleys are not fixed and are able to move apart. Both pulleys have fixed axes of rotation at a distance from each other. The sides of each pulley are controlled so that they may move apart or together laterally, varying the effective diameter on which the belt grips. The overall lateral displacement of each pulley is the opposite of the other.

CHAPTER REVIEW PROBLEMS

Problem 1

On a 20°C sunny day with no wind speed, and an air density of 1.2 kg/m³, a 1500 kg vehicle travels along an asphalt roadway with a 6° grade at 100 km/h and a rolling resistance coefficient of 0.013. The vehicle center of gravity is located 0.6 m from the ground in the center of the 2.5 m wheelbase with 0.66 m wheels and has a frontal area of 2.05 m² and a drag coefficient of 0.32.

Calculate the aerodynamic, grading, and rolling resistance.

Problem 2

After some engine and transmission performance upgrades, the same vehicle is taken to a test track to find out the new vehicle top speed. The upgrades have increased engine torque to 450 Nm and engine horsepower to 300 kW and an overall powertrain efficiency of 88%. After the upgrades, the minimum gear ratio of the transmission is 0.9, and the differential gear ratio is 3.21.

Calculate the maximum speed of the vehicle.

Problem 3

The same vehicle travels along a level asphalt roadway at 100 km/h, with a coefficient of road adhesion of 0.72, and encounters a large obstacle 50 m ahead and needs to stop to avoid striking the obstacle.

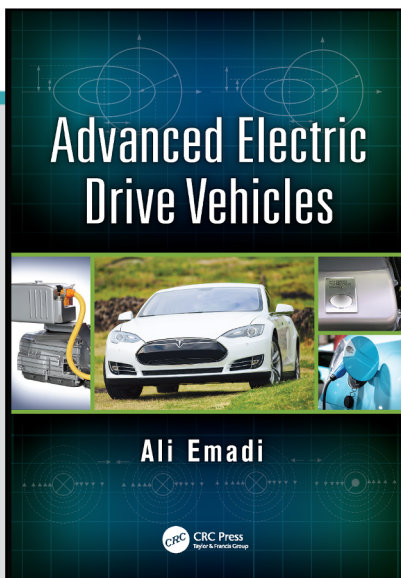
Calculate the braking force at the front and rear wheels that is required to stop just before the obstacle.



CHAPTER

4

HYBRID ENERGY STORAGE SYSTEMS



This chapter is excerpted from
Advanced Electric Drive Vehicles
by Ali Emadi

© 2014 Taylor & Francis Group. All rights reserved.

 [Learn more](#)

8 Hybrid Energy Storage Systems

Omer C. Onar and Alireza Khaligh

CONTENTS

8.1	Combined Battery and UC Topologies	284
8.1.1	Topology 1: Passive Parallel Configuration	285
8.1.2	Topology 2: UC/Battery Configuration	285
8.1.3	Topology 3: Battery/UC Configuration	286
8.1.4	Topology 4: Cascaded Converters Configuration	287
8.1.5	Topology 5: Multiple Parallel-Connected Converters Configuration	288
8.1.6	Topology 6: Multiple Dual-Active-Bridge Converters Configuration	289
8.1.7	Topology 7: Dual-Source Bidirectional Converters Configuration	289
8.1.8	Topology 8: Multiple-Input Converter Configuration	291
8.1.9	Topology 9: Multiple Modes Single-Converter Configuration	292
8.1.10	Topology 10: Interleaved Converter Configuration	293
8.1.11	Topology 11: Switched Capacitor Converter Configuration	293
8.1.12	Topology 12: Coupled Inductor-Based Hybridization Architecture	294
8.2	Other Energy Storage Devices and Systems: Flywheels, Compressed Air Storage Systems, and Superconducting Magnetic Storage Systems	296
8.2.1	Flywheel ESS	296
8.2.2	Compressed Air-Pumped Hydraulics-Based Storage System	297
8.2.3	Superconducting Magnetic ESS	298
8.3	Conclusions	300
8.4	Simulations and Analyses of Hybrid ESS Topologies for PEVs	301
8.4.1	Simulation and Analysis of Passive Parallel Configuration	302
8.4.2	Simulations and Analysis of Cascaded Converters Topology	304
8.4.3	Simulation and Analysis of Parallel-Connected Multiconverters Topology	309
8.4.4	Conclusions	311
	Problems	313
	References	313

In this chapter, hybrid energy storage systems (ESS) are presented for the decoupled power and energy components of the plug-in electric vehicles (PEVs^{*}). A stand-alone battery system with an energy capacity sized to propel the vehicle some distance at a moderate speed on a single charge in an all-electric mode may not be sufficient to satisfy peak demand periods and transient load variations in PEVs. In such a case, the battery would need to be oversized to supply the extra power needed to overcome these limitations, thus increasing the weight, volume, and cost as well as the number and depth of charge/discharge cycles. All these factors lead to concern over battery lifetime, which is one of the strongest barriers currently preventing rapid commercialization of PEVs. Alternatively, an ultra-capacitor (UC) bank can supply or recapture large bursts of power at high C-rates.

^{*} PEV includes all-electric vehicles (also known as battery electric vehicles) and plug-in electric vehicles (PHEVs).

Battery/UC hybrid operation provides an improved solution over the stand-alone battery design in terms of improved power management and control flexibility. Moreover, the voltage of the battery pack can be selected to be lower than the UC bank, which will result in cost and size reduction of the battery. Furthermore, since the battery is not prone to supply peak and sharp power variations, the stress on the battery is reduced and the battery lifetime can be increased. Utilizing UCs tends to result in a more effective capturing of braking energy, especially in sudden/hard braking conditions, and this would further increase the fuel economy as larger energy transients are able to flow or be recaptured more easily.

8.1 COMBINED BATTERY AND UC TOPOLOGIES

To provide more efficient propulsion without sacrificing the performance or increasing fuel consumption, more than one energy storage device, each with different power/energy characteristics, can be used in PEVs. In such a system, proper power budgeting based on the specific characteristics of energy sources should result in higher efficiency, longer life and reduced wear on energy sources, and an overall reduction in size and cost. The combination of energy sources should be able to store, supply, and recapture high-power pulses in a typical or worst-case drive cycle, as well as supply the steady demands of the car. A hybrid topology composed of a high-power-density component such as an UC and a high-energy-density component such as a rechargeable battery offers a compromise of both [1,2].

The energy storage devices in electric vehicles (EVs) should be able to meet the demands that the vehicle may encounter under any condition. Rechargeable chemical batteries are the most traditional energy storage sources for EVs. However, since the source needs to supply the peak power demands of the traction motor during transient and rapid accelerations, and since the current technologies do not provide a battery with sufficiently high-power densities, the size and cost of the battery pack significantly increase if it is required to supply all the load demands.

A PEV traction battery may be sized to successfully meet the energy capacity needs for a given single-charge travel distance requirement, but since the present generation of highly energy-dense lithium-ion battery technology has a relatively low-power density, this single power source may not be capable of sourcing or sinking large, short bursts of acceleration or regenerative braking energy. Moreover, battery longevity is directly related to both the depth of discharge and quantity of micro or macro charge/discharge cycles, that is, the short, powerful charge/discharge cycles associated with sharp acceleration and hard regenerative braking. Battery C-rate is defined as the parameter, which expresses battery discharge intensity [3], and when designing a battery-powered system, low C-rates will tend to increase battery life span and thus, instantaneous charge/discharge pulses or fast-fluctuating currents should be avoided. The problems associated with cycling batteries at high C-rates include decreased capacity, excessive heating (which would require additional cooling), and increased DC resistance (DCR); with capacity and DCR being those metrics used to define battery performance and therefore end of life.

Without a secondary ESS, the battery pack must supply all vehicle power demands that may result in an oversized system with a massive energy density to compensate for power-density shortcomings. This would result in increased cost and size of the battery pack or, if a smaller pack was used, it would shorten the battery lifetime, causing potential thermal runaway problems [4]. For this reason, UCs are proposed, because of their higher specific power and cycling efficiency [5], to relieve the battery bank of peak power transfer stresses. Combining these two energy sources, a hybrid system composed of batteries and UCs can not only meet both energy and power requirements of the drive train better, but also provide the flexibility of using smaller batteries with less peak-output power [6,7]. Owing to their very low internal resistances, UCs have very small time constants and can deliver high-power charge and discharge pulses [8] for relatively short durations. The manufacturer performance rating for certain UCs states a 20% decrease of initial capacitance and doubling of internal resistance over a period of 1,000,000 cycles [9]. The curves showing whether this wear and tear is linear or exponential over time are not provided, but with 1,000,000 cycle rating, it is likely that a system will not see serious degradation for a substantial length of time or energy throughput.

By employing UCs with batteries in a proper, efficient, and cost-effective manner, the peak current capacity of the overall topology can be increased. Therefore, the hybrid topology could benefit from an intermediate storage of high power in a buffer stage designed to deliver or receive current for the highest peaks, thus reducing both the number and the depth of discharge cycles of the batteries [7–11].

Different topologies for combining hybrid energy sources have been studied in the literature [7–15]. A direct parallel connection of two sources [12], a bidirectional DC/DC converter between the battery and UC bank [3–13], and two DC/DC converters sharing the same output [14] are among the conventional options.

8.1.1 TOPOLOGY 1: PASSIVE PARALLEL CONFIGURATION

Combining two power sources passively in parallel is the simplest method as the output voltages of both sources are automatically equalized by virtue of being directly connected to the same bus. The passive parallel connection topology is shown in Figure 8.1 with the bidirectional converter interfacing the common ESS bus to the DC link and motor drive. Since the converter is operated to provide constant input voltage to the DC link/motor drive, when the mechanical load on the machine increases, motor current will tend to increase, decreasing the DC link voltage. This will cause more power to be drawn from the ESS through the bidirectional converter to return the DC link to its nominal voltage. On the other hand, whenever braking occurs, the motor drive operates as a generator and captures the braking energy back to the DC link. Therefore, DC link voltage increases during braking or a reduction in mechanical load, and the bidirectional converter is operated in reverse (from DC link to ESS bus) to regulate the DC link voltage.

This topology provides simplicity and cost-effectiveness for hybrid ESSs. In this connection topology, it is expected that the UC will act faster than the battery due to its lower time constant. Therefore, it is anticipated that the UC will provide the transients and fast power variations while the battery supplies a relatively slow-varying current due to its slower dynamics [12].

However, in this topology, directly after current is drawn from the UC, since they are directly connected, the battery will supply a similar current profile for voltage equalization, since there is no active battery current waveform shaper, limiter, or controller. Battery current is, therefore, not effectively controlled [16] and this presents a drawback to the passive parallel connection topology. In addition to this drawback, the nominal battery and UC voltages must be sized to match, which puts an extra restriction on system configuration.

8.1.2 TOPOLOGY 2: UC/BATTERY CONFIGURATION

The most common UC/battery configuration connects the UC terminals to the DC link through a bidirectional DC/DC converter [17]. In this topology, the battery is directly connected to the DC link and a bidirectional interface is used for UC connection, as shown in Figure 8.2. Figure 8.3

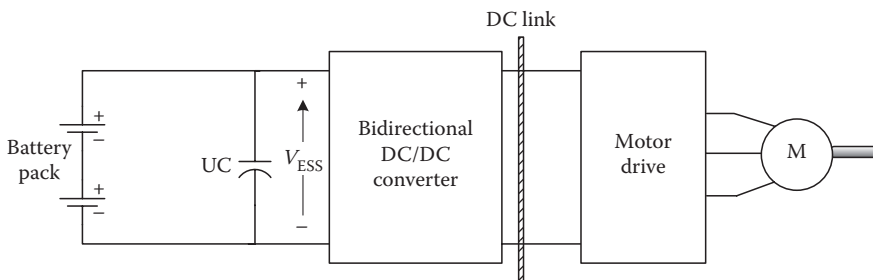


FIGURE 8.1 Passive parallel connection topology.

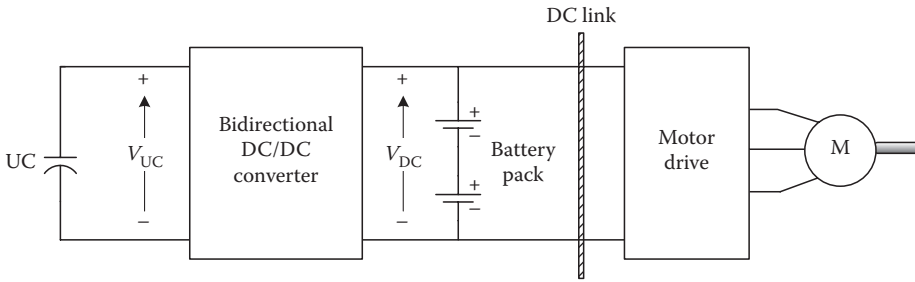


FIGURE 8.2 UC/battery configuration.

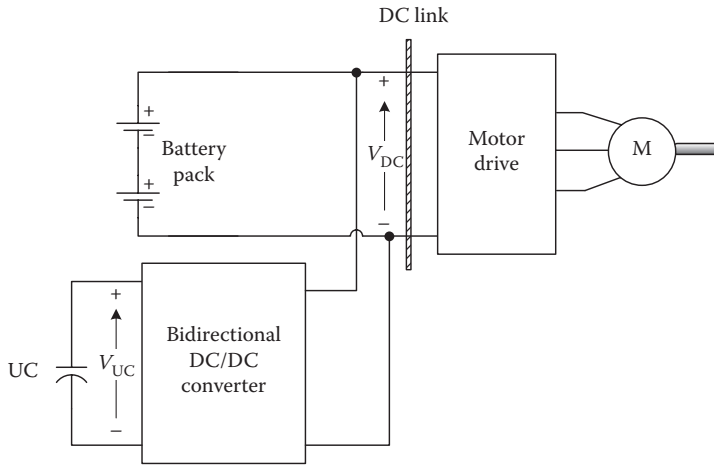


FIGURE 8.3 Another representation of the same UC/battery configuration.

shows another common view of the same connection topology. In this case, the power contribution from the UC can be effectively controlled [18], and the bidirectional DC/DC interface also helps to efficiently and more completely recapture braking energy. Moreover, an UC voltage can be selected that is different from the nominal DC link voltage, allowing the UC energy capacity to be increased or decreased regardless of the system DC voltage, since UC energy capacity varies by the square of its voltage. Since the battery is directly connected to the DC link, input voltage to the motor drive is relatively constant and further DC link voltage regulation is not required. This provides simplicity of control and voltage control loops may be eliminated.

The disadvantage of this topology is that the braking energy captured by the battery is not directly controlled. Braking energy recovered by the battery depends on the power level, battery state of charge (SoC), and the amount of energy captured by the UC. The other drawback is that the bidirectional DC/DC converter must operate properly even with low UC voltages and therefore higher current values; so, current ratings of the switches and other power electronics should be chosen appropriately.

8.1.3 TOPOLOGY 3: BATTERY/UC CONFIGURATION

For the battery/UC topology shown in Figure 8.4, the positions of the devices are simply switched as compared to the UC/battery configuration [19,20].

The main advantage of this topology is that the battery voltage can be maintained at a lower level. During braking, the UC is recharged directly from the DC link and some portion of the

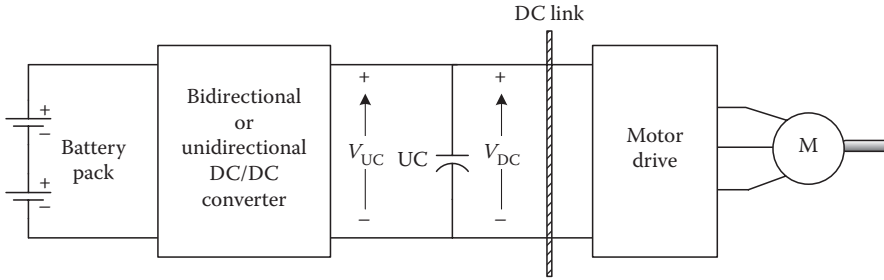


FIGURE 8.4 Battery/UC topology.

braking energy, appropriately current limited, can be transferred to the battery. Since the UC is directly connected to the DC link, it acts as a low-pass filter and takes care of fast load transients. However, the battery pack should be controlled in a way such that it continually maintains an appropriate voltage across the UC and DC link. The control strategy for the battery pack may be designed such that it supplies the average and slow-changing load variations, while the UC supplies the rest, acting as a buffer with faster dynamics. If the UC is not sized large enough or charged continually, the DC link voltage will be allowed to fluctuate over a wide range, and in this case, the motor drive inverter should be capable of operating over a large input voltage range.

In this topology, for simplicity and cost-effectiveness, the battery pack converter can be unidirectional. Since the overall system is that of a plug-in hybrid, the battery pack can be configured to only receive a charge from an on-board generator or an external source, and UC can be the only device responsible for capturing braking energy. This scheme would provide a significant amount of simplicity for power budgeting during braking.

8.1.4 TOPOLOGY 4: CASCADED CONVERTERS CONFIGURATION

Alternatively, one energy storage device can be cascaded to the motor drive through a DC/DC converter and the other cascaded through the first and a second DC/DC converter [21,22]. The cascaded converters configuration is presented in Figure 8.5.

In this configuration, both battery and UC voltages can be decoupled from the system voltage and from each other. It is preferred that the battery’s converter controls the battery output current and therefore the stress on the battery. If the UC is undersized or the battery converter is not appropriately controlled, the UC voltage can vary substantially. At low UC voltages, the input current to the UC converter can be very high, leading to higher conduction losses and the need for high-current-rated switches. Additionally, the UC DC/DC converter must provide stable operation over a wide voltage input range.

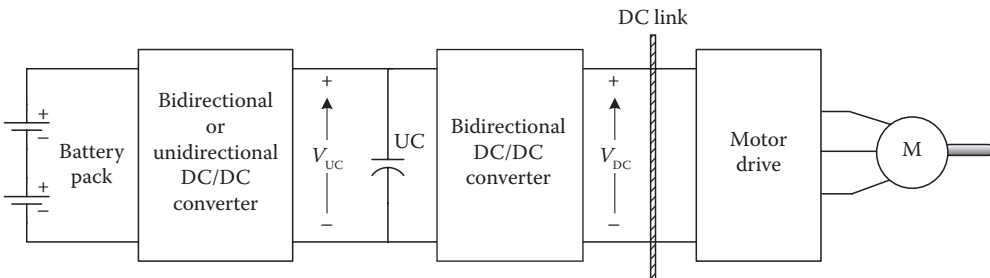


FIGURE 8.5 Cascaded converters configuration.

The major disadvantage of the cascaded converter topology is that additional losses may be encountered at the battery power flow path since there are two cascaded converters between the battery and DC link.

The battery converter can again be a unidirectional converter for control and configuration simplicity. In the case of a boost converter for the battery, the battery's power contribution can be easily controlled by current control mode [16]. The UC converter can be controlled for DC link regulation and the battery can be controlled such that it supplies a smoother current profile during the operation.

As in topology 3, the positions of the battery and UC can be switched, leading to another cascaded converters topology. However, in this case, the power contribution from the UC could possibly result in a more fluctuation voltage applied to the battery terminals. On the other hand, since the battery is the DC link side energy storage device, DC link voltage regulation could be easily accomplished by virtue of a nearly constant battery voltage.

8.1.5 TOPOLOGY 5: MULTIPLE PARALLEL-CONNECTED CONVERTERS CONFIGURATION

In this topology, each energy storage device has its own bidirectional DC/DC converter for interfacing with the DC link [11,22–24] and the outputs of each converter are all held in parallel. The block diagram of the multiple parallel-connected converters topology is given in Figure 8.6.

Although this topology is called a multiple-input converter, this is not a “true” multiple-input converter since each energy storage device has an individual converter and its contributions to the DC link are paralleled. This topology offers the highest flexibility and provides better functionality than that of the cascaded converters topology. The voltages of the battery and UC are decoupled from each other as well as the DC link voltage. Since power controls and power flow paths from the energy storage devices are totally decoupled, this topology is superior from stability, efficiency, and control simplicity points of view. The reliability is also improved since one source can keep operating through the failure of another.

As discussed in Reference 24, the battery can be operated in current control mode, supplying the load variations averaged and smoothed over a period of time. Meanwhile, the UC can be operated in voltage control mode, maintaining a nearly constant voltage across the DC link. Therefore, the UC will supply fast load variations and transients during both rapid acceleration and sudden braking conditions. This is due to the fact that these load activities directly affect the DC link voltage, and as long as DC link voltage is regulated fast enough, all load demands will be satisfied.

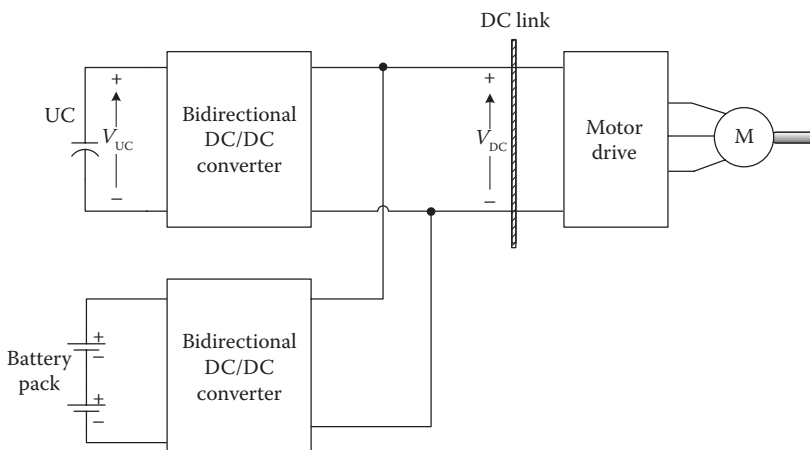


FIGURE 8.6 Multiple parallel-connected converters topology.

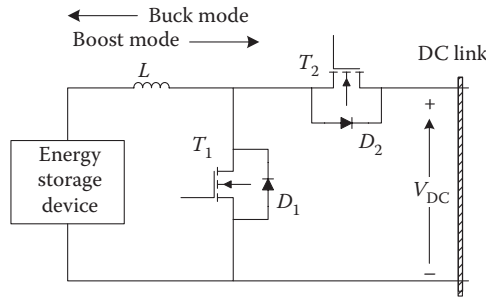


FIGURE 8.7 Bidirectional DC/DC converter.

The bidirectional DC/DC converters discussed for topologies 2 through 4 could be typical two-quadrant converters, able to operate in boost mode in one direction and buck mode in the other, as shown in Figure 8.7. This topology is also called a half-bridge bidirectional DC/DC converter.

As shown in Figure 8.7, for power flow from an energy storage device to the DC link, inductor L , switch T_1 , and diode D_2 form a boost converter. To accommodate power flow from the DC link to an energy storage device, switch T_2 , diode D_1 , and inductor L form a buck converter. Of course, other types of bidirectional converters could also be used, and some of these are presented in the following sections.

8.1.6 TOPOLOGY 6: MULTIPLE DUAL-ACTIVE-BRIDGE CONVERTERS CONFIGURATION

It is well known that conventional buck–boost converters can step the source voltage up or down at the cost of having a negative voltage output. Therefore, an inverting transformer is usually employed to obtain a positive output voltage. Although the transformer adds cost and volume to the system, it may be advantageous when there are two input sources for both isolation and coupling. Two buck–boost-type DC/DC converters for the UC and battery can be combined through the magnetic coupling of a transformer reactor [25]. However, neither conventional buck–boost nor buck–boost with transformer topologies is suitable for vehicle propulsion systems since they are not capable of bidirectional operation. On the other hand, dual-active-bridge DC/DC converters [26] can be employed for the combined operation of batteries and UCs. Although transformers typically add cost and volume to a system, the transformer in the dual-active-bridge converter operates at a very high frequency and it may therefore be very small and cheap. Having a transformer in the converter topology may be advantageous when there are two or more input sources since they can be combined through the magnetic coupling of the transformer reactor. The dual-active-bridge converter with two input sources is presented in Figure 8.8. Although this topology completely isolates the input sources from the DC link, it requires a greater number of switches at increased cost. If only isolation is required, the number of switches can be reduced by employing half-bridge inverters/rectifiers instead of full-bridge versions. This dual-active-bridge topology with half-bridge converters would cut the number of switches into half, and is given in Figure 8.9.

8.1.7 TOPOLOGY 7: DUAL-SOURCE BIDIRECTIONAL CONVERTERS CONFIGURATION

In the multiple-converters configuration, as discussed earlier, each individual converter shares the same output; hence, the combination of converters occurs at the output. Instead of paralleling the converters’ outputs at the DC link, the combination can be applied at the input, as in dual-source bidirectional converters [27,28]. The dual-source bidirectional converters configuration is presented in Figure 8.10.

Although this topology is very similar to topology 5, there is one less switch in this dual-source input case. For the UC, inductor L_1 , switch T_1 , and diode D_2 form a boost converter when transferring

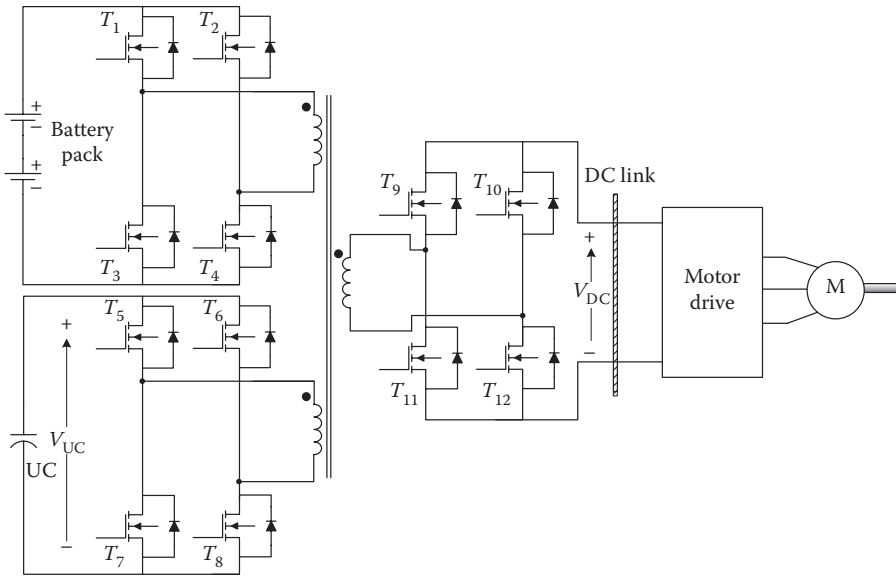


FIGURE 8.8 Dual-active-bridge converter topology with full-bridge converters.

power from battery to the DC link, and for the battery, inductor L_2 , switch T_3 , and D_1 – D_2 path form a boost converter when transferring power from UC to the DC link. During regenerative braking, the interface should be operated in buck mode. Switch T_2 , diode D_1 , and inductor L_1 form a buck converter from the DC link to the UC. On the other hand, some regenerative braking energy can be conveyed to the UC applying a pulse width modulation (PWM) signal to T_1 . In this case, switches T_2 and T_1 , diode D_3 , and inductor L_2 will form a buck converter from DC link to the UC. By applying an appropriate duty cycle to T_1 and T_2 , braking energy can be properly shared.

Although one switch is eliminated as compared to the multiple-converters configuration, a complicated control system is the main drawback of this configuration.

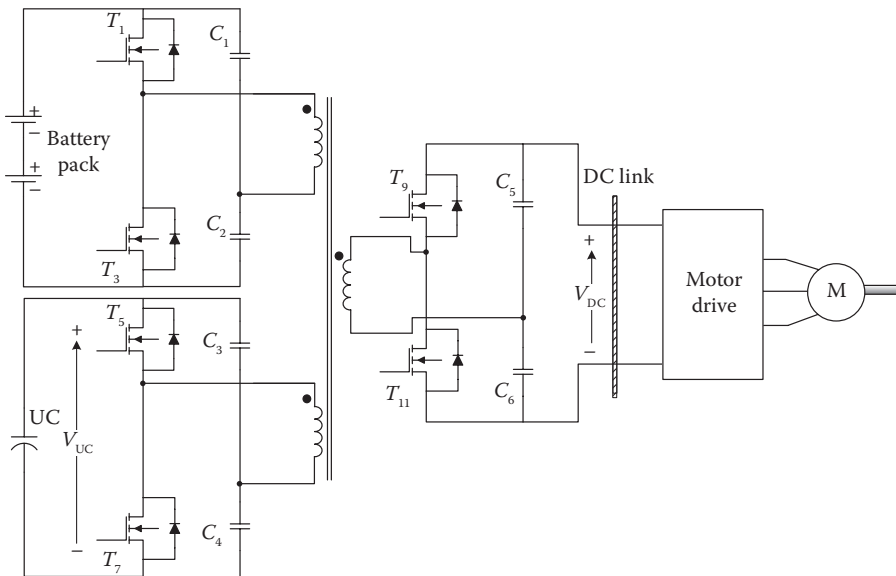


FIGURE 8.9 Dual-active-bridge converter topology with half-bridge converters.

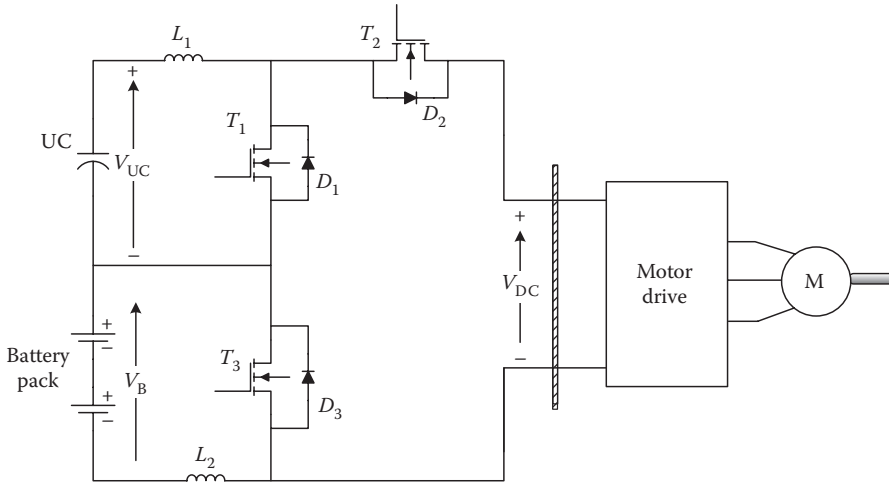


FIGURE 8.10 Dual-source bidirectional converters topology.

8.1.8 TOPOLOGY 8: MULTIPLE-INPUT CONVERTER CONFIGURATION

In the previously discussed topologies, battery and UC energy storage devices were employed through their individual DC/DC converters. Unlike these configurations, the multiple-input DC/DC converter has the flexibility of adding a number of inputs at the added cost of one switch and one diode (two switches and two diodes in the case of bidirectional operation). The multiple-input DC/DC converter topology with battery and UC input sources is given in Figure 8.11.

In this converter topology, the inputs share the same converter inductor and are connected through bidirectional switches [28–31]. This converter is capable of operating in buck, boost, and buck–boost modes for power flow in both directions. The assumption of a continuous inductor current requires that at least one input switch or diode is conducting at all times. The respective input diode is ON if all the input switches are OFF. If more than one switch is turned ON at the same time, the inductor voltage equals to the highest input voltage [32].

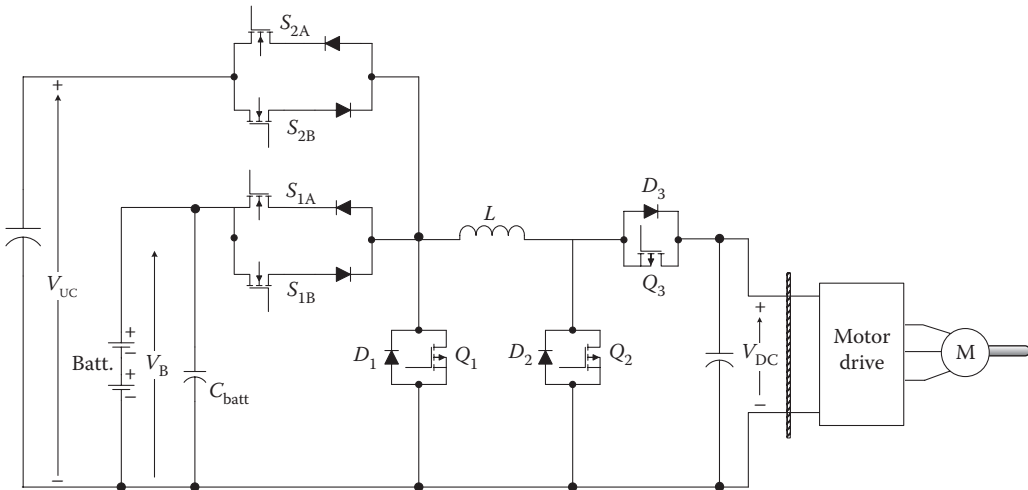


FIGURE 8.11 Multiple-input DC/DC converter topology.

Under acceleration conditions, both sources deliver power to the DC link. Since the UC voltage varies in a wider range than that of the battery, battery voltage can be selected higher than the UC for simpler operation. Since battery voltage is higher than that of the UC, S_{2A} is turned ON in boost mode. Switch Q_2 can be switched to control the inductor current, and power flow from battery to the UC can be controlled by switch S_{1A} . Diode D_3 conducts when Q_2 is turned OFF. During deceleration, the braking energy is transferred from the DC link to the energy storage devices and the converter is operated in buck mode. Since the UC voltage is less than the battery voltage, S_{1B} is always turned ON. Switch Q_3 can be used to control the inductor current. Power sharing between inputs is accomplished by controlling S_{2B} . Diode D_2 cannot conduct until switch Q_3 is turned OFF.

The main advantage of this topology is that only one inductor is required for the whole converter even if more inputs are connected, which can decrease the volume and weight of the converter significantly as compared to multiinductor or transformer topologies. Conversely, power budgeting in both boost and buck modes is very challenging and requires advanced control design.

8.1.9 TOPOLOGY 9: MULTIPLE MODES SINGLE-CONVERTER CONFIGURATION

In this design, only one bidirectional converter is required, with the UC voltage selected to be higher than the battery voltage. The UC is directly connected to the DC link to supply peak power demands, and the battery is connected to the DC bus through a diode. The bidirectional DC/DC converter is connected between the battery and UC, as shown in Figure 8.12, to transfer power between them [18]. This converter is controlled to maintain a higher voltage across the UC than the battery, and therefore, the diode is reverse biased for the majority of operations.

This converter has four different modes of operation: low-power mode, high-power mode, regenerative braking mode, and acceleration mode.

In low-power mode, it is assumed that the total power demand is less than the power capacity of the bidirectional converter. In this mode, since the UC/DC link voltage is higher than the battery voltage, the diode D_B is reverse biased. Since the power demand is lower than the capacity of the bidirectional converter, there is no power flow from the battery to the DC link. The battery supplies only power to the UC to keep its voltage at some predetermined higher level.

Whenever the power demand of the vehicle is greater than the converter power capacity, the system operates in high-power mode. In this mode, the UC voltage cannot be maintained at that high value since the power from the battery to the UC is less than the power from UC to the DC link. In this case, diode D_B is forward biased and the battery also directly supplies power to the DC link along with the UC.

During regenerative braking mode, since the UC is directly connected to the DC link, it is recharged by virtue of its position in the circuit, while diode D_B blocks the DC link power to prevent recharging of the battery directly. Some portion of the recaptured braking energy can be transferred to the battery through the bidirectional converter. Therefore, this mode provides controlled recharging for the battery; that is, whenever UC is fully charged but there is still regenerative energy available, the rest of the energy can be transferred to the battery as long as the regenerative current does

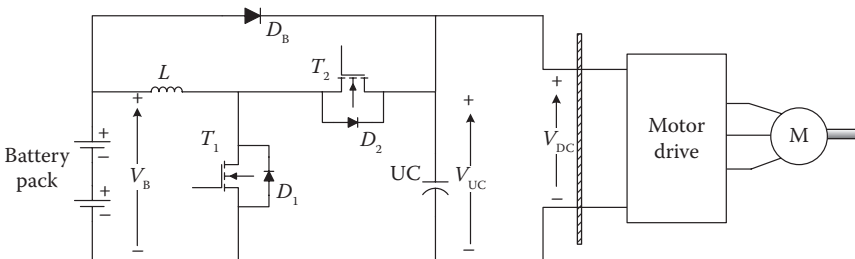


FIGURE 8.12 Single bidirectional converter topology.

not exceed the maximum battery-charging current. In the latter case, mechanical brakes could be utilized to keep the battery current below the maximum limit.

When the vehicle first starts to accelerate, the voltage across the UC is higher than that of the battery, and is equal to that of the DC link. Power demand on the vehicle is high, and UC voltage therefore drops. During the acceleration mode, the UC discharges through the DC link and the battery supplies power to the DC link through the bidirectional converter. Whenever the DC link voltage decreases to the level of the battery voltage, D_B becomes forward biased and the system switches to the high-power mode.

The advantage of this topology is that it requires only one converter. However, although power is shared among battery and UC during different modes, the battery current is not effectively controlled, especially in the regenerative mode with its potentially sharp transients.

8.1.10 TOPOLOGY 10: INTERLEAVED CONVERTER CONFIGURATION

The combination of battery and UC can also be achieved by using interleaved converters. The interleaved converter configuration is composed of a number of switching converters connected in parallel, as shown in Figure 8.13.

When low-current ripples or very tight tolerances are required, interleaved converters tend to be preferred. Interleaved converters offer very lower inductor current ripple than regular bidirectional converters, and the overall efficiency for a given power requirement is greater since each interleaved architecture has smaller power rating and smaller overall loss. Interleaved converters also have faster transient response to load changes [33–35].

As shown in Figure 8.13, the battery is interfaced to the UC terminals through the interleaved converters with UC directly connected to the DC link. Alternatively, UC and battery positions can be reversed, as shown by the dashed lines in Figure 8.13. In addition to these two configurations, the interleaved converters can be employed within topologies 2 through 5, presented in the earlier sections.

8.1.11 TOPOLOGY 11: SWITCHED CAPACITOR CONVERTER CONFIGURATION

Another bidirectional interface that combines battery and UC operation in PEVs, the switched capacitor converter (SCC), can also be employed [33]. An SCC is basically a combination of switches and capacitors, and by different combinations of switches and capacitors, these converters can produce an output voltage that is higher or lower than the input voltage. In addition, reverse polarity at the

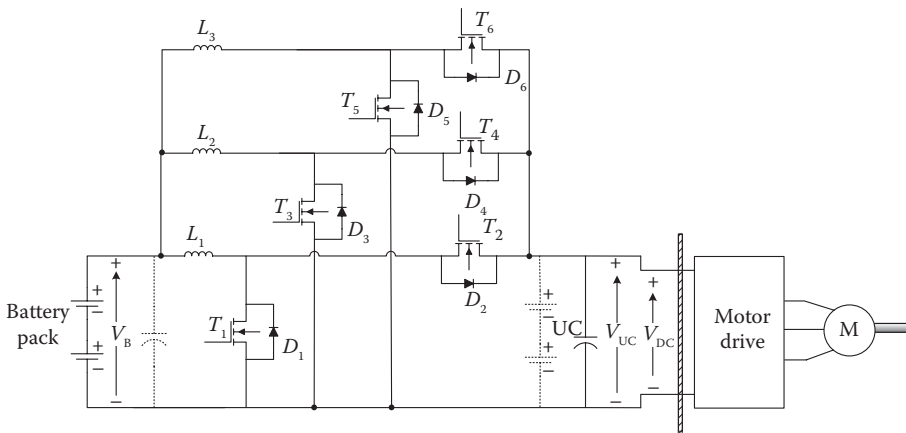


FIGURE 8.13 Parallel interleaved three-stage bidirectional converter.

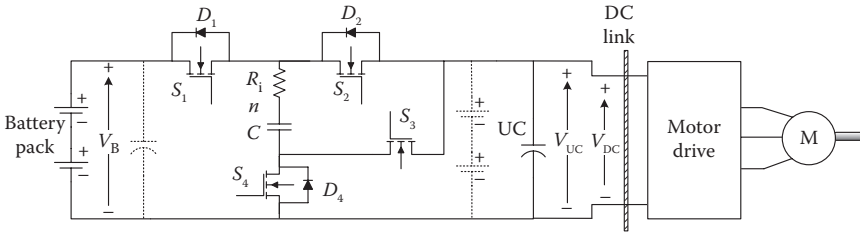


FIGURE 8.14 SCC configuration.

output can be provided if necessary. The capacitor can be charged or discharged through various paths formed by the controlled switches. Four switches, three diodes, and one switched capacitor can be used for a typical SCC. SCC can have a large voltage conversion ratio with very high efficiency, and therefore, they appear to be well suited for automotive applications [36–39].

An example of a battery/UC combination through SCC is provided in Figure 8.14.

On the basis of the circuit configuration shown in Figure 8.14, battery energy can be delivered to the load side by buck mode operation and the battery can be recharged by boost mode operation. In buck mode, switches S_1 and S_4 are turned ON until capacitor C is charged to some desired voltage level less than that of the battery, at which point, C is disconnected from the battery terminal by turning switches S_1 and S_4 OFF and connected to the load by turning switch S_2 ON to transfer its stored energy through S_2 and diode D_4 . In boost mode, C can be charged from the load side through D_2 and S_4 . After this stage, the S_3 and D_1 become the operating switches and the energy in C is discharged to the battery side. This control strategy offers control simplicity, continuous input current waveform in both modes of operation, and low source current ripple [33].

As shown in Figure 8.14, the battery is interfaced to the UC terminals through the SCC and the UC is directly connected to the DC link. Alternatively, UC and battery positions can be reversed, as shown by the dashed lines in Figure 8.14. In addition to these two configurations, the SCC can be employed within topologies 2 through 5, as a bidirectional converter, presented in the earlier sections.

8.1.12 TOPOLOGY 12: COUPLED INDUCTOR-BASED HYBRIDIZATION ARCHITECTURE

The system layout of this hybrid battery/UC architecture is demonstrated in Figure 8.15 [40]. The converter is composed of four switches T_1 – T_4 with their internal diodes D_1 – D_4 , battery and UC, a DC link capacitor C_1 , a capacitor in parallel with the battery (C_2), and an integrated magnetic structure with self-inductances L_1 , L_2 , and the mutual inductance M . The use of coupled inductors for the battery/UC combination can further reduce the bidirectional converters’ most bulky and expensive components.

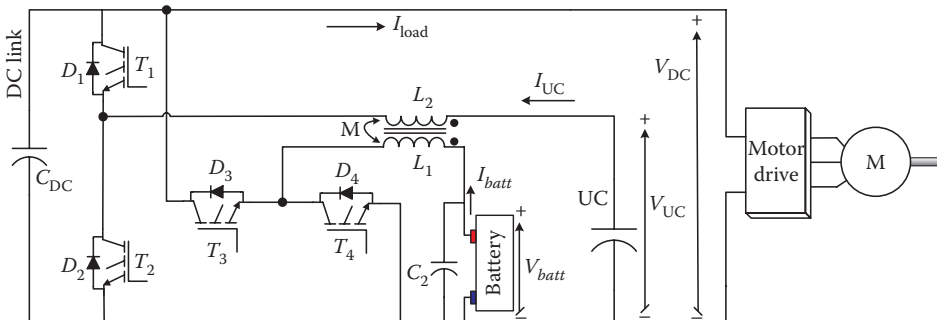


FIGURE 8.15 Coupled inductor-based battery/UC hybridization architecture.

This converter has five main operational modes: Mode-(1) Plug-in AC/DC charging of the energy storage devices with buck mode of operation from DC link voltage to the battery and UC. Mode-(2) Plug-in DC/AC discharging of the energy storage devices with boost mode of operation from the battery and UC to the DC link. Mode-(3) Boost mode of operation of the battery and UC to the DC link for acceleration, idling, or cruising during driving. Mode-(4) Buck mode of operation from DC link to the battery and UC for regenerative braking during driving. Mode-(5) Boost mode of operation and buck mode of operation when needed, that is, if the UC's SoC drops to the minimum allowed UC SoC. In plug-in charging, the power flow direction is identical to that of the regenerative braking mode. Therefore, Modes 1 and 4 are similar and the DC link acts as a common DC bus in these modes. Correlatively, when discharging energy storage devices in plug-in mode, power is transferred from ESS to the DC link with the same power flow direction in the acceleration mode. Therefore, Modes 2 and 3 are identical. Consequently, the operational modes can be generalized and the number of modes can be reduced to three.

In buck mode of operation for battery and UC, the vehicle can either be grid connected for charging or in regenerative braking condition. Switch T_3 , diode D_4 , and inductor L_1 form a buck converter from DC link to the battery. When T_3 is turned ON, current from DC link passes through T_3 and L_1 while energizing the inductor. When T_3 is turned OFF, D_4 is ON and the output current is freewheeled through D_4 and the inductance, decreasing the average current transferred to the battery. The current flow path of this operation mode is presented by blue lines in Figure 8.3. Similarly, the DC link voltage is stepped down to recharge the UC through the buck converter that is made up of switch T_1 , inductor L_2 , and diode D_2 . When T_1 is turned ON, power flows through T_1 and L_2 . When it is turned OFF, the energy stored in the inductor is freewheeled through D_2 . In boost mode of operation for battery and UC discharging, power is delivered from storage devices to the DC link, that is, plug-in discharging when grid connected or acceleration, cruising, and idling conditions during driving. The battery voltage can be boosted to the DC link by the inductor L_1 , switch T_4 , and diode D_3 that form a step-up converter. When T_4 is turned ON, the battery terminals are shorted through T_4 and L_1 , while energizing the inductor. When T_4 is turned OFF, D_3 turns ON and the energy is stored in the inductor, and the battery is transferred through D_4 to the DC link. Similar to the battery discharging, inductor L_2 , switch T_2 , and diode D_1 make up a boost converter from the UC to the DC link. When T_2 is turned ON, the inductor L_2 is energized and the UC discharges. When T_2 is turned OFF, D_1 turns ON and the energy stored in the inductor and the UC power flows through D_1 to the DC link.

The final operation mode is utilized when the battery is in boost mode and UC is in buck mode. It is very unlikely that the UC SoC drops below the minimum allowed value, since UC gains energy transiently when the load level decreases or a regenerative braking occurs. Therefore, this mode of operation is included as a fail-safe measure. If by any chance, the UC SoC drops to its minimum limit, the battery supplies power to the DC link while the UC retrieves power from the DC link. In this way, both the load demand is met and the UC is recharged by the battery. Whenever a regenerative braking occurs, the UC captures the available braking energy and this mode gets terminated. This mode will naturally end when the UC's SoC increases above the minimum limit. Table 8.1 summarizes all the operation modes of the proposed system.

TABLE 8.1
Operation Modes of the Proposed Battery/UC Converter

Mode	Source	Load	Operation
1 and 4	Grid and regenerative braking	Battery and UC	Buck for battery and buck for UC
2 and 3	Battery and UC	Grid and propulsion	Boost for battery and boost for UC
5	Battery	Propulsion and UC	Boost for battery and buck for UC

8.2 OTHER ENERGY STORAGE DEVICES AND SYSTEMS: FLYWHEELS, COMPRESSED AIR STORAGE SYSTEMS, AND SUPERCONDUCTING MAGNETIC STORAGE SYSTEMS

As an alternative to the battery/UC hybrid ESS, flywheels, compressed air storage systems, and superconducting magnetic storage systems can be incorporated within plug-in hybrid EVs. Although these ESS are still being investigated and currently, there are only research-level applications, they may be applicable to the plug-in hybrid EVs when they are commercialized due to the characteristics discussed in the following sections.

8.2.1 FLYWHEEL ESS

Unlike batteries and UCs, a flywheel stores energy in a kinetic device rather than in an electrochemical or electrostatic device. A flywheel designed for an energy storage application is basically a large rotating disk with a very high moment of inertia, designed to spin at very high speeds—from 20,000 to 50,000 rpm. Stored kinetic energy can be converted into electricity, or electricity can be converted into kinetic energy. A motor/generator is typically coupled to the flywheel, or the flywheel rotor itself is used as the motor/generator rotor, to convert kinetic energy into electric energy or electric energy into kinetic energy. In motoring mode, the electric machine increases the stored kinetic energy within the flywheel by simply increasing its speed, and in generating mode, the electric machine's shaft is mechanically driven by the flywheel, sapping energy [41]. Whenever power is drawn through the generator by the electrical system of the vehicle, it extracts energy from the flywheel by decreasing its rotational speed, and whenever excess needs to be dumped into the storage medium, its speed is increased. To increase the energy storage capacity in a flywheel system, the moment of inertia (a physical characteristic related to mass and geometry), or the maximum rated speed of rotation may be increased. Owing to their smaller size and the fact that stored energy increases as the square of rotational speed, high-speed flywheels are more preferable for automotive applications than the low-speed flywheels. However, high-speed flywheels must be isolated in a vacuum to reduce the windage and ventilation losses, and mechanical bearings—the other mode of energy losses in a flywheel system—should be replaced with contactless magnetic bearings so that the system floats on a “cushion” of electromagnetic force. These bearings are still being researched as practical replacements for mechanical bearings as a means to reduce the friction losses [42].

As is the case with other energy storage devices, safety is a concern that must be addressed when using flywheels. Since flywheels are high-speed devices, containment vessels are used in case of mechanical rotor failures, and flywheels are inherently designed to fail in some manner other than by flying apart. The other drawbacks are that they are relatively large, and heavy systems and rotational energy losses limit the long-term storage capabilities. Although size can be reduced as the speed is increased (with a maximum of about 1,00,000 rpm), this option would also increase the rotational losses and self-discharge (slowing down).

The advantages of flywheel storage devices are that they have a long rated life (typically 20 years [43]), can deliver large amounts of energy in a very short time, and are free of the deep discharge and high cycle count issues that tend to plague batteries. The power that can be delivered to/from a flywheel is limited only by the electric machine that is mechanically connected to it. Flywheels have been considered for large vehicles such as buses, trucks, and high-speed rail locomotives where the battery costs are inherently high [41]. A schematic example of the implementation of a flywheel ESS is shown in Figure 8.16.

In Figure 8.16, the electrical energy storage devices are shown in a generalized form that can be the representation of any of the hybridization topologies discussed earlier, and with the addition of a flywheel, it may be possible to include only one of these electrical storage systems into a design. Since the vehicle provides a common DC link, the flywheel can be connected to this DC link through a bidirectional DC/AC converter and a high-speed electric machine. Whenever there

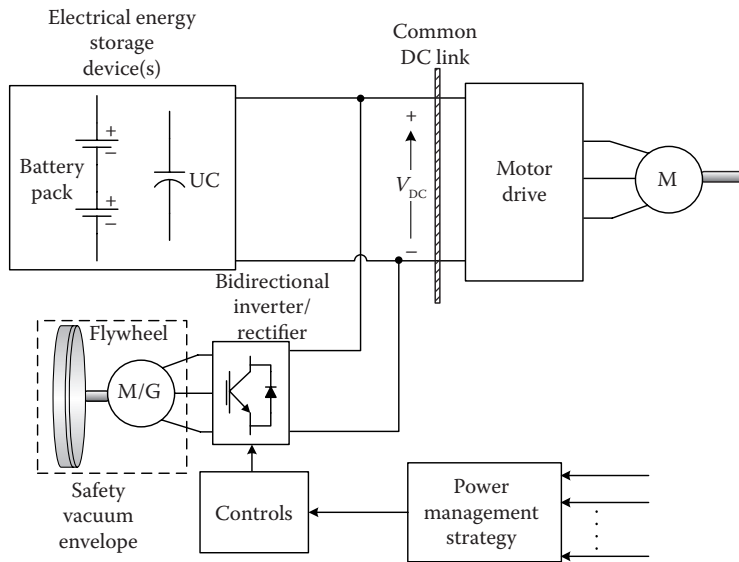


FIGURE 8.16 Hybrid flywheel ESS.

is a surplus of braking or buffering energy, it can be delivered to the flywheel by operating the machine in motoring mode and the converter in inverter mode, and whenever the energy stored in the flywheel is needed for propulsion, the machine is operated in generator mode and the converter is operated in rectifier mode [43–46]. Permanent magnet synchronous machines are typically preferred to drive flywheels due to their high-speed operation capability and control and drive simplicity [47]. The inputs to the power management strategy can be simply flywheel speed, torque demand on the vehicle, engine power, and power from electrical energy storage devices. From these variables, the power from/to flywheel can be controlled accordingly.

As an alternative to this electrical connection of flywheels through a power electronic converter and an electric machine, flywheels can also be mechanically coupled to the traction drive. However, in this mechanical case, they cannot be actively controlled to deliver or capture a certain amount of power; instead, they would only help torque-ripple cancelation as a passive flywheel [48].

8.2.2 COMPRESSED AIR-PUMPED HYDRAULICS-BASED STORAGE SYSTEM

Compressed air or pump storage devices may also be promising candidates for future energy storage solutions in PEVs. These storage alternatives have a much longer lifetime than batteries, typically 75 years for pumped hydro and 40 years for compressed air cases [49], and have comparable efficiency ratings of around 75%–80%. In addition to the high efficiency and long lifetime, they are more environmentally friendly as they do not produce problematic waste materials. Compressed air and pump storage device sizes vary greatly and can be implemented in both ultra-large facilities [50] and small applications using mechanical/hydraulic conversion with the liquid piston technique [49]. A simple implementation of a compressed air storage system for PEVs is given in Figure 8.17.

The compressed air-based potential energy storage devices can be interfaced to the common DC link through a motor/generator and a bidirectional DC/AC–AC/DC converter. Electrochemical storage devices such as batteries and UCs can still be employed within the vehicular power system, but since the compressed air storage system offers high-energy capacity and density, it could replace the batteries entirely. However, a storage device with higher power density and faster response, that is, UCs, is still needed for situations involving hard braking and quick acceleration. During the energy

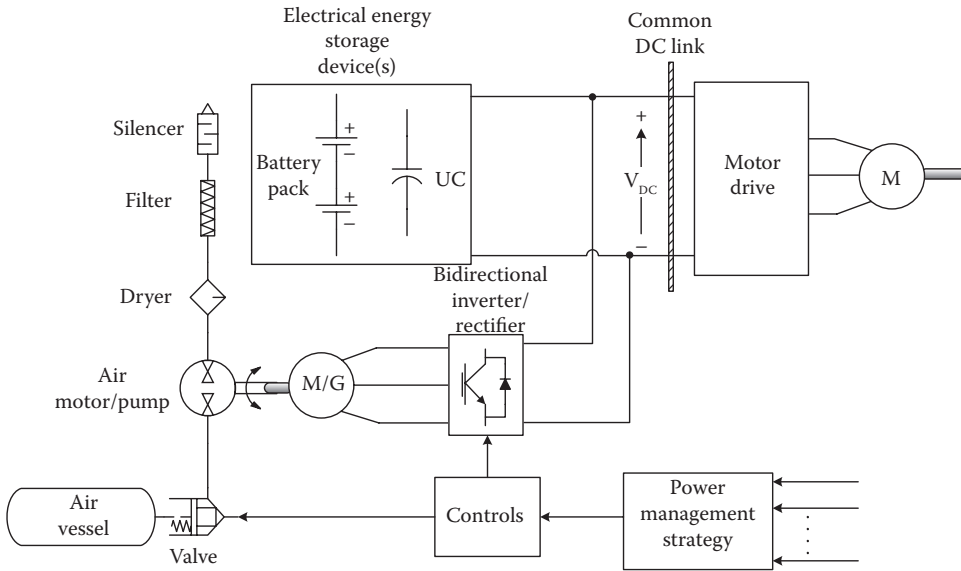


FIGURE 8.17 Compressed air storage system implementation.

storage process, the converter is operated in inverter mode and the electric machine is operated as a motor. The motor drives a pneumatic air pump that operates as a compressor and fills the vessel with pressurized air.

Whenever power is needed from the compressed air storage system, the converter is operated in rectifier mode and the electric machine is operated as a generator. In this mode, the pneumatic machine is driven directly by the compressed air that expands and is released from the air vessel. The pneumatic machine then drives a generator and power is supplied to the DC link via the power electronic converter. The power electronic converter and the valve of the air vessel are controlled based on the mode of operation and the amount of power that is to be delivered to/from compressed air storage system.

The main drawback of the pneumatic storage system is its low efficiency when compared to hydraulics-based storage systems. This is mainly due to the inefficiency of the compressor motor/pump. Therefore, oil-hydraulics/pneumatics-based ESS can be implemented to achieve higher efficiency and energy-density levels [49,51,52]. Hydraulic motors have exceptionally high-energy conversion efficiency and can achieve higher energy densities in storage applications due to their high-pressure ratings. These systems employ piston vessels or a high-pressure bladder where nitrogen is compressed by injecting high-pressure fluid (oil) in the body or in the shell using a piston or membrane as a gas/liquid separation medium. Combining gas pressurizing (pneumatics) and fluid compression (hydraulics), one produces a hydro-pneumatic storage system [49]. The operating principle of the hydro-pneumatic storage system for a PEV is provided in Figure 8.18.

The hydro-pneumatic system operating principle is very similar to that of the compressed air storage system. The major difference is that the hydraulic pump/motor, to compress the nitrogen gas, pumps oil rather than directly pressurizing the air. The most significant challenge with the compressed liquid/air systems is the relatively large size and the high number of components involved. This increases the cost and reduces the overall efficiency in vehicular applications.

8.2.3 SUPERCONDUCTING MAGNETIC ESS

Superconducting magnetic energy storage systems (SMES) can store electric energy in the form of magnetic energy. SMES are capable of transferring large amounts of power quickly in both charge

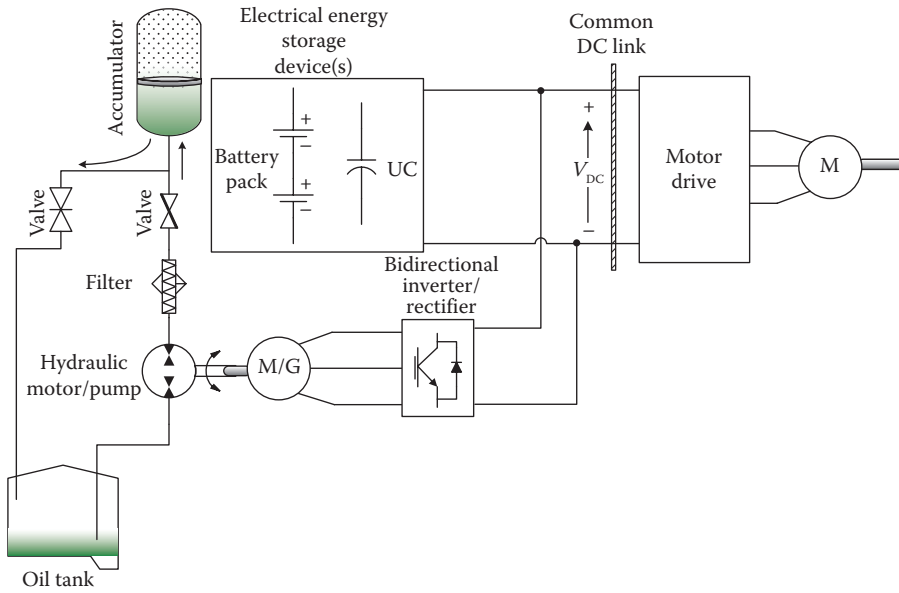


FIGURE 8.18 Hydro-pneumatic ESS implementation.

and discharge directions, and their efficiency is very high with a charge–discharge efficiency of over 95% [53]. Moreover, a relatively small magnet can be employed. Although the power density is high but the energy density is not very high, the battery energy storage devices cannot be completely eliminated in most of the cases. However, SMES can offer a suitable replacement for UCs.

As in battery/UC combined operation, battery/SMES combinations also provide high-power and high-energy density without any rotating parts [54–56]. Since batteries are still the main energy storage device, the size and cost of the SMES can be kept relatively low and this hybrid ESS can be made applicable to plug-in vehicles. Longer life and higher efficiency are the other advantages of hybrid battery/SMES system. As stated in Reference 57, when subjected to fast transients and repeated charge–discharge pulses, batteries present technical problems such as reduced efficiency, degradation, and overheating. Although UCs can mitigate these problems by providing energy during fast, high-demand transients, their energy density is very low and they are not a practical choice as the sole energy storage device for a PEV. With proper design, SMES may replace both batteries and UCs [57]. However, SMES devices present the major drawback of needing to be operated at very low temperatures for their coils to act as a superconducting material and reduce ohmic losses. For refrigeration and device containment, a cryogenic system must be constructed, the complexity and refrigeration power of which reduces the overall system efficiency and ease of implementation, and is a serious drawback to the commercial viability of vehicle-scale SMES systems. This refrigeration energy can be obtained through a closed-cycle system, that is, cryocooling, or cooling can be provided through evaporation of a suitable cryogenic liquid such as helium, nitrogen, or neon [57], and for vehicular applications, these are serious challenges that prevent the use of SMES. The use of high-temperature superconductors would make the SMES cost-effective and more efficient due to the reductions in refrigeration needs, but high-temperature superconducting material developments are still in the research and development stages [58,59].

To achieve the best possible performance with least cost, several factors should be considered for the design of SMES systems with coil configuration, structure, operating temperature, and energy and power capabilities being some of these key factors [58,60]. Energy/mass ratio, Lorentz forces (the force due to the electromagnetic field), and stray magnetic field are the parameters between which a compromise must be made for a stable, reliable, and economic SMES system. The SMES

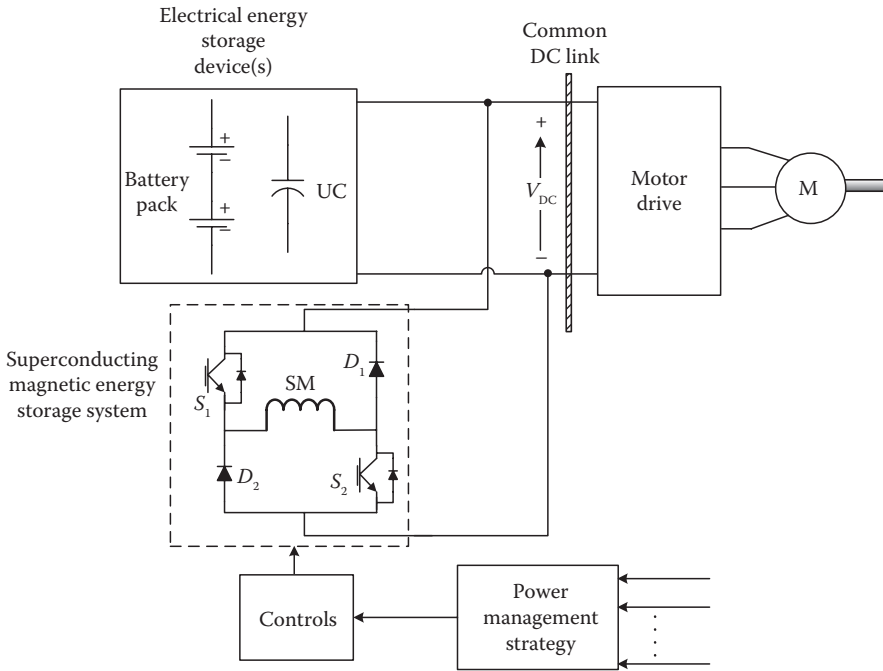


FIGURE 8.19 SMES implementation for a PEV.

coil can be toroidal or solenoidal; the solenoid coil type is preferred due to its simplicity and manufacturing cost-effectiveness, although toroids may be more suitable for small-scale applications [53]. Inductance wiring and the rating of the power electronic converter limit the maximum power (voltage and current) that can be drawn or injected from/to SMES system.

A typical implementation of an SMES to PEVs is shown in Figure 8.19. Although the battery and UC are shown in the system, UCs can be eliminated as mentioned earlier. In this configuration, a power electronic converter is used for SMES utilization.

During charging, switches S_1 and S_2 are turned ON allowing positive current to flow and increasing the voltage of the superconducting magnet, storing energy. By keeping S_1 turned ON and S_2 OFF, the energy stored in the magnet will circulate through S_1 –SM– D_1 , shorting the SM. Since it is composed of a superconducting material, energy can be stored by circulating the current through this path with only the circuit losses being those caused by the internal resistances of the switch and diode. During discharging mode, both switches, S_1 and S_2 , are turned OFF and the diodes become forward biased such that stored energy is transferred to the DC link. During discharge, it is possible to stop the flow of energy and switch back to the energy storage mode by keeping S_1 OFF and turning S_2 ON. In this case, the current of the superconducting magnet will circulate through the path SM– S_2 – D_2 and no energy transfer will occur since the SM is shorted through its own terminals.

The other drawback to the practical implementation of an SMES system is that, although the coil is superconducting, the switches are not ideal; therefore, the charge/discharge current will gradually decrease due to semiconductor losses in energy-storing mode. By using switches with low internal resistances and applying soft switching or switching loss recovery techniques, higher efficiencies can be achieved, but parasitic losses can never be completely eliminated.

8.3 CONCLUSIONS

In this chapter, different topologies offering the combined operation of several ESS have been reviewed. In total, 12 possible hybridization topologies are described for the combined operation of

batteries and UCs. The advantages and drawbacks of the passive parallel connection, UC/battery, battery/UC, cascaded converters, parallel converters, multiinput converters, dual-active-bridge converters, dual-source converters, interleaved converters, and SCC have all been highlighted. In addition, kinetic, potential, and magnetic ESS such as flywheels, compressed air/pumped hydraulics, and SMES devices have been described along with possible implementation scenarios, including advantages and disadvantages for plug-in hybrid EVs. Although there is no commercially manufactured plug-in hybrid vehicle powered by batteries and UCs together in the market so far, the hybridization of these energy storage devices has shown to be academically and analytically very beneficial in terms of battery life, vehicle performance, and fuel economy. However, the hybridization of energy storage devices is a challenging, multivariable problem requiring appropriate sizing and control of power-sharing strategies. Furthermore, nontraditional forms of ESS can be promising candidates for plug-in hybrid EVs due their longer lifetime, efficiency, and high specific power and energy densities, and further research and development of these technologies may produce some unforeseen ideal combination of energy density, power availability, efficiency, and easy if implemented in the future.

8.4 SIMULATIONS AND ANALYSES OF HYBRID ESS TOPOLOGIES FOR PEVs

In this section, three examples of hybridization topologies for the combined operation of batteries and UCs have been modeled and simulated. First, the passive parallel configuration topology is simulated; second, battery/UC cascaded and connected converters topology; and third, the parallel connected multiconverters configuration, making a case for the effectiveness and feasibility of each topology through the discussion that follows.

For the simulations, a portion of the urban dynamometer-driving schedule (UDDS) is used for the time interval $t = [690, 760]$. This driving cycle period of 80 s includes acceleration, braking, and idling conditions for the vehicle. For the analysis, a plug-in version of Toyota Prius has been used, and the battery parameters of the Toyota Prius plug-in are given in Table 8.2 [61,62].

For the UC, a BMOD0165 UC module manufactured by Maxwell has been chosen, the parameters of which are given in Table 8.3 [63].

Since one of the test topologies calls for a passive parallel connection, the UC voltage should be chosen such that it is close to that of the battery. Therefore, seven BMOD0165 modules are

TABLE 8.2
Toyota Prius PEV Battery Parameters

Parameter	Value
Battery type	Lithium ion
Rated voltage	345.6 V
Rated energy capacity	5.2 kWh
Rated Coulomb capacity	15.04 Ah
Internal resistance	0.56104 Ω

TABLE 8.3
Maxwell BMOD0165 UC Parameters

Parameter	Value
Nominal capacitance	165 F
Rated voltage	48.6 V
Equivalent series resistance	6.3 m Ω
Peak current	1970 A

connected in series, resulting in 23.57 F capacitance, 340.2 V rated terminal voltage, and 44.1 mΩ of internal series resistance.

8.4.1 SIMULATION AND ANALYSIS OF PASSIVE PARALLEL CONFIGURATION

In this configuration, the battery and UC are connected directly in parallel without any interfacing converter in between, and the common battery/UC terminals are connected to the DC link through a bidirectional converter. The power demand for the vehicle has been obtained through powertrain system analysis toolkit (PSAT) simulations considering a typical mid-size sedan vehicle configured as a PEV. Since the motor drive voltage is almost constant, the power demand of the vehicle can be divided by the DC link voltage to obtain the motor drive current, and the motor drive and load demand variation have therefore been modeled and implemented as a controlled current source.

During the simulation, the reference DC link voltage was selected as 400 V and the bidirectional converter was controlled through a double-loop voltage and current controller. A proportional–integral (PI) controller was used in the voltage loop, while a peak current mode controller was used in the current loop, as shown in Figure 8.20.

The load current for the $t = [690, 760]$ time interval varies, as shown in Figure 8.21. As shown, this load current includes positive and negative current variations, simulating acceleration, and braking conditions. On the basis of this load current variation, the bidirectional converter is controlled such that it maintains a constant DC link voltage while supplying power from sources during acceleration, and recharging them during braking. The battery and UC current variations are given in Figures 8.22 and 8.23, respectively.

As shown in Figures 8.22 and 8.23, the battery inherently supplies a smoother current profile in comparison to the UC due to its slower dynamics. However, since there is no interface that controls the battery current, its current has some fluctuations that could likely be eliminated by other connection

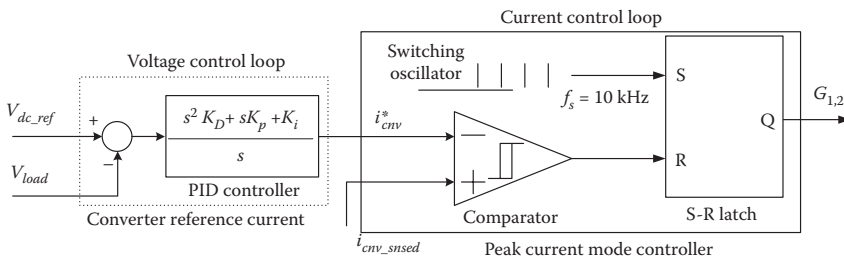


FIGURE 8.20 Control system for the passive parallel connection topology.

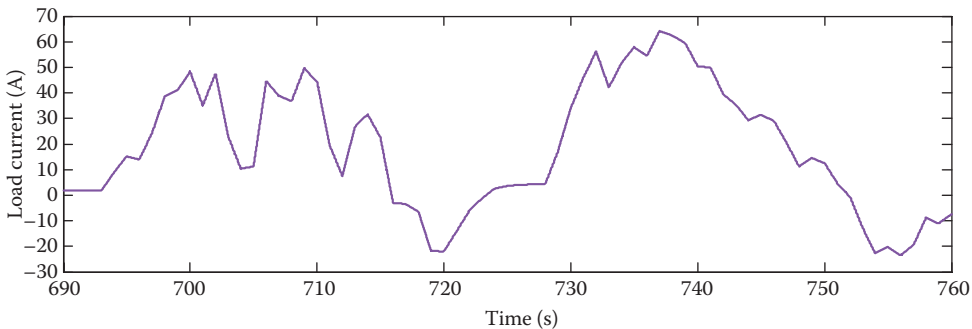


FIGURE 8.21 Load current variation.

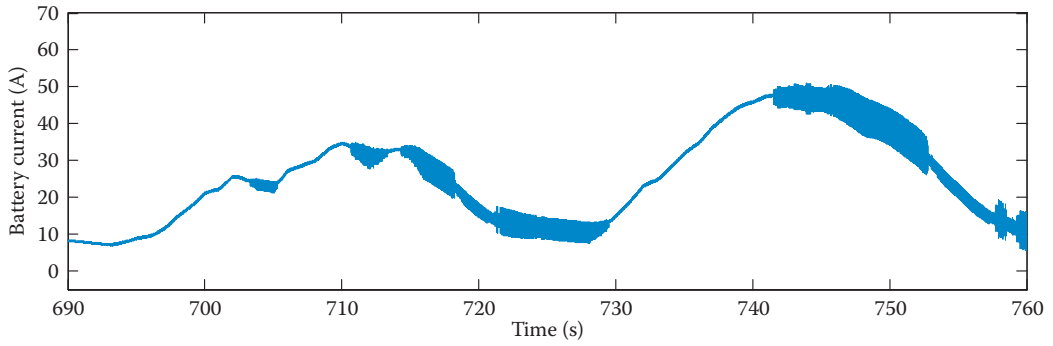


FIGURE 8.22 Battery current variation in passive parallel topology.

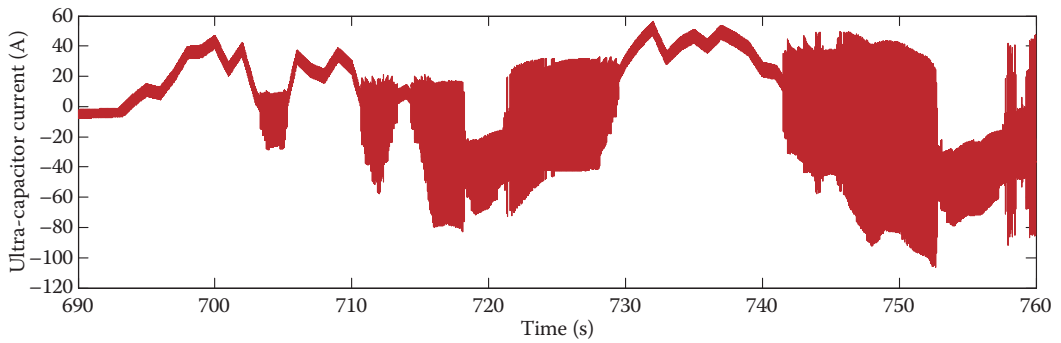


FIGURE 8.23 UC current variation in passive parallel topology.

topologies. Owing to the voltage balance between the battery and UC, battery current varies automatically to maintain similar terminal voltage with the UC at all times. If the UC voltage was higher than the battery voltage due to some large braking energy recovery, the battery current would reverse direction, but here, only the UC receives power from the application of regenerative braking.

The SoC variations of the battery and UC are given in Figures 8.24 and 8.25, respectively.

The initial SoCs for both battery and UC were selected as 90%. Since the battery voltage is higher than the UC, the battery is always discharging as explained for the current variations. However, the SoC of the UC is sometimes increasing as it is recharged during braking conditions, that is, the negative current variations of the UC.

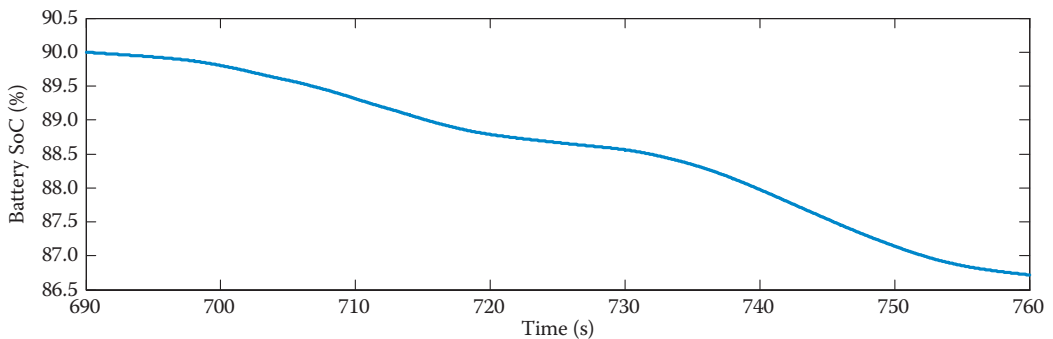


FIGURE 8.24 SoC of the battery for passive parallel topology.

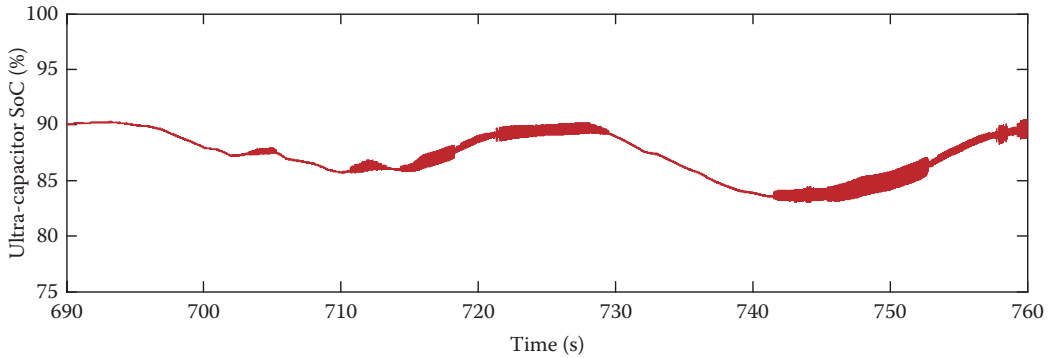


FIGURE 8.25 SoC of the UC for passive parallel topology.

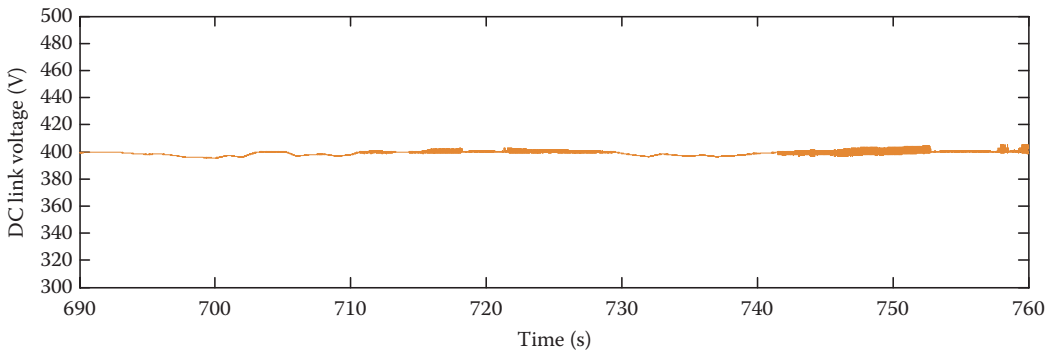


FIGURE 8.26 DC link (load bus) voltage variation for passive parallel topology.

Finally, the DC link voltage variation, to which the motor drive inverter is connected, is given in Figure 8.26. As observed from Figure 8.26, the DC link voltage varies steadily around the 400-V reference set point. During high-power demands and operation mode changes of the bidirectional converter, the voltage fluctuations increase. For this topology and control strategy, the maximum voltage seen at the DC link is 405.3 V with a minimum of 395.2 V, and therefore, a maximum amplitude of the voltage fluctuation of 2.5% over the simulation period.

8.4.2 SIMULATIONS AND ANALYSIS OF CASCADED CONVERTERS TOPOLOGY

In this configuration, the battery is connected to the UC through a bidirectional converter and the UC is connected to the DC link through another bidirectional converter; therefore, the battery, converter 1, UC, and converter 2 are all in cascade connection. The same drive cycle over the same time interval was used for load modeling in this topology as in the previous simulation, with the DC link voltage reference kept at 400 V. For the UC controls, a double-loop controller is employed for DC link voltage regulation, and for the battery controls, only a peak current mode controller is used. The reference current for the battery can be obtained as

$$I_{batt}^* = \frac{V_{load} \cdot I_{load}}{V_{batt}} G_{LP}(s) \quad (8.1)$$

where I_{batt}^* is the battery reference current, V_{load} and I_{load} are the instantaneously measured DC link voltage and current, and V_{batt} is the battery terminal voltage, which is nearly constant during the whole drive cycle. The transfer function represented by $G_{LP}(s)$ is a low-pass Bessel filter that is applied to eliminate any spikes and fast transients from the battery reference current. These fast transients come

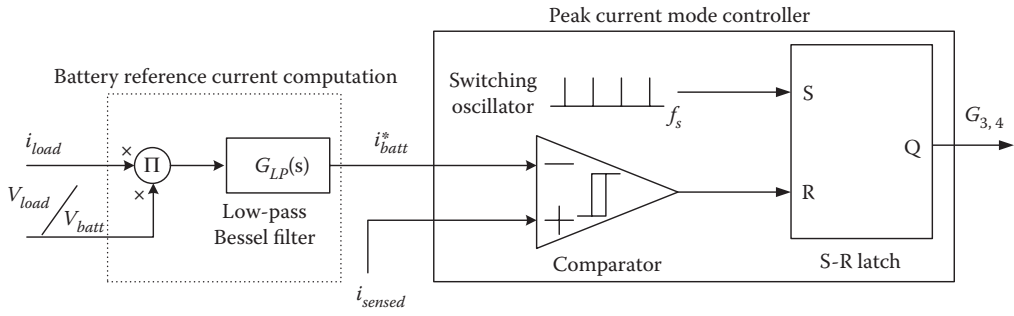


FIGURE 8.27 Battery current controller.

inherently from the variation in instantaneously measured load current, and by employing this filter, the battery current can be smoother and the stress on the battery is reduced since there is an additional converter regulating the battery current. The battery current controller is depicted in Figure 8.27.

The load current drawn from the DC link varies in the same manner as shown in Figure 8.21, and vehicle specifications and battery and UC parameters are the same as in the previous example. On the basis of this load current variation, the UC’s bidirectional converter is controlled such that it maintains a constant DC link voltage. The bidirectional converter connected to the battery is controlled so that the battery supplies the average load demand to the converter’s output. Whenever the DC link sees a reference voltage >400 V, both converters are controlled to change their modes of operation from boost to buck so that the braking energy can be recovered back into the storage devices. The battery and UC current variations are given in Figures 8.28 and 8.29, respectively.

From Figures 8.28 and 8.29, the battery current ripples are reduced due to the control strategy employed. Moreover, the power contribution is greater as compared to the previous topology since the battery current is actively controlled, allowing it to slowly supply the actual load demands. A benefit of this configuration is that, at any time, a limitation can be placed on the maximum allowable battery current to reduce the battery contribution and allow the UC to supply more power to the DC link to maintain the 400-V regulation. In this topology, the current ripple of the UC is greater than in the simpler passive parallel connection, but since it can successfully supply these current variations without seeing a shorter life span, this is not an issue for the UC.

The SoC variations of the battery and UC are given in Figures 8.30 and 8.31, respectively.

In this configuration, the battery is utilized in a manner similar to the passive parallel case. Therefore, the SoC usage window for the UC is smaller since it continually receives charge from the battery. However, since the battery contributes more, its SoC decreases more quickly in comparison to the passive parallel case.

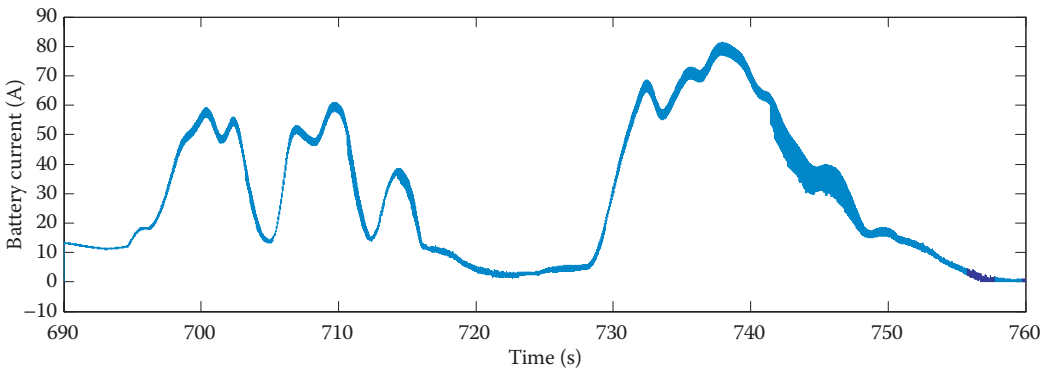


FIGURE 8.28 Battery current variation in cascaded converters topology.

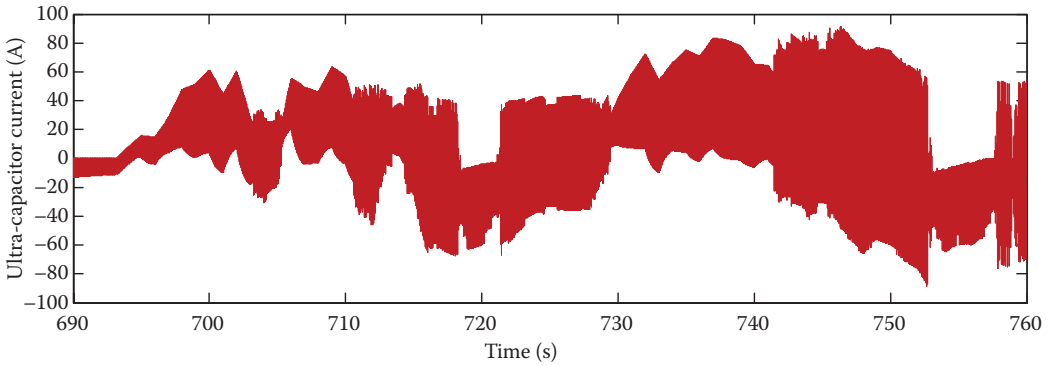


FIGURE 8.29 UC current variation in cascaded converters topology.

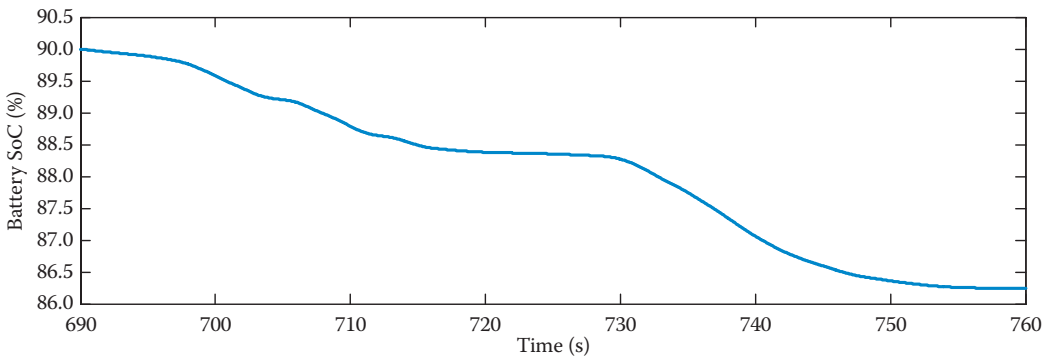


FIGURE 8.30 SoC of the battery for cascaded converters topology.

The DC link voltage variation for the cascaded converters configuration is represented in Figure 8.32. As seen from the figure, the DC link voltage varies around the 400-V reference set point, and during high-power demands and operation mode changes of the bidirectional converters, voltage fluctuations become more apparent. For this topology and control strategy, the DC link voltage reaches a maximum of 405.0 V and a minimum of 395.3 V. Therefore, the maximum amplitude of the voltage fluctuation has been calculated as 2.4% over the simulation period.

Since this configuration employs an individual DC/DC converter for the battery, it has the built-in flexibility of tuning and manipulating battery current controls. Therefore, a rate limiter and a saturation limiter can be implemented within the battery current control loop: the rate limiter will

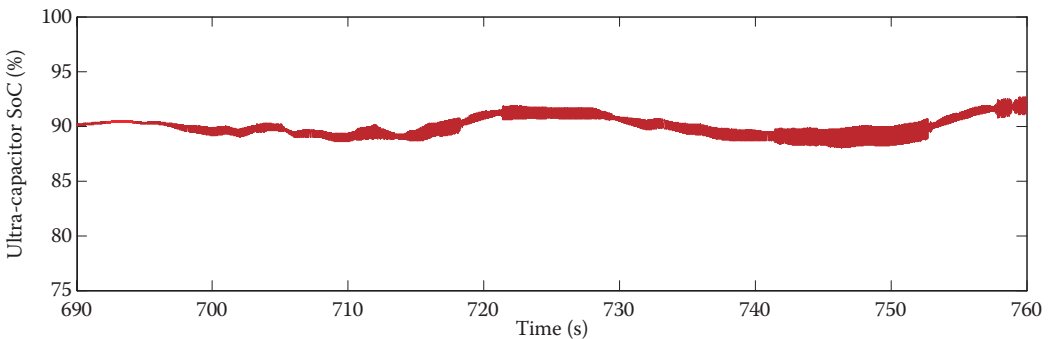


FIGURE 8.31 SoC of the UC for cascaded converters topology.

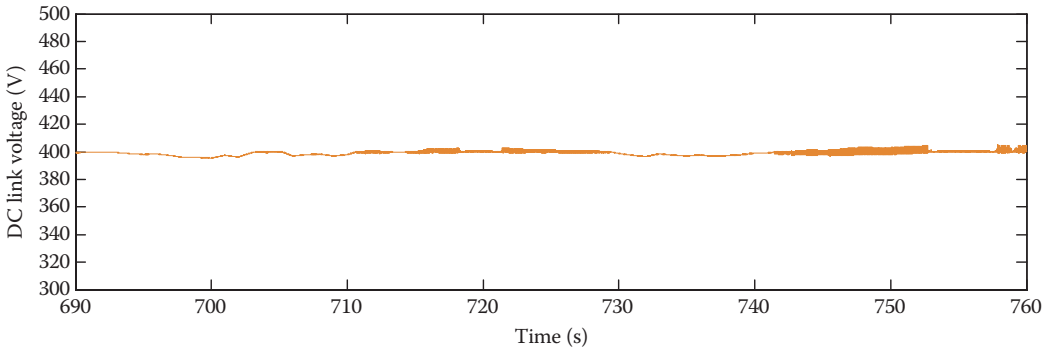


FIGURE 8.32 DC link (load bus) voltage variation for the cascaded converters topology.

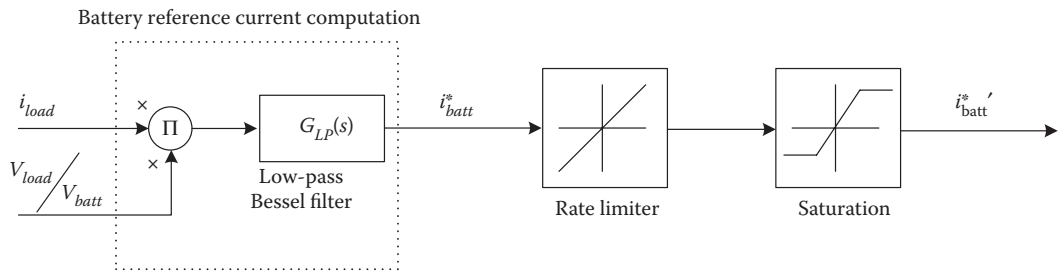


FIGURE 8.33 Battery reference current manipulation.

limit the slope of the battery reference current, while the saturation limiter will limit the battery current magnitude. The implementation of rate and saturation limiters into the battery controller is shown in Figure 8.33.

The rate limiter applied here has a rising slew rate of +0.1 and a falling slew rate of -0.1 placed on the rising and falling rates of the battery current. At the same time, the saturation block limits the maximum battery reference current by +50 A and negative battery reference current by -50 A to ensure the further reduction of battery stress and maximum battery charge and discharge current. In this case, the current variations of the battery and UC are recorded as given in Figures 8.34 and 8.35.

The battery current given in Figure 8.34 resulted from implementation of the rate and saturation limiters within the battery current control loop. This modification improves the battery current

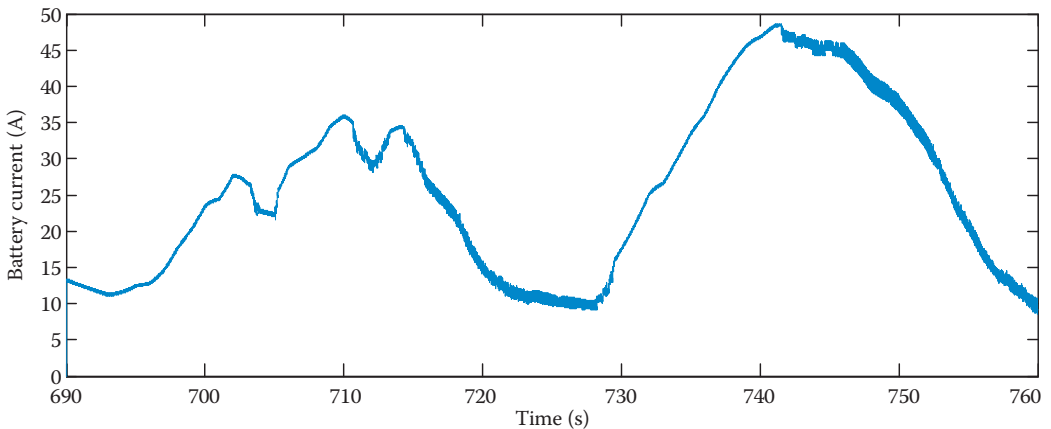


FIGURE 8.34 Battery current variation with modified controls.

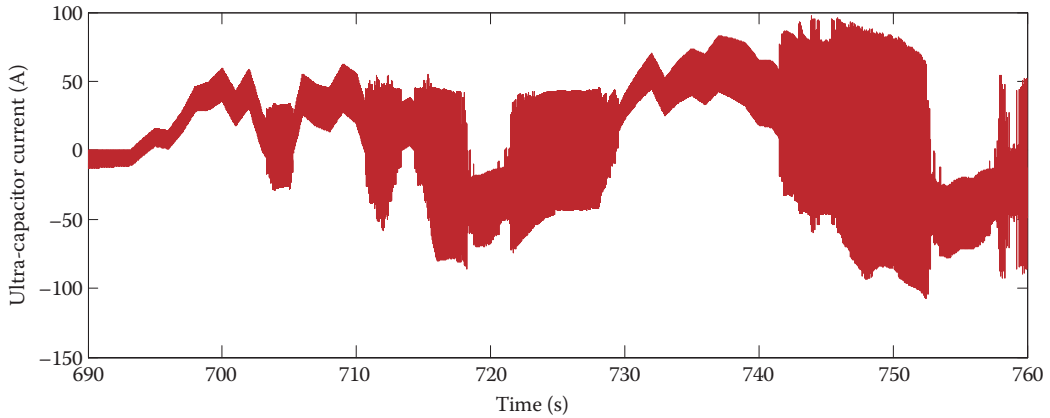


FIGURE 8.35 UC current variation with modified controls of battery.

waveform by eliminating the natural high slew rates of the load current (see Figure 8.28 vs. Figure 8.34). Moreover, maximum charge and discharge current rates can be defined and battery protection can be realized. In this case, the UC tends to vary faster in time and larger in amplitude (see Figure 8.29 vs. Figure 8.35), but again, the selected UC should be capable of supplying this type of current demand. Since the battery usage is reduced and more power is supplied from the UC, the modified current controller affects the SoC variations, as shown in Figures 8.36 and 8.37.

Figures 8.36 and 8.37 show that the battery SoC remains higher (see and compare Figure 8.30) while UC SoC drops more drastically (see and compare Figure 8.31) since the battery response to power-throughput demands is reduced and the UC must deliver more power to the DC link to regulate its voltage during transients.

While using any of the topologies discussed, whenever the UC SoC falls below a certain point, the battery controller should bring it above a certain point while supplying the load demands at the same time. A typical lower limit for the UC can be selected as 20%. Although a deep discharge does not tend to be a problem for UCs, such a limitation would prevent the associated DC/DC converter from operating in extreme voltage conversion ratios. Moreover, a fully discharged UC would draw an excessive high current at the initial charging if the charge current is not appropriately controlled.

The DC link voltage for this topology with a modification allowing for current limiting of battery is presented in Figure 8.38. Since the UC supplies more power to maintain constant DC link

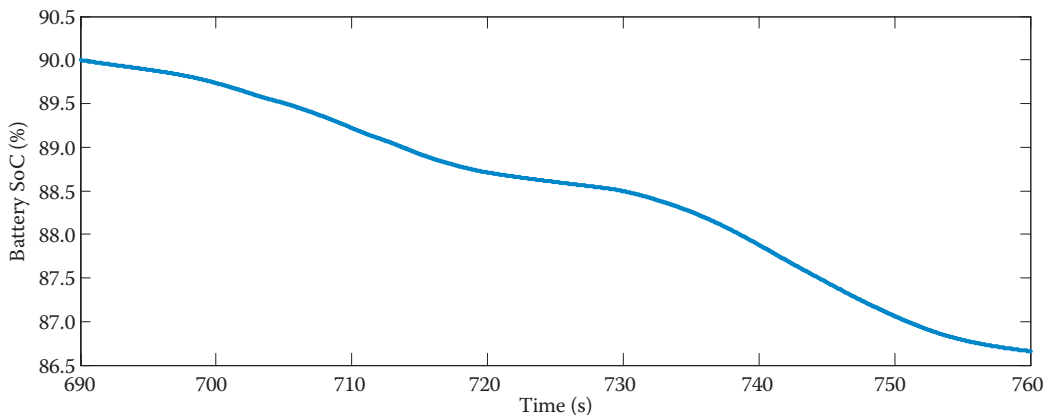


FIGURE 8.36 SoC of the battery for cascaded converters topology with modified controls.

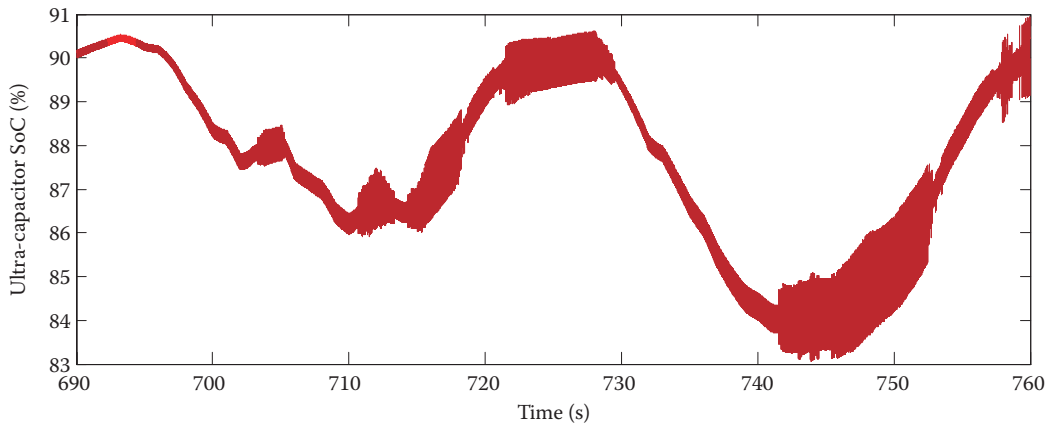


FIGURE 8.37 SoC of the UC with modified controls of the battery.

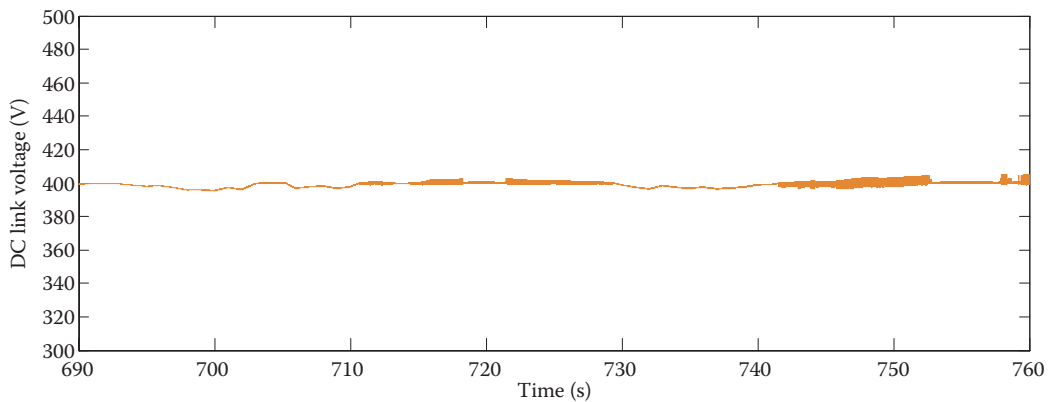


FIGURE 8.38 DC link voltage variation after modified battery current controls.

voltage, the resulting DC link voltage sees slightly more voltage ripple in comparison to the previous configurations. The maximum DC link voltage for this simulation was 405.2 V with a minimum of 395.2 V, and therefore a max/min ripple percentage of 2.5%.

8.4.3 SIMULATION AND ANALYSIS OF PARALLEL-CONNECTED MULTICONVERTERS TOPOLOGY

In this configuration, the battery is connected to the DC link through a bidirectional converter and the UC is connected to the same DC link through another bidirectional converter. The battery and UC are therefore connected to the common DC link in parallel through their individual converters as shown earlier. The same drive cycle was used for load modeling over the same time interval of the previous simulations, the DC link voltage reference was kept the same, and the same strategies were applied for the battery and UC control loops.

The battery and UC current variations are given in Figures 8.39 and 8.40, respectively.

Owing to the battery current control strategy used here and to the parallel-connected individual battery DC/DC converter, the battery current has been further smoothed with reduced current ripples. Although the battery current is limited to be within $[-50, +50]$ A, the battery current stays less than the maximum limit due to the Bessel reference current filter and rising–falling slew rate limiter controller. The only trade-off for having less distortion with the battery current is having

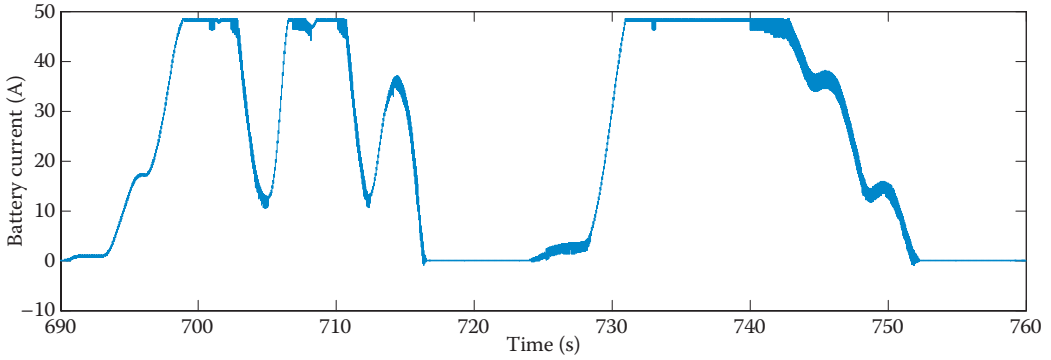


FIGURE 8.39 Battery current with parallel converters topology.

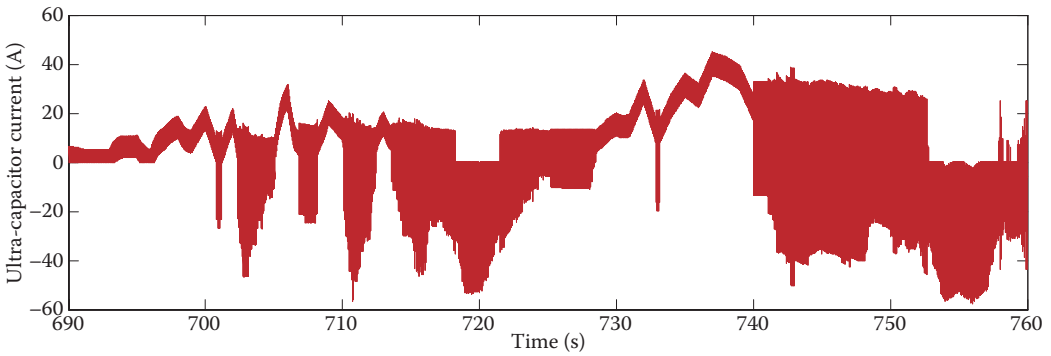


FIGURE 8.40 UC current with parallel converters topology.

huge fluctuations with the UC current. However, the UC is capable of supplying these types of current profiles without sacrificing lifetime and performance.

The SoC variations of the battery and UC are recorded as shown in Figures 8.41 and 8.42, respectively.

From Figures 8.41 and 8.42, it can be observed that the battery is utilized less and maintains a higher SoC at the end of the drive cycle. Since the UC makes a greater contribution, another mode

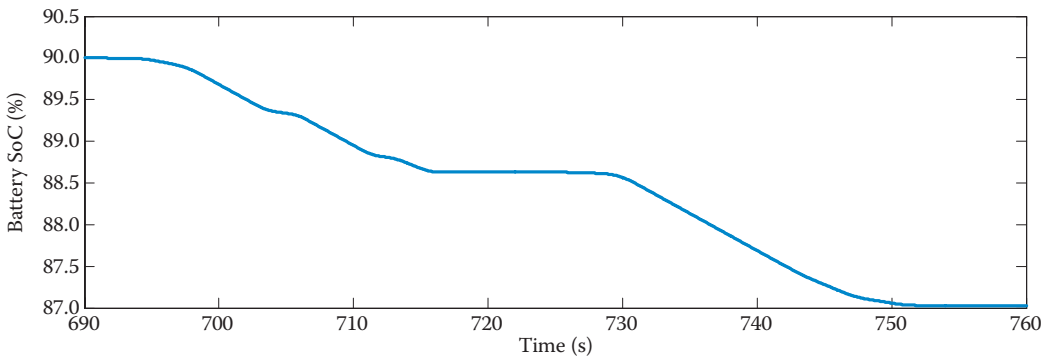


FIGURE 8.41 SoC of the battery with parallel converters topology.

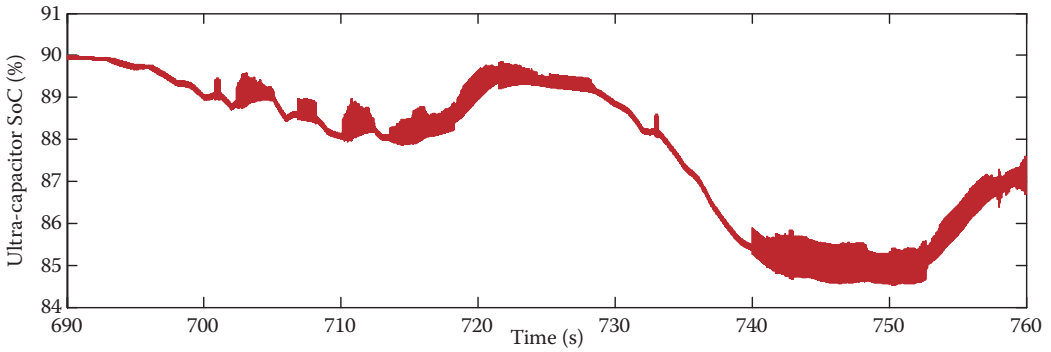


FIGURE 8.42 SoC of the UC with parallel converters topology.

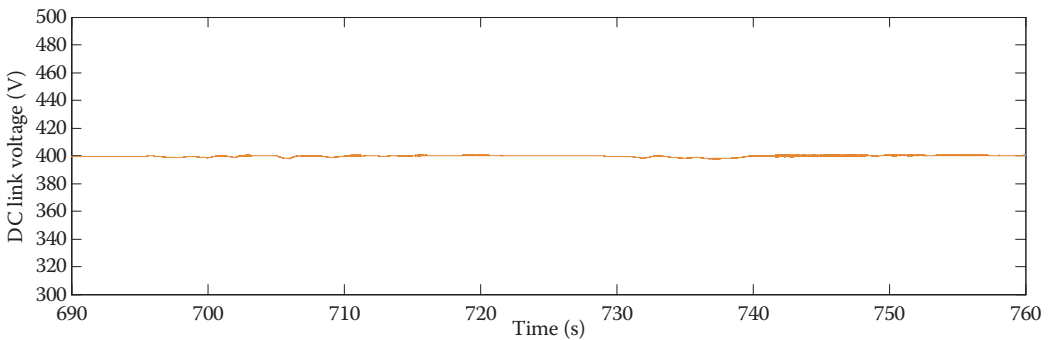


FIGURE 8.43 DC link voltage variation with parallel converters topology.

of operation could be employed such that the battery recharges the UC whenever the UC SoC drops below a certain lower limit. The last result for this topology is shown in Figure 8.43 that is the DC link voltage variation.

Since both UC and its individual parallel converter are controlled to maintain a constant DC link voltage, the DC link voltage has a much smaller voltage ripple than in the previous configurations. In this case, the DC link voltage sees a maximum of 400.7 V and a minimum of 397.6 V, resulting in a maximum ripple percentage of 0.8%.

8.4.4 CONCLUSIONS

This section presented simulations of battery/UC-based hybrid ESS including passive parallel connection, cascaded converters configuration, and the parallel-connected converters configuration. The results of the analysis of these three topologies have been consolidated for comparison in Table 8.4. For some comparison criteria, these topologies have been graded by the authors on a points scale with 1 indicating the best, 2 indicating the better, and 3 indicating the average.

As presented in Table 8.4, the control system is the simplest for the passive parallel topology since there is only one converter current to be regulated. Control of the cascaded converters is more complex as there are two converter currents to be controlled, and the addition of current and slew rate limiters into the cascaded converters controller is obviously still more complicated. Parallel converters also have a similarly high level of complexity but with a bit more freedom in control of current magnitude and direction.

TABLE 8.4
Comparisons of Hybrid ESS Configurations

Criteria	Passive Parallel	Cascaded Converters	Cascaded (Manipulated Controls)	Parallel Converters
Control simplicity	1	2	3	3
Structure complexity	1	2	2	2
Number of converters	1	2	2	2
Number of inductors	1	2	2	2
Total inductor mass	2	3	3	2
Number of transducers	5	6	6	6
Cycle-end battery SoC	86.72%	86.24%	86.66%	87.03%
Cycle-end UC SoC	89.90%	91.91%	90.45%	87.10%
Maximum battery current ripple	~7 A	~9 A	~1.7 A	~1.8 A
Cycle-based topology efficiency	95.24%	90.34%	90.72%	95.25%
Maximum DC link voltage variation percentage	2.52%	2.42%	2.51%	0.77%

The passive parallel configuration also has the most basic structure. The other converters have a similar level of structural complexity as they clearly have a larger number of converters and therefore switches, inductors, bus bars, and so on. The total inductor mass of the passive parallel topology and of the cascaded converters topology is higher than that of the parallel converters topology. In the passive parallel case, 100% of the UC and battery current must pass through a single inductor, requiring high-current-rating wiring of the inductor, and in the cascaded converter, the battery converter carries only the battery current, but the UC converter carries the sum of both the battery and UC currents. However, in the case of parallel converters, although two inductors are required, their sizes are relatively smaller as compared to inductors of the other topologies since each converter carries the current of one source and not of the two sources.

When the topologies are compared in terms of cycle-end battery SoC, the parallel converters are best because of the battery current profile. However, in this case, the UC is utilized more that results in less end of cycle SoC. In the cascaded converters case, the battery sustainably recharges the UC; that is, the battery power is transferred to the UC continually; therefore, the UC's cycle-end SoC is more. The highest battery current ripple occurs when using either the cascaded converter or the passive parallel converters topology since battery current is not effectively controlled and limited in these topologies. The cascaded converters with manipulated controls and the parallel converters inherently provide less battery current ripples and therefore prolong battery life.

The cycle-based energy efficiencies are calculated by numerically integrating the battery power, UC power, and load power over the drive cycle to obtain the total energy flow from each source to the load. Once the energy levels are obtained, the output and input energy relationship defines the cycle-based efficiency. In this case, the cascaded converter topology was the least efficient since there are two cascaded converters and one of them should carry all of the current (again, battery current must pass through two converters). In the passive parallel case, there is only one converter that improves the efficiency, but the most efficient topology is that of the parallel converters, since each of the energy storage devices has its own converter, and power from a single device must never pass through multiple converters. The parallel converters topology is also the best topology in terms of DC link voltage variation due to the fact that one of the converters is always utilized to independently regulate the DC link voltage.

PROBLEMS

An UC module has the following specifications:

Parameter	Value	Unit
Rated capacitance	63	(F)
Maximum ESR _{DC}	18	(mΩ)
Rated voltage	125	(V)
Absolute maximum voltage	136	(V)
Maximum continuous current at 45°C	240	(A)
Maximum peak current for 1 s, nonrepetitive	1800	(A)
Mass	60.5	(kg)

1. Calculate the stored energy of the UC module.
2. Calculate the specific energy of the UC module.
3. Calculate the maximum continuous power and the specific power (watts per kilogram) of the UC module.
4. Verify that the maximum peak current for 1 s is 1800 A as given in the datasheet.
5. Calculate the amount of energy that the UC releases when it is discharged from 125 to 100 V.
6. Assume that this UC module is being discharged with 100 A from initially charged condition. Calculate the module voltage for 10 and 50 s after the discharge starts.
7. When this module is discharging at 100 A in constant current discharge mode, how long does it take to discharge the UC from 125 to 45 V?
8. Calculate the discharge current if the UC voltage is reducing from 125 to 75 V in 300 s.
9. Calculate the power loss if the module is discharged at 10 A of constant current.
10. Calculate how long does it take to discharge the UC from 125 to 5 V at a constant power discharge rate of 1000 W?

A battery pack has the following specifications:

Parameter	Value	Unit
Nominal voltage	360	(V)
Total stored energy	24 (21, total usable)	(kWh)
Maximum continuous output power	100	(kW)
Weight	293.93	(kg)

11. If this battery pack is hybridized with the UC module of which parameters were earlier expressed, calculate the power density of the hybrid ESS and state what percent of power density has been increased as compared to the battery-alone case according to the IEC definition.
12. Calculate the energy density for the same hybrid configuration.

REFERENCES

1. S. Williamson, A. Khaligh, and A. Emadi, Impact of energy storage devices on drive train efficiency and performance of heavy-duty HEVs, *IEEE Vehicle Power and Propulsion Conference (VPPC)*, Chicago, September 2005.
2. A. Khaligh, A. M. Rahimi, Y. J. Lee, J. Cao, A. Emadi, S. D. Andrews, C. Robinson, and C. Finnerty, Digital control of an isolated active hybrid fuel cell/Li-ion battery power supply, *IEEE Transactions on Vehicular Technology*, 56, 3709–3721, November 2007.

3. P. Tiehua, J. Zang, and E. Darcy, Cycling test of commercial nickel–metal hydride (Ni–MH) cells, *Battery Conference on Applications and Advances*, Long Beach, CA, pp. 393–397, January 1998.
4. S. Lukic, S. Wirasingha, F. Rodriguez, J. Cao, and A. Emadi, Power management of an ultra-capacitor/battery hybrid storage system in HEV, *IEEE Vehicle Power and Propulsion Conference (VPPC)*, Windsor, United Kingdom, pp. 1–6, September 2006.
5. A. Emadi, M. Ehsani, and J. M. Miller, *Vehicular Electric Power Systems: Land, Sea, Air, and Space Vehicles*, New York: Marcel Dekker, 2003.
6. J. P. Zheng, T. R. Jow, and M. S. Ding, Hybrid power sources for pulsed current applications, *IEEE Transactions of Aerospace Electronic Systems*, 1(1), 288–292, January 2001.
7. A. Emadi, S. S. Williamson, and A. Khaligh, Power electronics intensive solutions for advanced electric, hybrid electric, and fuel cell vehicular power systems, *IEEE Transactions on Power Electronics*, 21(3), 567–577, May 2006.
8. P. A. Flatherty, Multi-stage hybrid drives for traction applications, in *Proceedings of the Joint Rail Conference*, pp. 171–175, March 2005, Pueblo, Colorado.
9. Maxwell® Technologies, BMOD0063 P125 B33 Ultra-capacitor datasheet, HTM Heavy Transportation Series, available online at: http://www.maxwell.com/ultracapacitors/datasheets/DATASHEET_BMOD0063_1014696.pdf
10. R. A. Dougal, S. Liu, and R. E. White, Power and life extension of battery-ultra-capacitor hybrids, *IEEE Transactions on Components and Packaging Technologies*, 25(1), 120–131, March 2002.
11. L. Solero, A. Lidozzi, and J. A. Pomilio, Design of multiple-input power converter for hybrid vehicles, *IEEE Transactions on Power Electronics*, 20(5), 1007–1016, September 2005.
12. S. Kim and S. H. Choi, Development of fuel cell hybrid vehicle by using ultra-capacitors as a secondary power source, *2005 SAE World Congress*, Detroit, Michigan, April 2005.
13. J. M. Miller and M. Everett, An assessment of ultra-capacitors as power cache in Toyota THS-11, GM-Allision AHS-2 and Ford FHS hybrid propulsion systems, *IEEE 20th Applied Power Electronics Conference and Exposition*, Austin, TX, 1, pp. 481–490, March 2005.
14. A. Napoli, F. Crescimbin, F. Capponi, and L. Solero, Control strategy for multiple input DC–DC converters for hybrid vehicles propulsion systems, *IEEE Power Electronics Specialists Conference*, L'Aquila, Italy, pp. 1685–1690, June 2002.
15. S. Liu and R. A. Dougal, Design and analysis of a current-mode controlled battery/ultracapacitor hybrid, in *Proceedings of the IEEE Industry Applications Society Annual Meeting*, pp. 1140–1145, Seattle, WA, October 2004.
16. O. Onar and A. Khaligh, Dynamic modeling and control of a cascaded active battery/ultra-capacitor based vehicular power system, in *Proceedings of the IEEE Vehicle Power and Propulsion Conference (VPPC)*, Harbin, China, pp. 1–4, September 2008.
17. M. Ortuzar, J. Moreno, and J. Dixon, Ultracapacitor-based auxiliary energy system for an electric vehicle: Implementation and evaluation, *IEEE Transactions on Industrial Electronics*, 54(4), 2147–2156, August 2007.
18. J. Cao and A. Emadi, A new battery/ultra-capacitor hybrid energy storage system for electric, hybrid, and plug-in hybrid electric vehicles, in *Proceedings of the IEEE Vehicle Power and Propulsion Conference (VPPC)*, Dearborn, MI, pp. 941–946, 2009.
19. L. Gao, R. A. Dougal, and S. Liu, Power enhancement of an actively controlled battery/ultracapacitor hybrid, *IEEE Transactions on Power Electronics*, 20(1), 236–243, January 2005.
20. W. Lhomme, P. Delarue, P. Barrade, A. Buoscayrol, and A. Rufer, Design and control of a supercapacitor storage system for traction applications, in *Proceedings of the IEEE Industry Application Conference*, Kowloon, Hong Kong, 3, pp. 2013–2020, October 2005.
21. Z. Jiang and R. A. Dougal, A compact digitally controlled fuel cell/battery hybrid power source, *IEEE Transactions on Industrial Electronics*, 53(4), 1094–1104, June 2006.
22. S. M. Lukic, S. G. Wirashanga, F. Rodriguez, C. Jian, and A. Emadi, Power management of an ultracapacitor/battery hybrid energy storage system in an HEV, in *Proceedings of the IEEE Vehicle Power and Propulsion Conference*, Windsor, United Kingdom, pp. 1–6, 2006.
23. S. M. Lukic, J. Cao, R. C. Bansal, F. Rodriguez, and A. Emadi, Energy storage systems for automotive applications, *IEEE Transactions on Industrial Electronics*, 55(6), 2258–2267, June 2008.
24. Z. Li, O. Onar, A. Khaligh, and E. Schaltz, Power management, design, and simulations of a battery/ultra-capacitor hybrid system for small electric vehicles, in *Proceedings of the SAE (Society of Automotive Engineers) World Congress*, Detroit, MI, USA, April 2009.
25. H. Matsuo, L. Wenzhong, F. Kurokawa, T. Shigemizu, and N. Watanabe, Characterization of the multiple-input DC–DC converter, *IEEE Transactions on Industrial Electronics*, 51(3), 625–631, June 2004.

26. M. H. Kheraluwala, R. W. Gascoine, D. M. Divan, and B. Bauman, Performance characterization of a high power dual active bridge DC/DC converter, in *Proceedings of the IEEE Industry Applications Society Annual Meeting*, 2, Seattle, WA, pp. 1267–1273, 1990.
27. M. Marchesoni and C. Vacca, New DC–DC converter for energy storage system interfacing in fuel cell hybrid electric vehicles, *IEEE Transactions on Power Electronics*, 22(1), 301–308, January 2007.
28. M. C. Kisacikoglu, M. Uzunoglu, and M. S. Alam, Fuzzy logic control of a fuel cell/battery/ultra-capacitor hybrid vehicular power system, in *Proceedings of the Vehicle Power and Propulsion Conference (VPPC)*, Arlington, TX, pp. 591–596, 2007.
29. B. G. Dobbs and P. L. Chapman, A multiple-input DC–DC converter topology, *IEEE Power Electronics Letters*, 1(1), 6–9, March 2003.
30. H.-J. Chiu, H.-M. Huang, L.-W. Lin, and M.-H. Tseng, A multiple-input DC/DC converter for renewable energy systems, in *Proceedings of the IEEE Industrial Conference on Industrial Technology*, Hong Kong, pp. 1304–1308, 2005.
31. Y.-M. Chen, Y.-C. Liu, and F.-Y. Wu, Multi-input DC/DC converter with ripple-free input currents, in *Proceedings of the IEEE Power Electronics Specialists Conference*, Cairns, Qld, Australia, 2, pp. 796–802, 2002.
32. Z. Li, O. Onar, A. Khaligh, and E. Schartz, Design and control of a multiple input DC/DC converter for battery/ultra-capacitor based electric vehicle power system, in *Proceedings of the IEEE 24th Annual Conference on Applied Power Electronics and Exposition (APEC)*, Washington DC, pp. 591–596, February 2009.
33. Z. Amjadi and S. S. Williamson, A novel control technique for a switched-capacitor–converter-based hybrid electric vehicle energy storage system, *IEEE Transactions on Industrial Electronics*, 57(3), 926–934, March 2010.
34. S. Dwari and L. Parsa, A novel high efficiency high power interleaved coupled-inductor boost DC–DC converter for hybrid and fuel cell electric vehicle, in *Proceedings of the IEEE Vehicle Power and Propulsion Conference*, Arlington, TX, pp. 399–404, September 2007.
35. M. B. Camara, F. Gustin, H. Gualous, and A. Berthon, Supercapacitors and battery power management for hybrid vehicle applications using multi boost and full bridge converters, in *Proceedings of the IEEE Europe Conference of Power Electronics Applications*, Aalborg, Denmark, pp. 1–9, September 2007.
36. A. Ioinovici, H. S. H. Chung, M. S. Makowski, and C. K. Tse, Comments on unified analysis of switched-capacitor resonant converters', *IEEE Transactions on Industrial Electronics*, 54(1), 684–685, February 2007.
37. Y. Berkovich, B. Axelrod, S. Tapuchi, and A. Ioinovici, A family of four-quadrant, PWM DC–DC converters, in *Proceedings of the IEEE Power Electronics Specialists Conference*, Orlando, FL, pp. 1878–1883, June 2007.
38. H. S. Chung and A. Ioinovici, Development of a general switched-capacitor DC/DC converter with bi-directional power flow, in *Proceedings of the IEEE International Symposium on Circuits and Systems*, Geneva, Italy, 3, pp. 499–502, May 2003.
39. O. C. Mak, Y. C. Wong, and A. Ioinovici, Step-up DC power supply based on a switched-capacitor circuit, *IEEE Transactions on Industrial Electronics*, 42(1), 90–97, February 1995.
40. O. C. Onar and A. Khaligh, A novel integrated magnetic structure based DC/DC converter for hybrid battery/ultracapacitor energy storage systems, *IEEE Transactions on Smart Grid*, 3(1), 296–307, March 2012.
41. R. Hebner, J. Beno, and A. Walls, Flywheel batteries come around again, *IEEE Spectrum*, 39(4), 46–51, April 2002.
42. T. M. Mulcahy, J. R. Hull, K. L. Uherka, R. C. Niemann, R. G. Abboud, J. P. Juna, and J. A. Lockwood, Flywheel energy storage advances using HTS bearings, *IEEE Transactions on Applied Superconducting*, 9(2), 297–300, June 1999.
43. A. Jaafar, C. R. Akli, B. Sareni, X. Roboam, and A. Jeunesse, Sizing and energy management of a hybrid locomotive based on flywheel and accumulators, *IEEE Transactions on Vehicular Technology*, 58(8), 3947–3958, October 2009.
44. O. Briat, J. M. Vinassa, W. Lajnef, S. Azzopardi, and E. Woirgard, Principle, design, and experimental validation of a flywheel-battery hybrid source for heavy-duty electric vehicles, *IET Electric Power Applications*, 1(5), 665–674, 2007.
45. S. Talebi, B. Nikbakhtian, and H. Toliyat, A novel algorithm for designing the PID controllers of high-speed flywheels for traction applications, in *Proceedings of the Vehicle Power and Propulsion Conference (VPPC)*, Arlington, TX, pp. 574–579, 2007.
46. S. Shen and F. E. Veldpaus, Analysis and control of a flywheel hybrid vehicular powertrain, *IEEE Transactions on Control Systems*, 12(5), 645–660, September 2004.

47. J. G. Oliviera, A. Larsson, and H. Bernhoff, Controlling a permanent-magnet motor using PWM converter in flywheel energy storage systems, in *Proceedings of the IEEE Industrial Electronics Conference (IECON)*, Orlando, FL, pp. 3364–3369, 2008.
48. R. I. Davis and R. D. Lorenz, Engine torque ripple cancellation with an integrated starter alternator in a hybrid electric vehicle: Implementation and control, *IEEE Transactions on Industry Applications*, 39(6), 1765–1773, November/December 2003.
49. S. Lemofouet and A. Rufer, A hybrid energy storage system based on compressed air and supercapacitors with maximum efficiency point tracking (MEPT), *IEEE Transactions on Industrial Electronics*, 53(4), 1105–1115, August 2006.
50. J. Lehmann, Air storage gas turbine power plants, a major distribution for energy storage, in *Proceedings of the International Conference on Energy Storage*, United Kingdom, pp. 327–336, April 1981.
51. A. Rufer and S. Lemofouet, Energetic performance of a hybrid energy storage system based on compressed air and super capacitors, in *Proceedings of the International Symposium on Power Electronics, Electrical Drives, Automation, and Motion (SPEDAM)*, Taormina, Italy, pp. 469–474, 2006.
52. A. Rufer and S. Lemofouet, Efficiency consideration and measurements of a hybrid energy storage system based on compressed air and super capacitors, in *Proceedings of the International Power Electronics and Motion Control Conference (EPE-PEMC)*, Portoroz, Slovenia, pp. 2077–2081, 2006.
53. P. F. Ribeiro, B. K. Johnson, M. L. Crow, A. Arsoy, and Y. Liu, Energy storage systems for advanced power applications, *Proceedings of the IEEE*, 89(12), 1744–1756, 2001.
54. M. H. Ali, B. Wu, and R. A. Dougal, An overview of SMES applications in power and energy systems, *IEEE Transactions on Sustainable Energy*, 1(1), 38–47, April 2010.
55. T. Ise, M. Kita, and A. Taguchi, A hybrid energy storage with a SMES and secondary battery, *IEEE Transactions on Applied Superconductivity*, 15(2), 1915–1918, June 2005.
56. H. Zhang, J. Ren, Y. Zhong, and J. Chen, Design and test of controller in power conditioning system for superconducting magnetic energy storage, in *Proceedings of the International Conference on Power Electronics (ICPE)*, Daegu, South Korea, pp. 966–972, 2001.
57. L. Trevisani, A. Morandi, F. Negrini, P. L. Ribani, and M. Fabbri, Cryogenic fuel-cooled SMES for hybrid vehicle application, *IEEE Transactions on Applied Superconductivity*, 19(3), 2008–2011, June 2009.
58. R. F. Giese, Progress toward high temperature superconducting magnetic energy storage (SMES) systems—A second look, *Technical Report by Argonne National Laboratory*, 1998.
59. A. P. Malozemoff, J. Maguire, B. Gamble, and S. Kalsi, Power applications of high-temperature superconductors: Status and perspective, *IEEE Transactions on Applied Superconductivity*, 12(1), 778–781, March 2002.
60. C. A. Luongo, Superconducting storage systems, *IEEE Transactions on Magnetics*, 32(4), 2214–2223, 1996.
61. Toyota officially launches plug-in Prius program, retail sales in 2011, Autobloggreen, Available online: <http://green.autoblog.com/2009/12/14/toyota-officially-launches-plug-in-prius-program-retail-sales-ii/>
62. Y. Tanaka, Prius plug-in hybrid vehicle overview, *Technical Report by Toyota Passenger Vehicle Development Center*, Available online: http://www.toyota.co.jp/en/tech/environment/conference09/pdf/phv_overview_en.pdf, December 2009.
63. Maxwell Technologies BMODO165-48.6 V ultra-capacitors' data sheet, Available online: http://www.maxwell.com/ultracapacitors/datasheets/DATASHEET_48V_series_1009365.pdf



CHAPTER

5

SOLAR POWERED CHARGING SYSTEMS

Solar Powered Charging
Infrastructure for
Electric Vehicles

A Sustainable Development



Edited by
Larry E. Erickson • Jessica Robinson
Gary Brase • Jackson Cutsor



This chapter is excerpted from

*Solar Powered Charging Infrastructure for Electric
Vehicles: A Sustainable Development*

by Larry E. Erickson, Jessica Robinson, Gary Brase &
Jackson Cutsor

© 2017 Taylor & Francis Group. All rights reserved.



[Learn more](#)

3

Solar Powered Charging Stations

Larry E. Erickson, Jackson Cutsor, and Jessica Robinson

CONTENTS

3.1 Social Benefits of SPCSs	25
3.2 Environmental Benefits of SPCSs	26
3.3 Economic Benefits	26
3.4 Electric Vehicle Supply Equipment	27
3.5 Locations for SPCSs	28
3.6 Energy Storage	29
3.7 Business Models for SPCSs.....	30
3.8 Life Cycle Analysis of SPCSs.....	32
3.9 Conclusions.....	32
References.....	33

When something is important enough, you do it even if the odds are not in your favor.

Elon Musk

Solar powered charging stations (SPCSs) are one of the important developments related to the electrification of transportation. The number of sites with SPCSs is increasing because of their value and convenience. In many cases, the SPCSs are designed to allow the electricity that is generated to flow into the local electrical grid. The solar panels provide shade in the parking lot, and the charge station is connected to the grid such that power for charging EVs is available at all times. At some sites there are batteries for electrical storage also. Some sites have battery storage without any grid connection. In cases where the power is provided to the EV without any cost to the owner of the EV, the charging equipment is simpler than when customers need to pay for connecting to the electric vehicle supply equipment (EVSE).

Many SPCSs have a concrete base, steel frames and supports, and needed electrical components including transformers, wires, and inverters. In many cases, there is a payment station with payment software and hardware and communication capabilities.

In some locations, there are solar panels in parking lots, but there are no charging stations for EVs. These structures have been put in place to produce

electricity and provide shade. Some were put in place before there was a demand for EVSEs. In these cases, a decision was made to construct the system without considering the need for EVSE infrastructure for EVs. There are many locations where SPCSs can be used to increase the amount of power generated with sustainable energy at competitive prices. Adding sustainable energy to the electrical grid with SPCSs has value for society because it is a very clean source of energy. These sites can be easily equipped with EVSEs when there is a need for them.

Envision Solar International, Inc. (2015) has developed a solar powered charge station with battery storage that is designed to be self contained and not connected to the electrical grid. This electric vehicle autonomous renewable charger can be towed to the site and used immediately. It also can be moved to a new site easily. It has 22 kWh of battery storage, which allows about one day of energy storage. The 2.3 kW solar array generates approximately 16 kWh/day, and it has a solar tracker to allow the solar array to follow the sun. This system can be installed at locations where there is no grid such as in parks, trail heads, and along roads where tourists may wish to stop. See Figure 3.1.

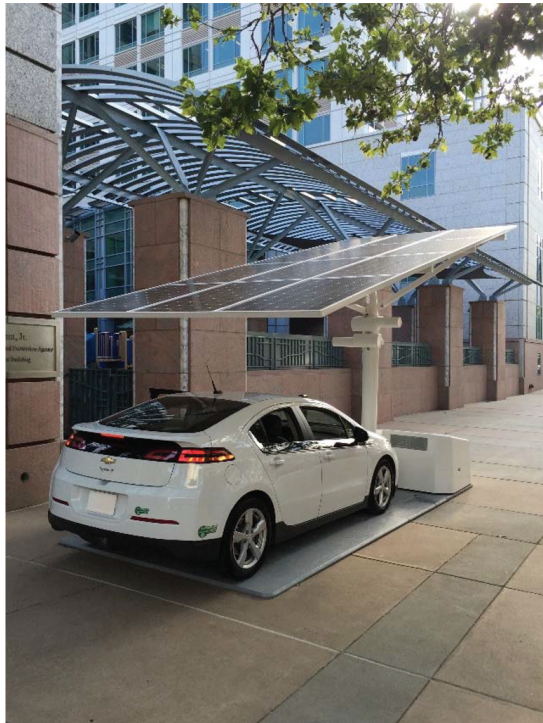


FIGURE 3.1

Solar powered charging system with battery storage available from Envision Solar International. (Photo provided by Envision Solar International, Inc.)

The amount of power that flows from the solar panels over a parking space depends on location, area of the panels, and efficiency. For instance, in Kansas a reasonable estimate is 16 kWh/day for one parking space. If 200 million parking spaces are covered with solar panels, 3.2 billion kWh/day could be generated, which can be compared to 11.2 billion kWh generated in the entire United States on an average day (Erickson et al., 2015). There are more than 200 million vehicles in use in the United States, and there are many more parking spaces than vehicles because there are always many empty parking spaces at any given time. Sports stadiums, church parking lots, shopping centers, and many work sites have empty spaces in their parking lots at many times during the week. The available land for SPCSs, the potential reduction in greenhouse gas emissions, and the reduced use of water compared to alternatives are metrics that favor SPCSs.

This chapter provides an introduction to SPCSs, and it builds on earlier papers by Goldin et al. (2014) and Robinson et al. (2014). The SPCS is an ideal example of sustainable development and the application of the triple bottom line principle: There are social, environmental, and economic benefits associated with SPCSs.

3.1 Social Benefits of SPCSs

Social benefits include shade, better air quality, and convenience. There are personal comfort benefits associated with entering a vehicle that has been in the shade on a hot summer day. Goldin et al. (2014) point out that the temperature in a car that is in the shade on a hot day may be more than 50°F lower. The social value of better air quality because of EVs and SPCSs is a benefit that impacts everyone. Economically SPCSs provide construction and maintenance jobs and reduce travel costs.

The reduction of greenhouse gas emissions has global benefits while the improved urban air quality associated with the transition to EVs and SPCSs benefits everyone in the urban area. Quality of life issues are important to many people. For example, some people move to the edge of an urban area in order to have better air quality.

Convenience is of significant social value to many people. If EV owners are able to plug in when they arrive at their parking space at work, when they stop at the mall after work, and when they are at home, this will have value for them, especially if there is a need to charge the batteries at sites other than at home. Constructing SPCSs at many locations will improve convenience for many EV owners. This convenience may help to retain employees, attract customers to a store, health club, or restaurant, and encourage purchases of EVs.

3.2 Environmental Benefits of SPCSs

Environmental benefits include reduced greenhouse gas emissions, better air quality in urban environments, and less noise. The transition to SPCSs has global environmental benefits because of reduced greenhouse gas emissions. The global goal of reducing emissions by 80% by 2050 will require significant changes, including the electrification of transportation and the generation of most of the electricity using sustainable methods such as solar panels. The electricity generated by SPCSs does not have air emissions associated with it. Air quality is impacted by emissions associated with coal fire power plants. Combustion gases can be controlled; however, there are costs associated with this and pollutants that are removed from the air exhaust become pollutants in waste water in some cases. There are no significant water requirements associated with solar energy compared to electricity generated with coal, nuclear, and natural gas where cooling water is used and lost to the atmosphere. Petroleum, coal, and natural gas production have significant environmental impacts, risks of production level spills and contamination, water use is significant, pipelines for transportation may rupture, and coal trains may leave the tracks.

A phenomenon affecting large cities is the urban heat island effect. This occurs because of a lack of vegetation, massive quantities of heat-absorbing materials such as concrete, and tall buildings that alter wind patterns. All of these issues make cities one or more degrees centigrade warmer than the surrounding rural areas on average. The solar panels on buildings and on SPCSs take solar energy and convert it to electrical energy, much like plants take light energy and convert it to chemical energy. Since EVs are much more efficient compared to cars with internal combustion engines (ICEs), the amount of heat generated per mile traveled by transportation is reduced. Per mile traveled, the ICE uses about 3 to 4 times as much energy as an EV. These two factors reduce the heat island effect.

In the STAR Community Rating System (STAR, 2015), SPCSs and EVs help communities meet 12 of 44 objectives, including green infrastructure, ambient noise, green market development, greenhouse gas mitigation, resource efficient public infrastructure, and greening the energy supply. STAR refers to Sustainability Tools for Assessing and Rating communities, and the STAR system is helpful to communities that want to track their progress toward a number of sustainability objectives.

3.3 Economic Benefits

Economically, SPCSs are beneficial on both a local and national level. They create temporary construction jobs and employment for those who produce

the materials and parts that are used for the construction of the SPCS. There is also employment for those who manage and maintain the SPCSs.

Businesses, especially those with large fleets of vehicles, have the potential to save money by investing in SPCSs and EVs. Delivery vehicles can be drastically cheaper to operate with electrical power and with SPCSs can potentially be free to fuel after the initial investment has been paid off. The operational cost is about 33%–50% of a conventional vehicle if maintenance costs are included. The U.S. Postal Service could save on operational costs by using EVs and SPCSs. Since the EV does not use much power while it is stopped, it is especially efficient for mail delivery. Businesses have other reasons to invest, like the green halo effect and employee retention. Free charging while at work is an inexpensive benefit for a company to provide. People respect businesses that are ecofriendly, and this may help attract and keep customers, especially those who appreciate free charging while at the business.

The operating and maintenance costs of an EV are less than for an auto with an internal combustion engine. Goldin et al. (2014) reported that the cost of transportation is least for the Nissan Leaf EV when it is compared to several other vehicles. If SPCSs allow an individual to use a Leaf to come to work, this has economic value because transportation costs are reduced. When it is powered by electricity from solar energy, the Leaf is a very clean form of transportation, and this has economic value because the improved air quality reduces health costs in urban areas where air quality is impacted by transportation emissions. The economic benefits include the greater value a vehicle has as a used vehicle when it has been sheltered from the sun regularly. Battery life in EVs may be impacted by high temperature, and shaded parking may be beneficial on hot summer days. In the future, solar panel costs and battery costs are expected to be less than they are today. Simple, inexpensive electric vehicles will have great utility in many parts of the world, especially if they can be supported by SPCSs at many locations. For instance, Jordan is one of the countries that are moving forward with EVs and SPCSs (Ajumni, 2015).

3.4 Electric Vehicle Supply Equipment

The equipment that is used to charge electric vehicles includes Level 1, Level 2, and high rate EVSE (USDOE, 2013). Level 1 EVSE is for use with a 120 volt AC circuit. Most EVs are supplied with a Level 1 charging cord that has an automatic stop to terminate charging when the battery is charged. There is a standard 120 volt three-prong household plug on one end and a standard connector that plugs into the vehicle on the other end. Level 1 charging often adds about 5 miles of range or about 2 kWh per hour to the batteries. This

rate of charging is about equal to the rate of supply of the solar panels above one parking space.

Level 2 EVSE uses a 240 volt supply often with a dedicated 40 amp circuit to provide approximately 18 miles of range or about 6 kWh per hour to the batteries. In many cases, the connection to the power supply is hard wired for safety. It is connected to the vehicle with the same J1772 standard connector as is used for Level 1 charging. The rate of charging depends on the charger that is in the vehicle. A 30 amp rate is commonly used.

Level 3 EVSE is often identified as DC fast charging and it is not as standardized as Level 1 and Level 2. Some EVs such as the Nissan Leaf that are equipped to accept DC fast charging have the CHAdeMO connector (Herron, 2015). There is also the SAE Combo Charging System (SAE CCS), which is used by European companies such as VW and BMW. Tesla has a supercharger connector, which is specific to the Tesla, but there is an adapter that allows the CHAdeMO connector to be used with the Tesla (Tesla, 2015). Herron (2015) has pointed out that the CHAdeMo system was developed in Japan while the SAE CCS was developed to meet SAE standards. All three systems are available in the United States at many locations. There is a need to standardize Level 3 charging (Herron, 2015). Most DC fast chargers are designed to provide rapid direct current charging over a 20–30 min time period with a final charge that is about 3/4 of a full charge. With fast charging 50–70 miles of range are added in 20 min.

There are many places where the EVSE system does not need to accept credit cards or identification cards. In places where the EVSE needs to process credit charges, there are many systems that are able to do this. When a credit card is used, there are often some transaction costs that must be paid. These can be a substantial part of the total bill when the cost of charging is modest.

3.5 Locations for SPCSs

There are three important variations for locations for SPCSs: home, along travel routes, and where drivers stop for an hour or more. Many EV owners will have a charge station at home. This may involve solar panels on a roof or car port. Recently, rapid charging EVSEs have been installed along some interstate highways. Tesla Motors has a network of these in the United States and in Europe. The Tesla high rate EVSE system includes solar panels and batteries for energy storage. Because of the expense associated with rapid charging from the electrical grid, the rapid charging is accomplished using the stored energy in the batteries. There is no charge for Tesla owners to use these charge stations. The third location for SPCSs is where individuals stop for an hour or more, and work sites are the most common of these.

It is becoming increasingly common for work sites to have SPCSs. Other locations where SPCSs may be installed include malls, hotels, gyms, eating establishments, stadiums, parks, churches, and zoos. Service stations may also install SPCSs.

The installation of SPCSs at many locations will help address the range anxiety that affects sales of EVs. If EV owners have a large number of SPCSs at many locations that are available to them, this will allow EVs to be used for more trips. If there were 200 million SPCSs in the United States with an appropriate mix of Level 1, Level 2, and Level 3 SPCSs, the range anxiety issue would be reduced. Many SPCSs that are connected to the grid can be very beneficial even if they are seldom used for EV charging because they are generating clean electricity for the electrical grid.

As EV use grows and demand for SPCSs increases, one variation that is anticipated to become popular is a canopy of solar panels such that entire parking lots are filled with SPCSs. The cost of construction and connection to the grid is less per SPCS when there are many SPCSs. The shaded parking is appreciated by all who park in the lot. Free Level 1 charging can be offered by installing 110 volt receptacles. It is important to be able to use, store, or sell all of the electricity that is generated. When there is a large array of solar panels, there may be opportunities to collect and manage rain water to reduce flooding and make use of the water at a later time.

For homes, garages, and apartment buildings, the solar panels can be mounted to the roof and the charge station equipment can be in the garage or near a parking space along the side of the building. There may be energy storage as well because it can provide electrical power when there is failure in the grid supplied power. This can also be a source of power at night when the solar panels are not producing power. Homes may be the most popular location for SPCSs. Having an EV makes solar panels more attractive for homeowners and having solar panels makes owning an EV more attractive. With time-of-use prices, it may even be best to have excess power produced by the solar panels flow into the grid during the day and then charge the EV with cheaper grid power at night.

3.6 Energy Storage

As the cost of batteries decreases, there will be greater use of energy storage in parking lots with SPCSs and EVSE. Solar energy is available during the day, but not at night. The ability to store electrical energy in batteries has value because it can then be used at a later time when demand is higher. As the sun sets, electrical power needs are often significant (as many people arrive at home after work), and this is a time when stored energy might be used. Stored energy allows the parking lot operator greater flexibility to

serve the needs of those who wish to charge their vehicles. With time-of-use prices for electricity, there may be economic benefits of storage that help to pay for the cost of the batteries that are used for storage.

One of the opportunities for energy storage is to take the older batteries from EVs and use them for energy storage in parking lots with SPCSs. The cost of batteries is going down as new developments are commercialized and companies are finding efficiencies. In 2015, battery costs were about \$300/kWh (Nykvist and Nilsson, 2015); they are expected to decrease to about \$125/kWh by 2022 (USDOE, 2014). As the price of batteries decreases and the percentage of electricity from solar and wind energy generation increases, there will be more battery storage. Time of use prices provide incentives for energy storage in EV batteries and those in parking lots and other locations.

3.7 Business Models for SPCSs

Robinson et al. (2014) describe several business models for SPCSs. The Tesla model is to provide a needed infrastructure with free fast DC charging with the expectation that this will help sales of Tesla cars. As of May 2015, there were more than 400 Tesla Supercharger stations (Richard, 2015). A photo of a Tesla Supercharger station is shown in Figure 3.2. Many employers presently



FIGURE 3.2

This Tesla Supercharger is an example of an SPCS. Solar panels are on the overhead structure with the charging station below. (Photographed by Tesla Press. Tesla Presskit. *Tesla Motors*. n.p., 2015. Web. Jan. 14, 2016. <https://teslamotors.app.box.com/pressfiles>.)

provide free parking for their employees. It is logical to extend this fringe benefit to free charging of EVs, and some employers have done this. If an employee drives 40 miles to get to work, the cost of charging the batteries at 12 cents per kWh would be about \$1.60 for an efficiency of 3 miles/kWh. If the installation of the SPCS system costs \$10,000/parking place, and it is used 250 days per year for 20 years, the cost per day is \$2.00/day. If 16 kWh are generated and 13.3 are used to charge the vehicle, 2.7 kWh enter the grid. All 16 kWh enter the grid on days when there are no vehicles being charged.

The concept of free EV charging for employees while at work could be justified as an incentive to encourage EV purchases because of the importance of reducing greenhouse gas emissions. For example, the federal government could add SPCSs to its parking lots and provide free charging in the lots.

In many cases the employer can make use of any electricity that flows into the company grid from the SPCSs. As the number of SPCSs increases, there may be a need to make provisions for electricity to flow into the electrical grid that is managed by the electric utilities. Presently, electricity that is generated by solar energy has above average value when time-of-use prices are considered. The lowest prices are at night, and the highest prices are in the late afternoon. On a normal working day, EV owners can plug in when they arrive at work. In the afternoon when most cars are charged, there will be power to flow to the grid from the SPCSs at an above average price if time-of-use prices are used.

For workplace charging, Level 1 and Level 2 charging are sufficient for those workers who park their vehicle for 8 hours or more while they are at work. For those who have a 1-hour commute to work, the vehicle can be nearly completely charged during a full work day with Level 1 charging. For some company vehicles, there may be a need for fast charging if the vehicle is used for business purposes during the day.

In cities, there may be public parking lots where SPCSs can be added or installed when a new parking lot is constructed. There are several options for SPCSs in public parking lots. Where there is free parking, there can be free use of the charge stations as well. This can be paid for through a sales tax or the same source of funds that is used to maintain the free parking. Where there is metered parking, the cost of charging can be recovered from the meter income. In parking garages, the cost of charging can be included in the parking fees. Here the solar panels may be on top of the garage. Another alternative is to allow the local electric utility to construct and operate the SPCSs and collect income from use of the charge station. This may require the utility to work with the regulatory organization that determines their rates to approve a special rate for sale of electricity at SPCSs.

Volta (2015) is a company that sells advertising and provides free EV charging. The idea of using advertising income to help pay for SPCSs can be implemented in many locations and parking lots. The listed price for an SPCS marketed by EcoVantage with Level 2 charging, advertising panels, and LED lights is \$17,445 (EcoVantage, 2015).

Envision Solar (2015) markets a solar tree that has solar panels with a tree structure that is 35 feet × 35 feet and tracks the sun. It shades 6–8 parking spaces and generates sufficient electricity for about 700 e-miles each day. It can be installed with or without grid connections, battery storage, and advertising space. Because it tracks the sun, it generates more electricity per unit area than a stationary system.

In some work environments, the employees may need to pay for the cost of the SPCSs. One approach to doing this is to make use of parking permits that allow the user to park in the shade of the SPCS and plug in to the EVSE. In this case, the income from the permits and the electricity that flows into the grid needs to be sufficient to pay for the SPCSs.

3.8 Life Cycle Analysis of SPCSs

Life cycle analysis (LCA) has been used to make comparisons that look at all aspects of a new process or product. Engholm et al. (2013) have completed an LCA of an SPCS. The LCA shows that the SPCS is a very good and appropriate product when greenhouse gas emissions are considered. There is a need for electrical energy to produce the solar panels, but the amount is much smaller than the energy generated by the solar panels over their estimated life. If the electrical power that is needed to produce the solar panels comes from wind or solar energy, then the LCA is even more positive.

When there are new developments that result in modernization or replacement of SPCSs, many parts of the SPCS can be recycled. During the next 30 years, progress in solar energy development should lead to more efficient solar panels that make it appropriate to upgrade the SPCSs.

3.9 Conclusions

One way to have green electricity for EVs is to fill parking lots with SPCSs. There are social, environmental, and economic reasons for installing SPCSs and there are presently many SPCSs in the United States and some other countries. As prices of batteries come down, there will be more battery storage of electricity generated by SPCSs. The most popular locations for SPCSs are homes, places of employment, shopping malls, and along major highways.

References

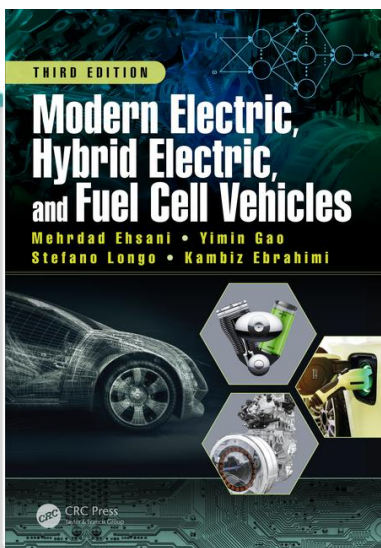
- Ajumni, D. 2015. Jordan plans to build 30 mw solar-powered electric vehicle charging network, *PVBZZ*, January 10, 2015; <http://www.pvbuzz.com/>.
- EcoVantage. 2015. EcoVantage Catalog, EcoVantage Energy, Inc.; <http://www.ecovantageenergy.com/catalog/>.
- Engholm, A., G. Johansson, and A.A. Persson. 2013. Life Cycle Assessment of Solelia Greentech's Photovoltaic Based Charging Station for Electric Vehicles, Uppsala University, Sweden.
- Envision Solar. 2015. Internet Site of Envision Solar International, Inc.; <http://www.envisionsolar.com/>.
- Erickson, L.E., A. Burkey, K.G. Morrissey et al. 2015. Social, economic, technological, and environmental impacts of the development and implementation of solar-powered charge stations, *Environmental Progress and Sustainable Energy* 34: 1808–1813.
- Goldin, E., L.E. Erickson, B. Natarajan, G. Brase, and A. Pahwa. 2014. Solar powered charge stations for electric vehicles, *Environmental Progress and Sustainable Energy* 33: 1298–1308.
- Herron, D. 2015. EV DC Fast Charging Standards—CHAdEMO, CCS, SAE Combo, Tesla Super Charger, etc., The Long Tail Pipe, August 11, 2015; <http://longtailpipe.com/>.
- Nykvist, B. and M. Nilsson. 2015. Rapidly falling costs of battery packs for electric vehicles, *Nature Climate Change* 5: 329–332.
- Richard, M.G. 2015. Tesla's free-to-use Superchargers growing like weeds worldwide. *Treehugger*, May 27, 2015; <http://www.treehugger.com/>.
- Robinson, J., G. Brase, W. Griswold, C. Jackson, and L.E. Erickson. 2014. Business models for solar powered charging stations to develop infrastructure for electric vehicles, *Sustainability* 6: 7358–7387.
- STAR. 2015. STAR community rating system, Version 1.2, March 2015; <http://www.starcommunities.org/rating-system/>.
- Tesla. 2015. CHAdEMO Adapters; http://shop.teslamotors.com/products/chademo_adapter/.
- Tesla Presskit. 2015. *Tesla Motors*, January 14, 2016; <https://teslamotors.app.box.com/pressfiles>.
- U.S. Department of Energy (USDOE). 2013. *Plug-in Electric Vehicle Handbook*, U.S. Department of Energy DOE/GO-102013-3925; <http://cleancities.energy.gov/publications>.
- U.S. Department of Energy (USDOE). 2014. U.S. Department of Energy vehicle technologies office: Plug-in electric vehicles and batteries; <http://energy.gov/eere/>.



CHAPTER

6

ENVIRONMENTAL IMPACT AND HISTORY OF MODERN TRANSPORTATION



This chapter is excerpted from

*Modern Electric, Hybrid Electric, and Fuel Cell Vehicles,
Third Edition*

by Mehrdad Ehsani, Yimin Gao, Stefano Longo,
Kambiz Ebrahimi.

© 2018 Taylor & Francis Group. All rights reserved.



[Learn more](#)

1

Environmental Impact and History of Modern Transportation

The development of internal combustion (IC) engine vehicles, and especially automobiles, is one of the greatest achievements of modern technology. Automobiles have made great contributions to the growth of modern society by satisfying many of the needs for mobility in everyday life. The rapid development of the automotive industry, unlike that of any other industry, has prompted the progress of human beings from a primitive society to a highly developed industrial one. The automobile industry and the other industries that serve it constitute the backbone of the world's economy and employ the greatest share of the working population.

However, the large number of automobiles in use around the world has caused and continues to cause serious problems for the environment and human life. Air pollution, global warming, and the rapid depletion of the Earth's petroleum resources are now problems of paramount concern.

In recent decades, the research and development activities related to transportation have emphasized the development of high-efficiency, clean, and safe transportation. Electric vehicles (EVs), hybrid electric vehicles (HEVs), and fuel cell vehicles have been typically proposed to replace conventional vehicles in the near future.

This chapter reviews the problems of air pollution, gas emissions causing global warming, and petroleum resource depletion. It also briefly reviews the history of EVs, HEVs, and fuel cell technology.

1.1 Air Pollution

At present, all vehicles rely on the combustion of hydrocarbon (HC) fuels to derive the energy necessary for their propulsion. Combustion is a reaction between the fuel and the air that releases heat and combustion products. The heat is converted to mechanical power by an engine, and the combustion products are released into the atmosphere. An HC is a chemical compound with molecules made up of carbon and hydrogen atoms. Ideally, the combustion of an HC yields only carbon dioxide and water, which do not harm the environment. Indeed, green plants "digest" carbon dioxide by photosynthesis. Carbon dioxide is a necessary ingredient in vegetal life. Animals do not suffer by breathing carbon dioxide unless its concentration in air is such that oxygen is almost absent.

The combustion of HC fuel in combustion engines is never ideal. Besides carbon dioxide and water, the combustion products contain a certain amount of nitrogen oxides (NO_x), carbon monoxides (CO), and unburned HCs, all of which are toxic to human health.

1.1.1 Nitrogen Oxides

Nitrogen oxides (NO_x) result from the reaction between nitrogen in the air and oxygen. Theoretically, nitrogen is an inert gas. However, the high temperatures and pressures in engines create favorable conditions for the formation of nitrogen oxides. Temperature is by far the most important parameter in nitrogen oxide formation. The most commonly found nitrogen oxide is nitric oxide (NO), although small amounts of nitric dioxide (NO_2) and traces of nitrous oxide (N_2O) are present. Once released into the atmosphere, NO reacts with oxygen to form NO_2 . This is later decomposed by the Sun's ultraviolet radiation back to NO and highly reactive oxygen atoms that attack the membranes of living cells. Nitrogen dioxide is partly responsible for smog; its brownish color makes smog visible. It also reacts with atmospheric water to form nitric acid (HNO_3), which dilutes in rain. This phenomenon is referred to as "acid rain" and is responsible for the destruction of forests in industrialized countries.¹ Acid rain also contributes to the degradation of historical monuments made of marble.¹

1.1.2 Carbon Monoxide

Carbon monoxide results from the incomplete combustion of HCs due to a lack of oxygen.¹ It is a poison to human beings and animals that inhale/breathe it. Once carbon monoxide reaches blood cells, it attaches to the hemoglobin in place of oxygen, thereby diminishing the quantity of oxygen that reaches the organs and reducing the physical and mental abilities of the affected living beings.¹ Dizziness is the first symptom of carbon monoxide poisoning, which can rapidly lead to death. Carbon monoxide binds more strongly to hemoglobin than oxygen. The bonds are so strong that normal body functions cannot break them. People intoxicated by carbon monoxide must be treated in pressurized chambers, where the pressure makes it easier to break the carbon monoxide–hemoglobin bonds.

1.1.3 Unburned HCs

Unburned HCs are a result of the incomplete combustion of HCs.^{1,2} Depending on their nature, unburned HCs may be harmful to living beings.² Some of these unburned HCs may be direct poisons or carcinogenic chemicals such as particulates, benzene, or others. Unburned HCs are also responsible for smog; the Sun's ultraviolet radiation interacts with the unburned HCs and NO in the atmosphere to form ozone and other products. Ozone is a molecule formed by three oxygen atoms. It is colorless but very dangerous and poisonous because it attacks the membranes of living cells, causing them to age prematurely or die. Toddlers, older people, and asthmatics suffer greatly from exposure to high ozone concentrations. Annually, deaths from high ozone peaks in polluted cities have been reported.³

1.1.4 Other Pollutants

Impurities in fuels result in the emission of pollutants. The major impurity is sulfur, mostly found in diesel and jet fuel but also in gasoline and natural gas.¹ The combustion of sulfur (or sulfur compounds such as hydrogen sulfide) with oxygen releases sulfur oxides (SO_x). Sulfur dioxide (SO_2) is the major product of this combustion. On contact with air, it forms sulfur trioxide, which later reacts with water to form sulfuric acid, a major component of acid rain. It should be noted that sulfur oxide emissions originate from transportation sources but also largely from the combustion of coal in power plants and steel factories. In addition, there is debate over the exact contribution of natural sources such as volcanoes.

Petroleum companies add chemical compounds to their fuels to improve the performance or lifetime of engines.¹ Tetraethyl lead, often referred to simply as “lead,” was used to improve the knock resistance of gasoline and, thereby, produce better engine performance. However, the combustion of this chemical releases lead metal, which is responsible for a neurological disease called saturnism. Its use is now forbidden in most developed countries, and it has been replaced by other chemicals.¹

1.2 Global Warming

Global warming is a result of the greenhouse effect induced by the presence of carbon dioxide and other gases, such as methane, in the atmosphere. These gases trap the Sun’s infrared radiation reflected from the ground, thus retaining the energy in the atmosphere and increasing the temperature. An increased Earth temperature results in major ecological damage to ecosystems and in many natural disasters that affect human populations.²

Considering the ecological damage induced by global warming, the disappearance of some endangered species is a concern because this destabilizes the natural resources that feed some populations. There are also concerns about the migration of some species from warm seas to previously colder northern seas, where they can potentially destroy indigenous species and the economies that live off those species. This may be happening in the Mediterranean Sea, where barracudas from the Red Sea have been observed.

Natural disasters command our attention more than ecological disasters because of the magnitude of the damage they cause. Global warming is believed to have induced meteorological phenomena such as El Niño, which disturbs the South Pacific region and regularly causes tornadoes, floods, and droughts. The melting of the polar icecaps, another major result of global warming, raises the sea level and can cause the permanent inundation of coastal regions and sometimes of entire countries.

Carbon dioxide is the result of the combustion of HCs and coal. Transportation accounts for a large share (32% from 1980 to 1999) of carbon dioxide emissions. The distribution of carbon dioxide emissions is shown in Figure 1.1.⁴

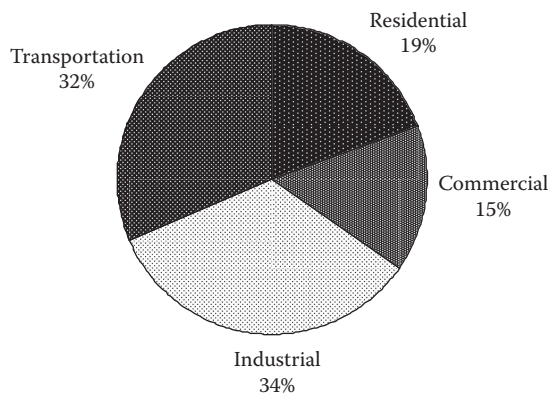


FIGURE 1.1

Carbon dioxide emission distribution from 1980 to 1999.

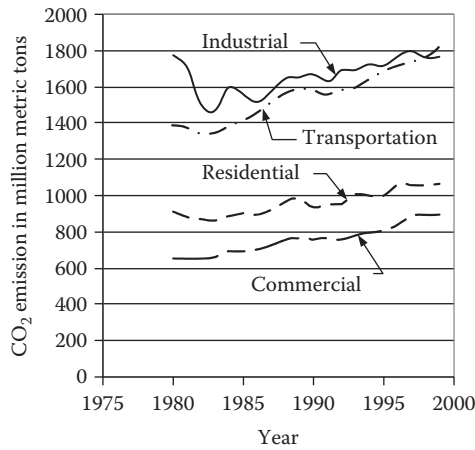


FIGURE 1.2
Evolution of CO₂ emission.

Figure 1.2 shows the trend in carbon dioxide emissions. The transportation sector is clearly now the major contributor to carbon dioxide emissions. It should be noted that developing countries are rapidly increasing their transportation sector, and these countries represent a very large share of the world's population. Further discussion of this issue is provided in the next subsection.

The large amounts of carbon dioxide released into the atmosphere by human activities are believed to be largely responsible for the increase in the global temperature on Earth observed in recent decades (Figure 1.3). It is important to note that carbon dioxide is indeed digested by plants and sequestered by oceans in the form of carbonates. However, these natural assimilation processes are limited and cannot assimilate all emitted carbon dioxide, resulting in an accumulation of carbon dioxide in the atmosphere.

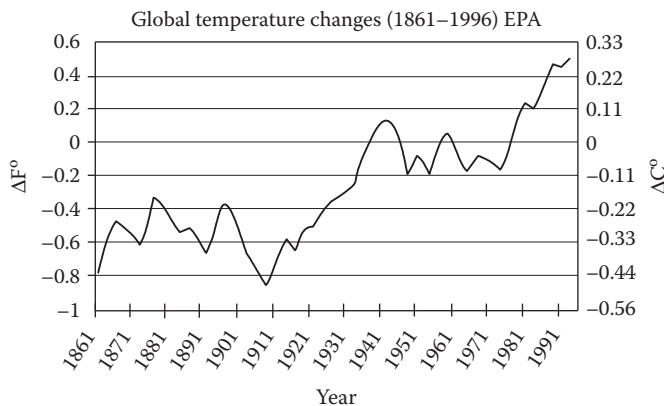


FIGURE 1.3
Global Earth atmospheric temperature. (IPCC (1995) updated.)

1.3 Petroleum Resources

The vast majority of fuels for transportation are liquid fuels originating from petroleum. Petroleum is a fossil fuel, resulting from the decomposition of living matter imprisoned millions of years ago (Ordovician, 600–400 million years ago) in geologically stable layers. The process is roughly as follows: living matter (mostly plants) dies and is slowly covered by sediments. Over time, these accumulating sediments form thick layers and transform into rock. The living matter is trapped in a closed space, where it encounters high pressures and temperatures and slowly transforms into either HCs or coal, depending on its nature. This process takes millions of years to accomplish. This is what makes the Earth's fossil fuel resources finite.

Proved reserves are "those quantities that geological and engineering information indicates with reasonable certainty can be recovered in the future from known reservoirs under existing economic and operating conditions."⁵ Therefore, they do not constitute an indicator of the Earth's total reserves. The proved reserves, as they are given in the British Petroleum 2001 estimate,⁵ are given in billion tons in Table 1.1. The *R/P* ratio is the number of years that the proved reserves would last if production were to continue at its current level. This ratio is also given in Table 1.1 for each region.⁵

The oil extracted today is the easily extractable oil that lies close to the surface, in regions where the climate does not pose major problems. It is believed that far more oil lies underneath the Earth's crust in regions such as Siberia or the American and Canadian Arctic. In these regions, climate and ecological concerns are major obstacles to extracting or prospecting for oil. The estimation of the Earth's total reserves is a difficult task for political and technical reasons. A 2000 estimate of undiscovered oil resources by the U.S. Geological Survey is given in Table 1.2.⁶

Although the *R/P* ratio does not include future discoveries, it is significant. Indeed, it is based on proved reserves, which are easily accessible today. The amount of future oil discoveries is hypothetical, and newly discovered oil will not be easily accessible. The *R/P* ratio is also based on the hypothesis that production will remain constant. It is obvious, however, that consumption (and therefore production) is increasing yearly to keep up with the growth of developed and developing economies. Consumption is likely to increase in gigantic proportions with the rapid development of some highly populated countries,

TABLE 1.1

Proved Petroleum Reserves in 2000

Region	Proved Reserves in 2000 in Billion Tons	<i>R/P</i> Ratio
North America	8.5	13.8
South and Central America	13.6	39.0
Europe	2.5	7.7
Africa	10.0	26.8
Middle East	92.5	83.6
Former USSR	9.0	22.7
Asia Pacific	6.0	15.9
Total world	142.1	39.9

TABLE 1.2

U.S. Geological Survey Estimate of Undiscovered Oil in 2000

Region	Undiscovered Oil in 2000 in Billion Tons
North America	19.8
South and Central America	14.9
Europe	3.0
Sub-Saharan Africa and Antarctic	9.7
Middle East and North Africa	31.2
Former USSR	15.7
Asia Pacific	4.0
World (potential growth)	98.3 (91.5)

particularly in the Asia-Pacific region. Figure 1.4 shows the trend in oil consumption over the last 20 years.⁷ Oil consumption is given in thousand barrels per day (one barrel is about 8 metric tons).

Despite the drop in oil consumption for Eastern Europe and the former USSR, the world trend is clearly increasing, as shown in Figure 1.5. The fastest-growing region is the Asia Pacific, where most of the world’s population lives. An explosion in oil consumption is to be expected, with a proportional increase in pollutant emissions and CO₂ emissions.

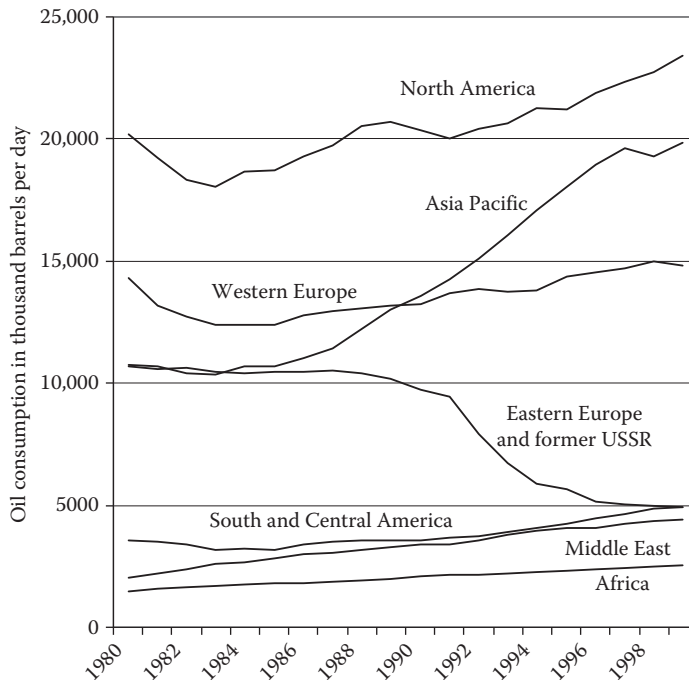


FIGURE 1.4
Oil consumption per region.

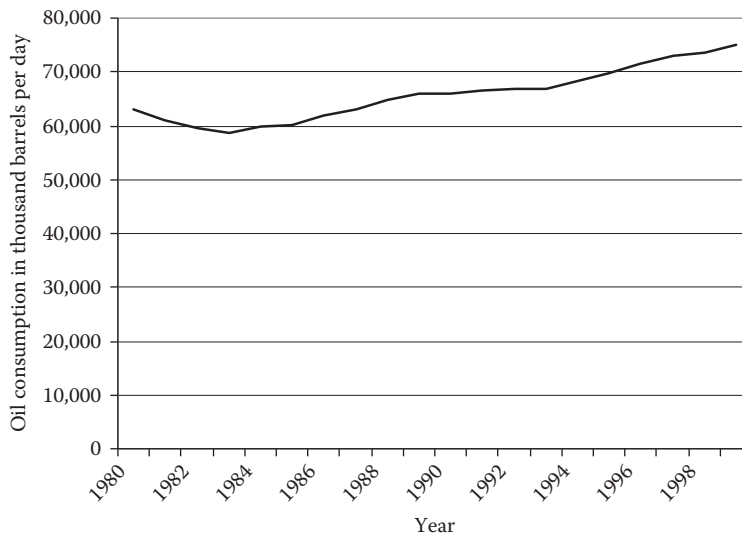


FIGURE 1.5
World oil consumption.

1.4 Induced Costs

The problems associated with the frenetic combustion of fossil fuels are many, including pollution, global warming, and foreseeable exhaustion of resources, among others. Although difficult to estimate, the costs associated with these problems are huge and indirect,⁸ and they may be financial, human, or both.

Costs induced by pollution include, but are not limited to, health expenses, the cost of replanting forests devastated by acid rain, and the cost of cleaning and fixing monuments corroded by acid rain. Health expenses probably represent the largest share of these costs, especially in developed countries with socialized medicine or health-insured populations.

Costs associated with global warming are difficult to assess. They may include the cost of the damage caused by hurricanes, lost crops due to dryness, damaged properties due to floods, and international aid to relieve the affected populations. The amount is potentially huge.

Most of the petroleum-producing countries are not the largest petroleum-consuming countries. Most of the production is located in the Middle East, while most of the consumption is located in Europe, North America, and Asia Pacific. As a result, consumers must import their oil and depend on the producing countries. This issue is particularly sensitive in the Middle East, where political turmoil affected oil delivery to Western countries in 1973 and 1977. The Gulf War, the Iran–Iraq war, and the constant surveillance of the area by the United States and allied forces come at a cost that is both human and financial. The dependency of Western economies on a fluctuating oil supply is potentially expensive. Indeed, a shortage in oil supply causes a serious slowdown of the economy, resulting in damaged perishable goods, lost business opportunities, and the eventual impossibility of running businesses.

In searching for a solution to the problems associated with oil consumption, one must take into account those induced costs. This is difficult because the cost is not necessarily incurred where it is generated. Many of the induced costs cannot be counted in asserting the benefits of an eventual solution. The solution to these problems will have to be economically sustainable and commercially viable without government subsidies to sustain itself in the long run. Nevertheless, it remains clear that any solution to these problems—even if it is only a partial solution—will indeed result in cost savings, which will benefit the payers.

1.5 Importance of Different Transportation Development Strategies to Future Oil Supply

The number of years that oil resources can support our demand for oil completely depends on the new discovery of oil reserves and cumulative oil production (as well as cumulative oil consumption). Historical data show that the rate of new discoveries of oil reserves grows slowly. On the other hand, consumption shows a high growth rate, as shown in Figure 1.6. If oil discovery and consumption follow current trends, the world’s oil resources will be used up by about 2038.^{9,10}

It is becoming more and more difficult to discover new reserves of petroleum. Exploring new oil fields is becoming an increasingly expensive venture. It is believed that the scenario of oil supply will not change much if the consumption rate cannot be significantly reduced.

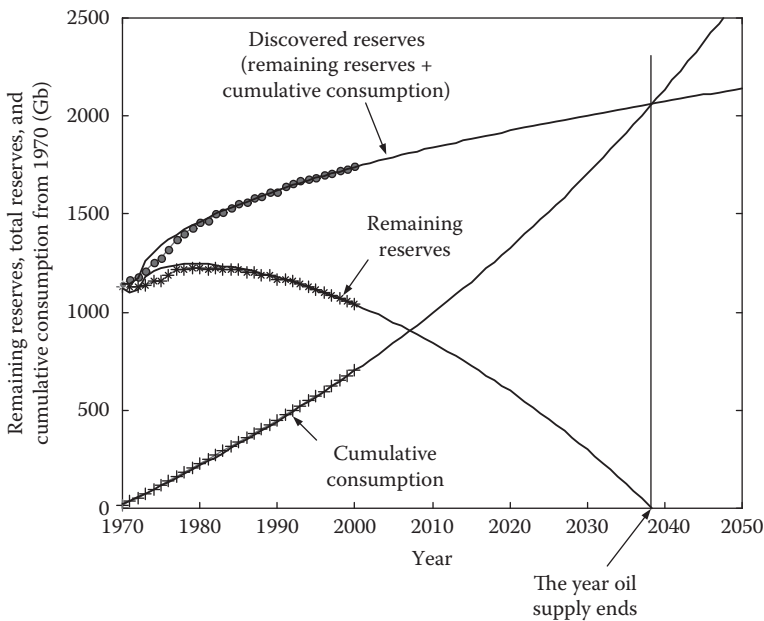


FIGURE 1.6 World oil discovery, remaining reserves, and cumulative consumption.

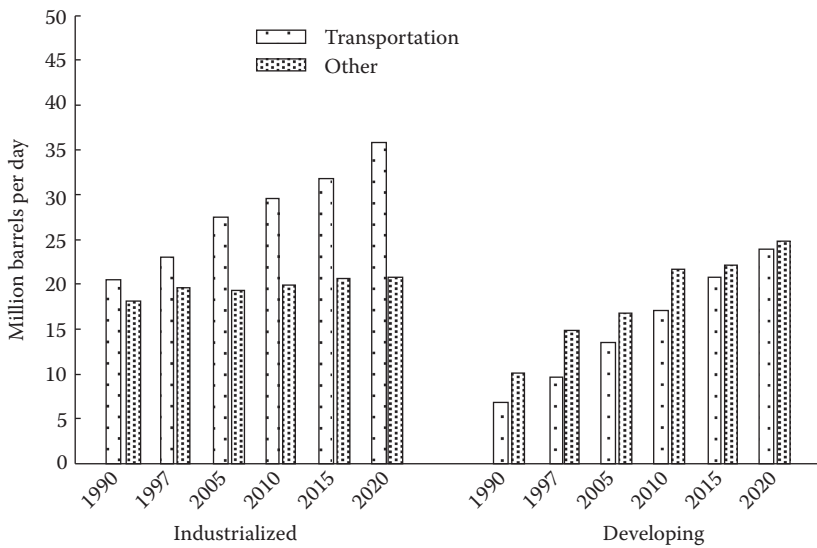


FIGURE 1.7
World oil consumption in transportation and other sectors.

As shown in Figure 1.7, the transportation sector is the primary user of petroleum, consuming 49% of the oil used in the world in 1997. The patterns of consumption of industrialized and developing countries are quite different, however. In the heat and power segments of the markets in industrialized countries, nonpetroleum energy sources were able to compete with and substitute for oil throughout the 1980s; by 1990, the oil consumption in other sectors was less than that in the transportation sector.

Most of the gains in worldwide oil use occur in the transportation sector. Of the total increase (11.4 million barrels per day) projected for industrialized countries from 1997 to 2020, 10.7 million barrels per day are attributed to the transportation sector, where few alternatives are economical until late in the forecast.

In developing countries, the transportation sector also shows the fastest projected growth in petroleum consumption, promising to rise nearly to the level of nontransportation energy use by 2020. In the developing world, however, unlike in industrialized countries, oil use for purposes other than transportation is projected to contribute 42% of the total increase in petroleum consumption. The growth in nontransportation petroleum consumption in developing countries is caused in part by the substitution of petroleum products for non-commercial fuels (such as wood burning for home heating and cooking).

Improving the fuel economy of vehicles has a crucial impact on oil supply. So far, the most promising technologies are HEVs and fuel cell vehicles. Hybrid vehicles, using current IC engines as their primary power source and batteries/electric motor as the peaking power source, have a much higher operational efficiency than those powered by an IC engine alone. The hardware and software of this technology are almost ready for industrial manufacturing. On the other hand, fuel cell vehicles, which are potentially more efficient and cleaner than HEVs, are still in the laboratory stage, and it will take a long time to overcome technical hurdles for commercialization.

Figure 1.8 shows the generalized annual fuel consumption of different development strategies of next-generation vehicles. Curve a–b–c represents the annual fuel consumption

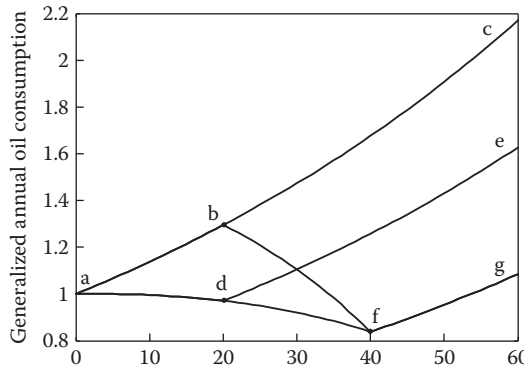


FIGURE 1.8 Comparison of annual fuel consumption between different development strategies of next-generation vehicles.

trend of current vehicles, which is assumed to have a 1.3% annual growth rate. This annual growth rate is assumed to be that of the total vehicle number. Curve a–d–e represents a development strategy in which conventional vehicles gradually become hybrid vehicles during the first 20 years, and after 20 years, all vehicles will be hybrids. In this strategy, it is assumed that the hybrid vehicle is 25% more efficient than a current conventional vehicle (25% less fuel consumption). Curve a–b–f–g represents a strategy in which, in the first 20 years, fuel cell vehicles are in a developing stage, while current conventional vehicles are still on the market. In the second 20 years, the fuel cell vehicles will gradually go to market, starting from point b and becoming totally fuel cell powered at point f. In this strategy, it is assumed that 50% less fuel will be consumed by fuel cell vehicles than by current conventional vehicles. Curve a–d–f–g represents a strategy whereby vehicles become hybrid in the first 20 years and fuel cell powered in the second 20 years.

Cumulative oil consumption is more meaningful because it involves annual consumption and the time effect, and it is directly associated with the reduction of oil reserves, as shown in Figure 1.6. Figure 1.9 shows the scenario of generalized cumulative oil consumption of the

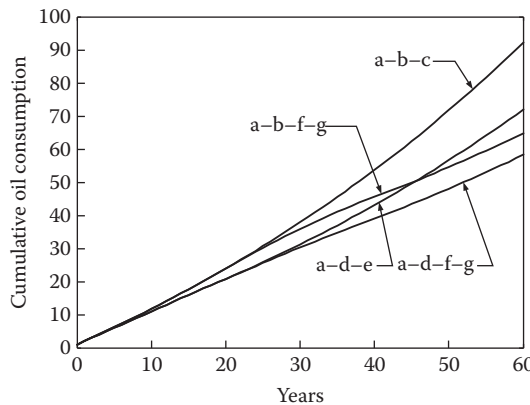


FIGURE 1.9 Comparison of cumulative fuel consumption between different development strategies of next-generation vehicles.

development strategies mentioned previously. Although fuel cell vehicles are more efficient than hybrid vehicles, the cumulative fuel consumption by strategy a–b–f–g (a fuel cell vehicle in the second 20 years) is higher than the strategy a–d–e (a hybrid vehicle in the first 20 years) within 45 years due to the time effect. From Figure 1.8 it is clear that strategy a–d–f–g (a hybrid vehicle in the first 20 years and a fuel cell vehicle in the second 20 years) is the best. Figures 1.6 and 1.9 reveal another important fact: fuel cell vehicles should not rely on oil products because of the difficulty of future oil supply 45 years later. Thus, the best development strategy of next-generation transportation would be to commercialize HEVs immediately and, at the same time, do the best to commercialize nonpetroleum fuel cell vehicles as soon as possible.

1.6 History of EVs

The first EV was built by Frenchman Gustave Trouvé in 1881. It was a tricycle powered by a 0.1-hp direct current (DC) motor fed by lead-acid batteries. The whole vehicle and its driver weighed approximately 160 kg. A vehicle similar to this was built in 1883 by two British professors.¹¹ These early realizations did not attract much attention from the public because the technology was not mature enough to compete with horse carriages. Speeds of 15 km/h and a range of 16 km were nothing exciting for potential customers. The 1864 Paris-to-Rouen race changed it all. The 1135-km race was run in 48 h and 53 min at an average speed of 23.3 km/h. This speed was by far superior to that possible with horse-drawn carriages. The public became interested in horseless carriages, or automobiles as these vehicles were now called.

The following 20 years were an era during which EVs competed with their gasoline counterparts. This was particularly true in the United States, where there were not many paved roads outside a few cities. The limited range of EVs was not a problem. However, in Europe, the rapidly increasing number of paved roads called for extended ranges, favoring gasoline vehicles.¹¹

The first commercial EV was Morris and Salom's Electrobat. This vehicle was operated as a taxi in New York City by a company created by its inventors. The Electrobat proved to be more profitable than horse cabs despite a higher purchase price (around \$3000 versus \$1200). It could be used for three shifts of 4 h with 90-min recharging periods in between. It was powered by two 1.5-hp motors that allowed a maximum speed of 32 km/h and a 40-km range.¹¹

The most significant technical advance of that era was the invention of regenerative braking by Frenchman M. A. Darracq on his 1897 coupe. This method makes it possible to recover the vehicle's kinetic energy while braking and recharging the batteries, which greatly enhances the driving range. It is one of the most significant contributions to electric and HEV technology as it contributes to energy efficiency more than anything else in urban driving.

In addition, among the most significant EVs of that era was the first vehicle ever to reach 100 km. It was "La Jamais Contente" built by Frenchman Camille Jenatton. Note that Studebaker and Oldsmobile got started in business by building EVs.

As gasoline automobiles became more powerful, more flexible, and above all easier to handle, EVs started to disappear. Their high cost did not help, but it was their limited driving range and performance that really hurt them versus their gasoline counterparts. The last

commercially significant EVs were released around 1905. For nearly 60 years, the only EVs sold were common golf carts and delivery vehicles.

In 1945, three researchers at Bell Laboratories invented a device that was meant to revolutionize the world of electronics and electricity: the transistor. It quickly replaced vacuum tubes for signal electronics, and soon the thyristor was invented, which made it possible to switch high currents at high voltages. This made it possible to regulate the power fed to an electric motor without the very inefficient rheostats, and it allowed the running of AC motors at variable frequency. In 1966, General Motors (GM) built the Electrovan, which was propelled by induction motors fed by inverters built with thyristors.

The most significant EV of that era was the Lunar Roving Vehicle, which the Apollo astronauts used on the Moon. The vehicle itself weighed 209 kg and could carry a payload of 490 kg. The range was around 65 km. The design of this extraterrestrial vehicle, however, has very little significance down on Earth. The absence of air and the lower gravity on the Moon, as well as the low speed, made it easier for engineers to reach an extended range with a limited technology.

During the 1960s and 1970s, concerns about the environment spurred research on EVs. However, despite advances in battery technology and power electronics, their range and performance remained obstacles.

The modern EV era culminated in the 1980s and early 1990s with the release of a few realistic vehicles by firms such as GM with the EV₁ and Peugeot Société Anonyme (PSA) with the 106 Electric. Although these vehicles represented a real achievement, especially compared with early realizations, it became clear during the early 1990s that electric automobiles could never compete with gasoline automobiles for range and performance. The reason is that in batteries the energy is stored in the metal of the electrodes, which weigh far more than gasoline for the same energy content. The automotive industry abandoned the EV to conduct research on HEVs. After a few years of development, these are far closer to the assembly line for mass production than EVs have ever been.

In the context of the development of EVs, battery technology is the weakest, preventing the EVs from making it to market. Great effort and investment have been put into battery research, with the intention of improving performance to meet EV requirements. Unfortunately, progress has been very limited. Performance lags far behind requirements, especially energy storage capacity per unit weight and volume. This poor energy storage capability of batteries limits EVs to specific applications, such as at airports, railroad stations, mail delivery routes, golf courses, and so on. In fact, basic study¹² shows that the EV will never be able to challenge the liquid-fueled vehicle even with the optimistic value of battery energy capacity. Thus, in recent years, advanced vehicle technology research has turned to HEVs as well as fuel cell vehicles.

1.7 History of HEVs

Surprisingly, the concept of an HEV is almost as old as the automobile itself. The primary purpose, however, was not so much to lower the fuel consumption but rather to assist the IC engine in providing an acceptable level of performance. Indeed, in the early days, IC engine engineering was less advanced than electric motor engineering.

The first hybrid vehicles reported were shown at the Paris Salon of 1899.¹³ These were built by the Pieper establishments of Liège, Belgium and by the Vedovelli and Priestly

Electric Carriage Company, France. The Pieper vehicle was a parallel hybrid with a small air-cooled gasoline engine assisted by an electric motor and lead-acid batteries. It is reported that the batteries were charged by the engine when the vehicle coasted or was at a standstill. When the driving power required was greater than the engine rating, the electric motor provided additional power. In addition to being one of the first two hybrid vehicles and the first parallel hybrid vehicle, the Pieper was undoubtedly the first electric starter.

The other hybrid vehicle introduced at the Paris Salon of 1899 was the first series HEV and was derived from a pure EV commercially built by the French firm Vedovelli and Priestly.¹³ This vehicle was a tricycle, with the two rear wheels powered by independent motors. An additional $\frac{3}{4}$ -hp gasoline engine coupled to a 1.1-kW generator was mounted on a trailer and could be towed behind the vehicle to extend the range by recharging the batteries. In the French case, the hybrid design was used to extend its range by recharging the batteries. Also, the hybrid design was used to extend the range of an EV, not to supply additional power to a weak IC engine.

Frenchman Camille Jenatzy presented a parallel hybrid vehicle at the Paris Salon of 1903. This vehicle combined a 6-hp gasoline engine with a 14-hp electric machine that could either charge the batteries from the engine or assist them later. Another Frenchman, H. Krieger, built the second reported series hybrid vehicle in 1902. His design used two independent DC motors driving the front wheels. They drew their energy from 44 lead-acid cells that were recharged by a 4.5-hp alcohol spark-ignited engine coupled to a shunt DC generator.

Other hybrid vehicles, both parallel and series type, were built during the period 1899–1914. Although electric braking had been used in these early designs, there is no mention of regenerative braking. It is likely that most, possibly even all, designs used dynamic braking by short circuiting or by placing a resistance in the armature of the traction motors. The Lohner-Porsche vehicle of 1903 is a typical example of this approach.¹³ The frequent use of magnetic clutches and magnetic couplings should be noted.

Early hybrid vehicles were built to assist the weak IC engines of that time or to improve the range of EVs. They made use of the basic electric technologies that were then available. Despite the great creativity that featured in their design, these early hybrid vehicles could no longer compete with the greatly improved gasoline engines that came into use after World War I. The gasoline engine made tremendous improvements in terms of power density, the engines became smaller and more efficient, and there was no longer a need to assist them with electric motors. The supplementary cost of having an electric motor and the hazards associated with the lead-acid batteries were key factors in the disappearance of hybrid vehicles from the market after World War I.

However, the greatest problem that these early designs had to cope with was the difficulty of controlling the electric machine. Power electronics did not become available until the mid-1960s, and early electric motors were controlled by mechanical switches and resistors. They had a limited operating range incompatible with efficient operation. Only with great difficulty could they be made compatible with the operation of a hybrid vehicle.

Dr. Victor Wouk is recognized as the modern investigator of the HEV movement.¹³ In 1975, along with his colleagues, he built a parallel hybrid version of a Buick Skylark.¹³ The engine was a Mazda rotary engine coupled to a manual transmission. It was assisted by a 15-hp, separately excited DC machine located in front of the transmission. Eight 12-V automotive batteries were used for energy storage. A top speed of 129 km/h (80 mph) was achieved, with acceleration from 0 to 60 mph in 16 s.

The series hybrid design was revived by Dr. Ernest H. Wakefield in 1967, when working for Linear Alpha Inc. A small engine coupled to an AC generator, with an output of 3 kW, was used to keep a battery pack charged. However, the experiments were quickly stopped

because of technical problems. Other approaches used during the 1970s and early 1980s used range extenders, similar in concept to the French Vedovelli and Priestly 1899 design. These range extenders were intended to improve the range of EVs that never reached the market. Other prototypes of hybrid vehicles were built by the Electric Auto Corporation in 1982 and by the Briggs & Stratton Corporation in 1980. These were both parallel hybrid vehicles.

Despite the two oil crises of 1973 and 1977, and despite growing environmental concerns, no HEV made it to the market. Researchers' focus was on the EV, of which many prototypes were built during the 1980s. The lack of interest in HEVs during this period may be attributed to the lack of practical power electronics, modern electric motor, and battery technologies. The 1980s witnessed a reduction in conventional IC engine-powered vehicle sizes, the introduction of catalytic converters, and the generalization of fuel injection.

The HEV concept drew great interest during the 1990s when it became clear that EVs would never achieve the objective of saving energy. The Ford Motor Company initiated the Ford Hybrid Electric Vehicle Challenge, which drew efforts from universities to develop hybrid versions of production automobiles.

Automobile manufacturers around the world built prototypes that achieved tremendous improvements in fuel economy over their IC engine-powered counterparts. In the United States, Dodge built the Intrepid ESX 1, 2, and 3. The ESX-1 was a series hybrid vehicle, powered by a small turbocharged three-cylinder diesel engine and a battery pack. Two 100-hp electric motors were located in the rear wheels. The U.S. government launched the Partnership for a New Generation of Vehicles (PNGV), which included the goal of a midsize sedan that could achieve 80 mpg. The Ford Prodigy and GM Precept resulted from this effort. The Prodigy and Precept vehicles were parallel HEVs powered by small turbocharged diesel engines coupled to dry clutch manual transmissions. Both achieved the objective, but production did not follow.

Efforts in Europe are represented by the French Renault Next, a small parallel hybrid vehicle using a 750-cc spark-ignited engine and two electric motors. This prototype achieved 29.4 km/L (70 mpg) with maximum speed and acceleration performance comparable to conventional vehicles. Volkswagen also built a prototype, the Chico. The base was a small EV, with a nickel-metal hydride battery pack and a three-phase induction motor. A small two-cylinder gasoline engine was used to recharge the batteries and provide additional power for high-speed cruising.

The most significant effort in the development and commercialization of HEVs was made by Japanese manufacturers. In 1997, Toyota released the Prius sedan in Japan. Honda also released its Insight and Civic Hybrid. These vehicles are now available throughout the world. They achieve excellent figures of fuel consumption. Toyota's Prius and Honda's Insight vehicles have historical value in that they are the first hybrid vehicles commercialized in the modern era to respond to the problem of personal vehicle fuel consumption.

1.8 History of Fuel Cell Vehicles

As early as 1839, Sir William Grove (often referred to as the "Father of the Fuel Cell") discovered that it may be possible to generate electricity by reversing the electrolysis of water. It was not until 1889 that two researchers, Charles Langer and Ludwig Mond, coined the

term “fuel cell” as they were trying to engineer the first practical fuel cell using air and coal gas. Although further attempts were made in the early 1900s to develop fuel cells that could convert coal or carbon into electricity, the advent of the IC engine temporarily quashed any hopes of further development of the fledgling technology.

Francis Bacon developed what was perhaps the first successful fuel cell device in 1932, with a hydrogen–oxygen cell using alkaline electrolytes and nickel electrodes—inexpensive alternatives to the catalysts used by Mond and Langer. Due to a substantial number of technical hurdles, it was not until 1959 that Bacon and company first demonstrated a practical 5-kW fuel cell system. Harry Karl Ihrig presented his now-famous 20-hp fuel-cell-powered tractor that same year.

The National Aeronautics and Space Administration (NASA) also began building compact electric generators for use on space missions in the late 1950s. NASA soon came to fund hundreds of research contracts involving fuel cell technology. Fuel cells now have a proven role in the space program, having supplied electricity for several space missions.

In more recent decades, several manufacturers—including major automakers—and various federal agencies have supported ongoing research into the development of fuel cell technology for use in fuel cell vehicles and other applications.¹⁴ Hydrogen production, storage, and distribution are the biggest challenges. Truly, fuel-cell-powered vehicles still have a long way to go to enter the market.

Bibliography

1. C. R. Ferguson and A. T. Kirkpatrick, *Internal Combustion Engines—Applied Thermo-Sciences*, Second Edition, John Wiley & Sons, New York, 2001.
2. U.S. Environmental Protection Agency (EPA), *Automobile emissions: An overview*, EPA 400-F-92-007, Fact Sheet OMS-5, August 1994.
3. U.S. Environmental Protection Agency (EPA), *Automobiles and ozone*, EPA 400-F-92-006, Fact Sheet OMS-4, January 1993.
4. Energy Information Administration, U.S. Department of Energy, *Carbon dioxide emissions from energy consumption by sector, 1980–1999, 2001*, available at <http://www.eia.doe.gov/emeu/aer/txt/tab1202.htm>.
5. BP statistical review of world energy—oil, 2001, available at http://www.bp.com/downloads/837/global_oil_section.pdf.
6. USGS World Energy Assessment Team, *World undiscovered assessment results summary*, U.S. Geological Survey Digital Data Series 60, available at <http://greenwood.cr.usgs.gov/energy/WorldEnergy/DDS-60/sum1.html#TOP>.
7. International Energy Database, Energy Information Administration, U.S. Department of Energy, *World petroleum consumption, 1980–1999, 2000*.
8. D. Doniger, D. Friedman, R. Hwang, D. Lashof, and J. Mark, *Dangerous addiction: Ending America’s oil dependence*, National Resources Defense Council and Union of Concerned Scientists, 2002.
9. M. Ehsani, D. Hoelscher, N. Shidore, and P. Asadi, *Impact of hybrid electric vehicles on the world’s petroleum consumption and supply*, Society of Automotive Engineers (SAE) Future Transportation Technology Conference, Paper No. 2003-01-2310, 2003.
10. J. E. Hake, *International energy outlook—2000 with projection to 2020*, available at <http://tonto.eia.doe.gov/FTPROOT/presentations/ieo2000/sld008.htm>.
11. E. H. Wakefield, *History of the Electric Automobile: Battery-only Powered Cars*, Society of Automotive Engineers (SAE), Warrendale, PA, 1994, ISBN: 1-56091-299-5.

12. Y. Gao and M. Ehsani, An investigation of battery technologies for the Army's hybrid vehicle application, *Proceedings of the IEEE 56th Vehicular Technology Conference*, Vancouver, British Columbia, Canada, September 2002.
13. E. H. Wakefield, *History of the Electric Automobile: Hybrid Electric Vehicles*, Society of Automotive Engineers (SAE), Warrendale, PA, 1998, ISBN: 0-7680-0125-0.
14. California Fuel Cell Partnership, available at <http://www.fuelcellpartnership.org/>
15. L. L. Christiansen, H. Frederick, K. Knechel, and E. L. Mussman, Meeting the Needs of Modern Transportation Researchers by Transforming the Iowa Department of Transportation Library-Early Efforts & Results. *Transportation Research Board 95th Annual Meeting*, no. 16-3827. 2016.
16. C. Ergas, M. Clement, and J. McGee, Urban density and the metabolic reach of metropolitan areas: A panel analysis of per capita transportation emissions at the county-level. *Social Science Research* 58, 2016: 243–253.
17. E. Weiner, *Urban transportation planning in the United States: History, policy, and practice*. Springer, 2016.
18. M. Alam, J. Ferreira, and J. Fonseca, Introduction to intelligent transportation systems. *Intelligent Transportation Systems*, pp. 1–17. Springer International Publishing, 2016.
19. R. Jedwab and A. Moradi, The permanent effects of transportation revolutions in poor countries: Evidence from Africa. *Review of Economics and Statistics* 98(2), 2016: 268–284.
20. S. A. Bagloee, M. Tavana, M. Asadi, and T. Oliver, Autonomous vehicles: Challenges, opportunities, and future implications for transportation policies. *Journal of Modern Transportation* 24 (4), 2016: 284–303.
21. M. Lawry, A. Mirza, Y. W. Wang, and D. Sundaram, Efficient Transportation-Does the Future Lie in Vehicle Technologies or in Transportation Systems? *International Conference on Future Network Systems and Security*, pp. 126–138. Springer, Cham, 2017.
22. M. Chowdhury and K. Dey, Intelligent transportation systems-a frontier for breaking boundaries of traditional academic engineering disciplines [Education]. *IEEE Intelligent Transportation Systems Magazine* 8(1), 2016: 4–8.
23. J. Hogerwaard, I. Dincer, and C. Zamfirescu, Thermodynamic and environmental impact assessment of NH3 diesel-fueled locomotive configurations for clean rail transportation. *Journal of Energy Engineering* 143(5), 2017: 04017018.
24. J. D. K. Bishop, N. Molden, and A. M. Boies, Real-world environmental impacts from modern passenger vehicles operating in urban settings. *International Journal of Transport Development and Integration* 1(2), 2017: 203–211.
25. L. A. W. Ellingsen, B. Singh, and A. H. Strømman, The size and range effect: Lifecycle greenhouse gas emissions of electric vehicles. *Environmental Research Letters* 11(5), 2016: 054010.
26. H. I. Abdel-Shafy and M. S. M. Mansour, A review on polycyclic aromatic hydrocarbons: source, environmental impact, effect on human health and remediation. *Egyptian Journal of Petroleum* 25(1), 2016: 107–123.
27. W. Ren, B. Xue, Y. Geng, C. Lu, C. Y. Zhang, L. Zhang, T. Fujita, and H. Hao, Inter-city passenger transport in larger urban agglomeration area: Emissions and health impacts. *Journal of Cleaner Production* 114, 2016: 412–419.
28. W. Ke, S. Zhang, X. He, Y. Wu, and J. Hao, Well-to-wheels energy consumption and emissions of electric vehicles: Mid-term implications from real-world features and air pollution control progress. *Applied Energy* 188, 2017: 367–377.
29. S. S. Sosale, Performance Analysis of Various 4-Wheelers with IC Engines for Hybridization, 2017.
30. D. Karner and J. Francfort, Hybrid and plug-in hybrid electric vehicle performance testing by the US Department of Energy Advanced Vehicle Testing Activity. *Journal of Power Sources* 174, 2007: 69–75. <http://dx.doi.org/10.1016/j.jpowsour.2007.06.069>.
31. X. Hu, N. Murgovski, L. M. Johannesson, and B. Egardt, Comparison of three electrochemical energy buffers applied to a hybrid bus powertrain with simultaneous optimal sizing and energy management. *IEEE Transactions on Intelligent Transportation Systems* 15, 2014: 1193–1205. <http://dx.doi.org/10.1109/TITS.2013.2294675>.